공학박사 학위논문

Development of High Performance Solution-Processed Oxide Thin-Film Transistors through Alkali Metal Doping and Dielectric Engineering

알칼리 금속 도핑과 절연체 엔지니어링을 통한 고성능 용액 공정 산화물 박막 트랜지스터 개발에 관한 연구

2017년 8월

서울대학교 대학원

융합과학부 나노융합전공

임 건 희

Development of High Performance Solution-Processed Oxide Thin-Film Transistors through Alkali Metal Doping and Dielectric Engineering

지도교수 김 연 상

이 논문을 공학박사 학위논문으로 제출함
2017년 7월

서울대학교 대학원
융합과학부 나노융합전공
임 건 희

임건희의 박사학위논문을 인준함
2017년 6월

위 원 장 송 윤 규 (인)

부 위 원 장 김 연 상 (인)

위 원 조 정 호 (인)

위 원 박 원 철 (인)

위 원 김 명 길 (인)

Abstract

Development of High Performance Solution-Processed Oxide Thin-Film Transistors through Alkali Metal Doping and Dielectric Engineering

Keon-Hee Lim

Program in Nanoscience and Technology

The Graduate School

Seoul National University

Solution-processed oxide semiconductors thin-film transistors (TFTs) with transparent, flexible properties and low-cost manufacturing have a great potential for future display requiring advanced performances such as high resolution and large scale as well as unique properties such as transparency and flexibility. However, there are several limitations for practical applications. Especially, a relatively low field-effect mobility compared with that of low temperature poly Si (LTPS) TFTs and high vacuum-processed oxide semiconductor TFTs is a critical issue. Accordingly, many studies have mainly

focused on the development of solution-processed oxide semiconductor TFTs having a high field-effect mobility with various methods. However, their low field-effect mobility still remains a problem.

Herein, I propose alkali metal doping and dielectric engineering for the increase of field-effect mobility in solution-processed oxide semiconductor TFTs. Through alkali metal doping, the field-effect mobility of solution-processed $ZnSn_xO_y$ (ZTO) TFTs was increased 2 ~ 3 times. Also, with the dielectric engineering, the field-effect mobility of the ZTO TFTs could be dramatically enhanced. Using various analyses with X-ray diffraction (XRD), high-resolution transmission electron microscopy (HRTEM), atomic force microscopy (AFM), X-ray photoemission spectroscopy (XPS), developed TFT model, and the like, the mechanism how field-effect mobility is increased by the alkali metal doping and the dielectric engineering has been investigated. These methods have good potential for the application of the solution-processed oxide semiconductor in future display technology.

Keywords : oxide semiconductor, solution-process, high mobility, thin-film transistor, alkali metal doping, dielectric engineering

Student Number : 2011-22761

Contents

List of Tables and Figures

60% HCA operated at V_{ds} = 1 V.

Figure 4.9 (a) The hysterysis of ZTO TFTs on 60% HCA with 1000 μm channel width and 15 μm channel length. The change of drain current and field-effect mobility of ZTO TFTs on 60% HCA by repeat test at constant gate voltage and drain voltage, (b) V_{gs} = 6 V, V_{ds} = 5 V (c) V_{gs} = 8 V, V_{ds} = 5 V (d) V_{gs}= 10 V, V_{ds} = 5 V. (e) Transfer characteristics and (f) field-effect mobility of ZTO TFTs on 60% HCA with 1000 μm channel width and 50 μm channel length after switching test.

Figure 4.10 (a) The leakage current of ZTO TFTs on 60% HCA with 1000 μm channel width and 15 μm channel length. (b) The schematic of leakage current mechanism in these devices.

Figure 4.11 (a) transfer characteristics and gate leakage current of patterned ZTO TFTs on a 60% HCA. (b) The histogram of the field-effect mobility of the patterned ZTO TFTs on 60% HCA.

Figure 4.12 (a) ZTO TFT on 60% HCA with 1000 μm channel width and 50 μm channel length. (b) ZTO TFT on 60% HCA with 1000 μm channel width and 15 m channel length. (c) patterned ZTO TFT on 60% HCA with 1000 μm channel width and 50 μm channel length. (d) patterned ZTO TFT on a bilayer dielectric composed of 60% HCA and 100 nm SiN_x with 1000 μm channel width and 50 μm channel length. (e) patterned ZTO TFT on a bilayer dielectric composed of 60% HCA and 200 nm SiN_x with 1000 μm channel width and 50 μm channel length. (f) patterned ZTO TFT on a bilayer composed of 60% HCA and 200nm SiN_x with 1000 μm channel width and 30 μm

semiconductor – metal) structure. (The semiconductor and top metal region was patterned in circle shape, R = 250 μm, 20 Hz frequency condition)

Figure 4.33 The electron transport mechanism at ZTO TFTs on HCA. (a) The band diagram and electron transport mechanism of ZTO TFT on 0% HCA at high V_{gs} (ZTO TFTs on 0% HCA at V_{gs} = 10 V). The band diagram and electron transport mechanism of ZTO TFT on 60% HCA when (b) V_{gs} is lower than specific voltage (ZTO TFTs on 0% HCA at V_{gs} < 6 V, gradual enhancement region) or (c) V_{gs} is higher than specific voltage (ZTO TFTs on 0% HCA at V_{gs} > 6 V, dramatic enhancement region).

Abbreviations

TFT Thin-film transistor

LTPS Low temperature poly silicon

ZTO Zinc tin oxide

XPS X-ray photoemission spectroscopy

AFM Atomic force microscopy

HRTEM High-resolution transmission electron microscopy

UV Ultraviolet

MTR Multiple trapping and release

VRH Variable range hopping

EDX Energy-dispersive X-ray spectroscopy

EELS Electron energy loss spectroscopy

XRD X-ray diffraction

XRR X-ray reflectivity

BJT Bipolar junction transistor

FET Field-effect transistor

LCD Liquid crystal display

OLED Organic light emitting display

MOSFET Metal oxide semiconductor field-effect transistor

V_T Threshold voltage

V_{gs} Gate-source voltage

I_{ds} Drain-source current

V_{ds} Drain-source voltage

μ_{FE} Field-effect mobility

S Subthreshold swing

V_{on} Turn-on voltage

IGZO InGaZnO

RC Resistance-capacitance

IC Integrated circuit

DEMUX Demultiplexer

ITZO $InSn_xZn_yO_z$

PLD Pulsed laser deposition

RF Radio frequency

ALD Atomic layer deposition

ZTO Zinc tin oxide

SEM Scanning electron microscopy

O_{vac} Oxygen vacancy

OH Hydroxide

M-O Metal oxide

$Zn(CH_3COO)_2$ Zinc acetate

$SnCl_2$ Tin chloride

$Li(CH_3COO)$ Lithium acetate

$Na(CH_3COO)$ Sodium acetate

HCA Humidity-controlled Al_2O_3

FFT Fast Fourier transformation

$Al(NO_3)_39H_2O$ Aluminium nitrate nonahydrate

MISM Metal-insulator-semiconductor-metal

Chapter 1. Introduction

In future display, the unique properties with transparency and flexibility as well as advanced properties with ultra-high resolution and large scale have been demanded for realistically delivering the visual information. [1-5] To realize the transparent and flexible display, the development of transparent and flexible thin-film transistor (TFT) is essential. Also, in advanced display, the development of high mobility TFTs is essential to overcome them, because a decrease of accumulated charges from an increase of the resistance-capacitance delay and of the TFT dimension in pixels, makes it hard to effectively drive the display. [6, 7]

Low temperature poly silicon (LTPS) TFT and oxide semiconductor TFT replacing the conventional amorphous silicon TFT (< 1 cm^2 V^{-1} s^{-1}) have attracted great interest. Although LTPS TFT has a high field-effect mobility around 100 cm^2 V^{-1} s^{-1}, the LTPS TFT has considerable difficulty in applying to a practical, large-sized display because LTPS manufactured by an excimer laser beam does not mostly have uniform electrical characteristics. [8] Furthermore, its opaque property presents a limitation as a TFT for future display.

oxide semiconductor TFT has large-scale processability, low cost fabrication, and transparency. In addition, oxide semiconductor can be realized by solution-process which has many advantages as future fabrication processing such as low cost, continuous, and large scale fabrication. [9] However, it is still limited by a relatively low field-effect mobility compared with that of LTPS TFT. Thus, many

researchers have tried to improve the field-effect mobility of oxide semiconductor TFTs through various methods (e.g., dual-gate design, doping methods, confining structures, etc.). However, they still suffer from low field-effect mobility under 50 $cm^2 V^{-1} s^{-1}$. [10-14]

To address the issue, this dissertation focuses on the development of solution-processed oxide semiconductor TFT having high field-effect mobility. Before addressing the issue, basic knowledge and background are introduced in chapter 2.

In chapter 3, to enhance the field-effect mobility of solution-processed amorphous zinc tin oxide (ZTO) semiconductor TFTs, the method using alkali metals, Li and Na, doping method and its mobility enhancement mechanism are introduced. Through alkali metal doping, ZTO TFT with two to three times higher mobility were realized. To investigated unrevealed mechanism how alkali metal dopant enhance the field-effect mobility of amorphous ZTO, various techniques such as X-ray photoemission spectroscopy (XPS), atomic force microscopy (AFM), high-resolution transmission electron microscopy (HRTEM), Hall measurement and so on. From these analyses, the correlation between the enhancement of field-effect mobility and the increase of carrier concentration depending on the amount of alkali metal doping was revealed. Through spectroscopic ultraviolet (UV)-visible analysis, the validity of the hypothesis was supported. In addition, it suggests the useful monitoring technique for the change in electrical performance of ZTO TFT doped by alkali metal with the optical bandgap shift. This work has been published

as “UV-Visible Spectroscopic Analysis of Electrical Properties in Alkali Metal-Doped Amorphous Zinc Tin Oxide Thin-Film Transistors” by K.-H Lim *et. al.* Advanced Materials, 25, 2994 (2013). [15]

In chapter 4, I introduce the dielectric engineering for the dramatic enhancement of field-effect mobility in solution-processed oxide semiconductor TFTs. In particular, it was discovered that the change in humidity during annealing process in Al_2O_3 dielectric fabrication process is a important factor which enhances the field-effect mobility of the solution-processed ZTO TFTs. When ZTO TFTs are fabricated at Al_2O_3 fabricated in 60% humidity condition, the ZTO TFTs which exhibit a very high effective field-effect mobility of over 400 cm^2 V^{-1} s^{-1} with 10^6 on/off current ratio were realized. For investigation of the abnormal phenomenon, the electrical properties were strictly investigated through various electrical tests. Furthermore, based on the application of the various oxide semiconductor TFT models, such as multiple trapping and release (MTR) and variable range hopping (VRH) percolation models, and systematic analyses with the temperature dependence of electrical behavior in the ZTO TFTs, high-resolution transmission electron microscopy (HRTEM), energy-dispersive X-ray spectroscopy (EDX), electron energy loss spectroscopy (EELS), X-ray diffraction (XRD), atomic force microscopy (AFM), X-ray reflectivity (XRR), and X-ray photoemission spectroscopy (XPS), I proposed a electron transport mechanism explaining the abnormal increase of the field-effect

mobility of ZTO TFTs by the dielectric engineering. This work has been prepared as “Unusual Performance Enhancement of Solution-Processed Oxide Semiconductor Thin-Film Transistors *via* Dielectric Engineering” by K.-H Lim *et. al.* (Submitted)

Finally, in chapter 5, the overall conclusion and the potential of this dissertation are summarized

1.1 References

[1] E. Fortunato, P. Barquinha, R. Martins, Adv. Mater. 2012, 24, 2945.

[2] K. Nomura, H. Ohta, K. Ueda, T. Kamiya, M. Hirano, H. Hosono, Science, 2003, 300, 1269.

[3] Y.-H. Kim, J.-S. Heo, T.-H. Kim, S. Park, M.-H. Yoon, J. Kim, M. S. Oh, G.-R. Yi, Y.-Y. Noh, S. K. Park, Nature, 2012, 489, 128.

[4] K. Nomura, H. Ohta, A. Takagi, T. Kamiya, M. Hirano, H. Hosono, Nature, 2004, 432, 488.

[5] E. Lee, J. Ko, K.-H. Lim, K. Kim, S. Y. Park, J. M. Myoung, Y. S. Kim, Adv. Func. Mater. 2014, 24, 4689.

[6] J. Y. Kwon, K. S. Son, J. S. Jung, T. S. Kim, M. K. Ryu, K. B. Park, B. W. Yoo, J. W. Kim, Y. G. Lee, K. C. Park, S. Y. Lee, J. M. Kim, IEEE. Electron Device Lett. 2008, 29, 1309

[7] J. C. Park, S. W. Kim, S. I. Kim, H. Yin, J. H. Hur, S. H. Jeon, S. H. Park, I H. Song, Y. S. Park, U I. Chung, M. K. Ryu, S. Lee, S. Kim, Y. Jeon, D. M. Kim, D. H. Kim, K.-W. Kwon, C. J. Kim, IEDM Tech. Dig., Dec. 2009, 7-9, 1-4

[8] T. Kamiya, K. Nomura, H. Hosono. Sci. Technol. Adv. Mater. 2010, 11, 044305.

[9] K.-H. Lim, J.-E. Huh, J. Lee, N.-K. Cho, J.-W. Park, B.-I Nam, E. Lee, Y. S. Kim, ACS Appl. Mater. Interfaces, 2017, 9, 548.

[10] Y. S. Rim, H. Chen, X. Kou, H.-S Duan, H. Zhou, M. Cai, H. J. Kim, Y. Yang, Adv. Mater. 2014, 26, 4273.

[11] H.-W. Zan, W.-T. Chen, C.-C. Yeh, H.-W. Hsueh, C.-C. Tsai,

H.-F. Meng, Appl. Phys. Lett. 2011, 98, 153506.

[12] S. T. Meyers, J. T. Anderson, C. M. Hung, J. Thompson, J. F. Wager, D. A. Keszler, J. Am. Chem. Soc. 2008, 130, 17603.

[13] S. Y. Han, G. S. Herman, C. H. Chang, J. Am. Chem. Soc. 2011, 133, 5166.

[14] K. K. Banger, Y. Yamashita, K. Mori , R. L. Peterson, T. Leedham, J. Rickard, H. Sirringhaus, Nat. Mater. 2011, 10, 45.

[15] K.-H. Lim, K. Kim, S. Kim, S. Y. Park, H. Kim, Y. S. Kim, Adv. Mater. 2013, 25, 2994.

Chapter 2. Literature Review and Theories

2.1 Thin-film transistor

2.1.1 Concept of thin-film transistor

A transistor which is known as a fundamental component for electronic devices is a semiconductor-based device for amplifying or switching electrical signals. The transistors are divided into two types : bipolar junction transistor (BJT) and field-effect transistor (FET). (Figure 2.1) Basically, although the basic role of the two types of transistors are similar, they have different structure and operating principle. The BJT is based on pnp or npn junction which is called emitter, base, and collector. Accordingly, for operation of BJT, both majority and minority carriers in semiconductors are involved. Meanwhile, FET which consists of active layer, gate-dielectric, and source/drain/gate electrodes uses the electric field to operate the device. In this process, majority charge carriers in semiconductor are mainly controlled. Accordingly, it is called an unipolar transistors.

Thin-Film Transistor (TFT) based on semiconductor, dielectric, and metal thin films is a kind of FET. Due to its thin-film structure, it is mainly used as a switching device in liquid crystal display (LCD) and organic light emitting display (OLED). Conventionally, the active layer of TFT is based on Si-based materials such as amorphous silicon or poly silicon. Recently, in order to apply it to future display with flexible and transparent characteristics, various studies have been

conducted to realize TFT using special materials such as organic and oxide materials. In addition, thin-film transistors are being studied in various fields including flexible and transparent sensors and memories.

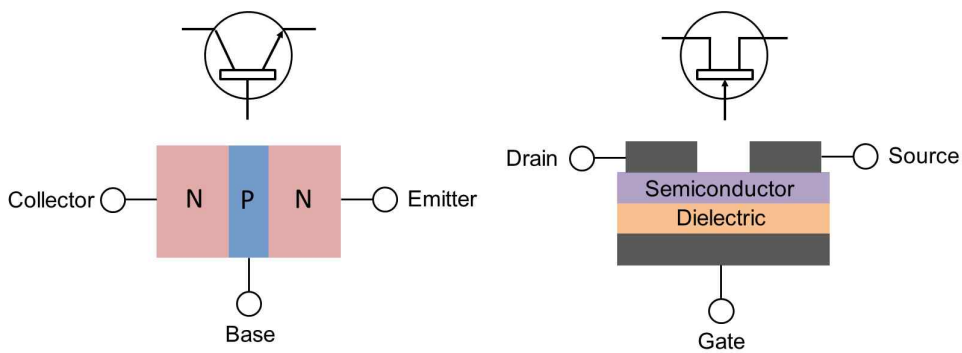

Figure 2.1 The scheme of bipolar junction transistor (BJT) and field-effect transistor (FET).

2.1.2 Operation and parameters of TFT

TFT and metal oxide semiconductor field-effect transistor (MOSFET) are a type of FET. However, they have different operation mechanism. MOSFET is based on pn junction. In addition, the device is operated by the inversion mechanism of minority carrier. On the other hand, TFT is mainly controlled by majority carrier. When n-type semiconductor is used as a active layer, the On-state of TFT is operated by the accumulation of majority carrier.

In general, TFT is divided into enhancement mode and depletion mode. In the case of n-type semiconductor-based TFT, when threshold voltage (V_T) is positive, it is designated as a enhancement mode. That is, in the enhancement mode, the On-state is realized by the principle that a channel layer occurs when a positive gate-source voltage (V_{gs}) is applied. Meanwhile, the negative V_{gs} is required for Off-state in depletion mode. [1, 2]

In On-state of TFT ($V_{gs} > V_T$), large drain-source current (I_{ds}) flows at channel region. At the On-state, depending on the drain-source voltage (V_{ds}), the I_{ds} behavior is divided into the saturation mode and the linear mode. It is clearly distinguished from output characteristic. (Figure 2.2)

[Saturation region, $V_{gs} - V_T > V_{ds}$]

$$I_{ds,\,sat} = \frac{W}{2L} C_i \mu_{sat} (V_{gs} - V_T)^2 \qquad (1)$$

[Linear region, $V_{gs} - V_T < V_{ds}$]

$$I_{ds,lin} = \frac{W}{L} C_i \mu_{lin} ((V_{gs} - V_T) V_{ds} - \frac{V_{ds}^2}{2}) \qquad (2)$$

where, W and L is a channel width and length, C_i is the capacitance of gate-dielectric. μ_{sat} and μ_{lin} are field-effect mobility in saturation and linear region.

In transfer characteristic of TFT, the important parameters of TFT can be obtained. (Figure 2.2)

[Field-effect mobility (μ_{FE})]

Mobility is an important parameter showing how fast electrons are moving in material. The mobility obtained from behavior in FET is defined as a field effect mobility.

It can be obtained by Equation 1 and 2.

$$\mu_{sat} = \frac{2L}{WC_i} \left(\frac{\partial \sqrt{I_{ds}}}{\partial V_{gs}} \right)^2 \qquad (3)$$

$$\mu_{lin} = \frac{L}{WC_i V_{ds}} \frac{\partial I_{ds}}{\partial V_{gs}} \qquad (4)$$

[On/Off current ratio (on/off)]

On/Off current ratio is the ratio of the maximum and minimum values of the drain current. It is an important parameter as a switching device.

[Subthreshold swing (S)]

Subthreshold swing parameter means V_{gs} required to increase I_{ds} by 10 times in the subthreshold region. The unit is expressed in V/decade.

$$S = \frac{\partial V_{gs}}{\partial(\log_{10} I_{ds})} \qquad (5)$$

[turn-on voltage (V_{on})]

V_{on} parameter indicates V_{gs} value at which I_{ds} begins to increase.

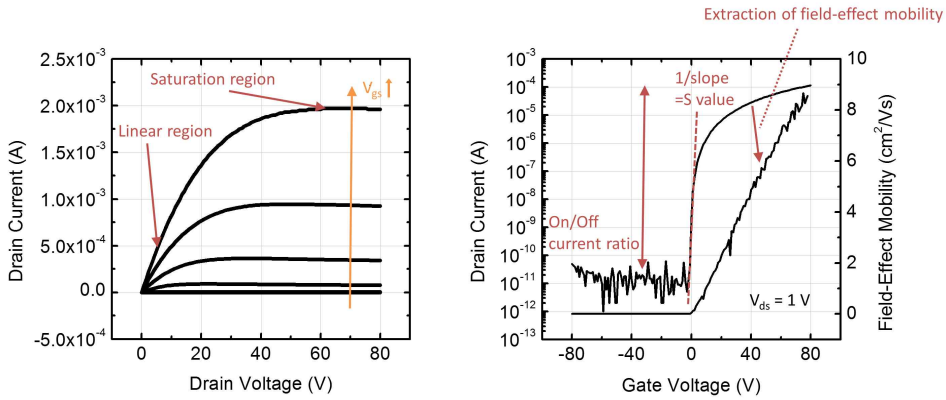

Figure 2.2 Output characteristics (Left) and transfer characteristics (Right) of TFT.

2.1.3 Structures of TFT and their properties

TFT structures are largely divided into four types. [2, 3] (Figure 2.3) Basically, staggered or coplanar structure can be distinguished by the definition of Weimer. It defined as coplanar structure if source-drain electrode and the gate electrode are in the same direction with respect to the semiconductor, or stagged structure if they are in the opposite direction. Top gate and bottom gate structure are distinguished by whether the gate electrode is above or below the structure. The bottom gate structure is sometimes referred to as an inverted structure.

In general, each structure is determined depending on the manufacturing conditions and characteristics of the semiconductor. The top gate structure is used when a semiconductor is fabricated in high temperature process. In this structure, there is an advantage that the insulator and the gate electrode protect the semiconductor region. However, since the gate electrode is generally located on the upper side, in the case of liquid crystal display (LCD), the semiconductor can be affected by the light from light source located at the lower side. On the other hand, in the case of organic light emitting display (OLED), light source can be located on the TFT, the top gate structure can be suitable. Therefore, the top gate structure is used for the poly silicon TFT applied to the OLED.

Meanwhile, in the case of the bottom gate structure, the surface of the semiconductor is generally exposed to air. Also, there is the possibility that semiconductor can be damaged during the

source-drain etching process. Accordingly, etch stopper is often used to overcome these problems. However, since the gate electrode can block the light coming from the lower side, amorphous silicon TFT used in the LCD process adopt this structure. The coplanar structure generally has a smaller contact resistance of the source and drain electrodes than that of the staggered structure. The coplanar or staggered structure can be determined depending on the etching condition of each layer and the manufacturing conditions.

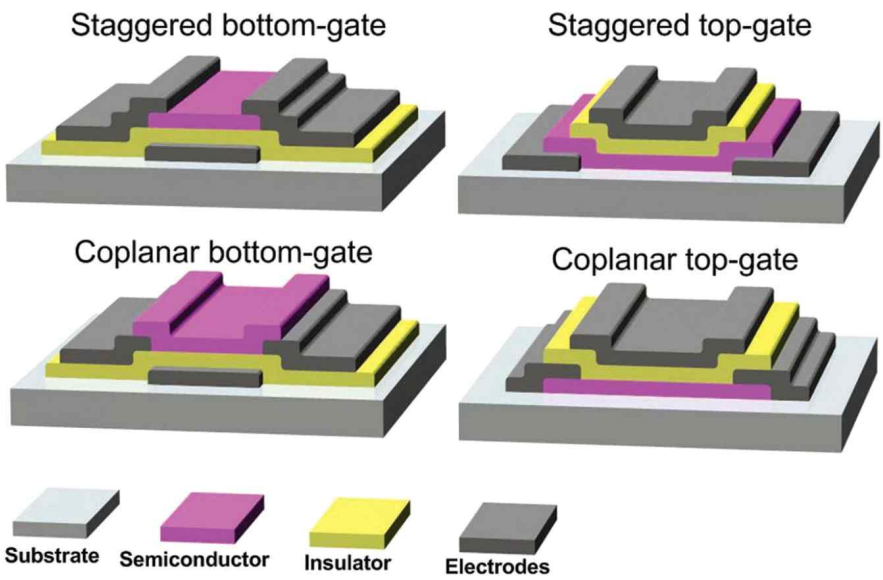

Figure 2.3 Structures of TFTs. [2]

2.2 Oxide semiconductor for TFT

Transparent and flexible properties are required in future displays. Accordingly, suitable TFTs for future displays are demanded. For this purpose, amorphous Si, poly Si, organic, and oxide semiconductor TFTs are suggested. Especially, oxide semiconductor TFT, which has transparent and flexible properties as well as high electrical properties, has been attracted as a promising switching device.

To date, Si-based TFTs such as hydrogenated amorphous silicon TFT and low-temperature polycrystalline silicon (LTPS) TFT have been widely applied in current display technology. Hydrogenated amorphous silicon TFT has a relatively low mobility (< 1 cm^2 V^{-1} s^{-1}). [4] Accordingly, it is not suitable for advanced display requiring high field-effect mobility. To overcome them, the development of high mobility TFTs is essential. LTPS TFT and oxide semiconductor TFT have attracted great interest. Although LTPS TFT has a high field-effect mobility of about 100 cm^2 V^{-1} s^{-1}, the LTPS TFT has considerable difficulty in applying to a practical and large-sized display because LTPS manufactured by an excimer laser beam has non-uniform electrical characteristics with a large-area [5]. Furthermore, this process requires expensive laser equipment and they have poor transparency which is a fatal drawback for future displays. On the other hand, oxide semiconductor TFTs have high electrical properties as well as unique properties such as transparency for applications in future displays. [6-8]

Oxide semiconductor is composed of a compound of metal cations

such as In, Zn, Ga and oxygen anions. Conduction band in oxide semiconductor is mainly composed of an large isotropic s orbital of a metal cation, and thus exhibits relatively high electric mobility characteristics in an amorphous state. [9] (Figure 2.4) This feature is a major difference from conventional silicon semiconductor formed by covalent bonds and exhibiting poor electrical properties in amorphous state. Accordingly, the oxide semiconduct TFT can be fabricated in low processing temperature. In addition, it exhibits a transparent property due to strong ionic bonding with a high Madelung potential. [10] (Figure 2.5) Therefore, oxide semiconductor TFT is expected to be applicable not only to a large-area and high-resolution display but also to a future device having transparency and flexibility (a transparent display, sensor, memory and the like).

Oxide semiconductor TFTs have been studied since the 1960s. However, TFT did not show good electrical characteristics. In 2003, TFTs using ZnO and InGaZnO (IGZO) showed good performance and oxide semiconductor TFTs have been focused. In particular, in 2004, the Hosono el. al. succeeded in fabricating amorphous IGZO TFTs at low temperatures on flexible substrates. [11] (Figure 2.6) Also, it is known that carrier concentration can be controlled in oxide semiconductors using Ga. Also, since then, with various analyses, unique electronic structure of IGZO about tail states, subgap states, and potential barriers was investigated. [11, 12] (Figure 2.7)

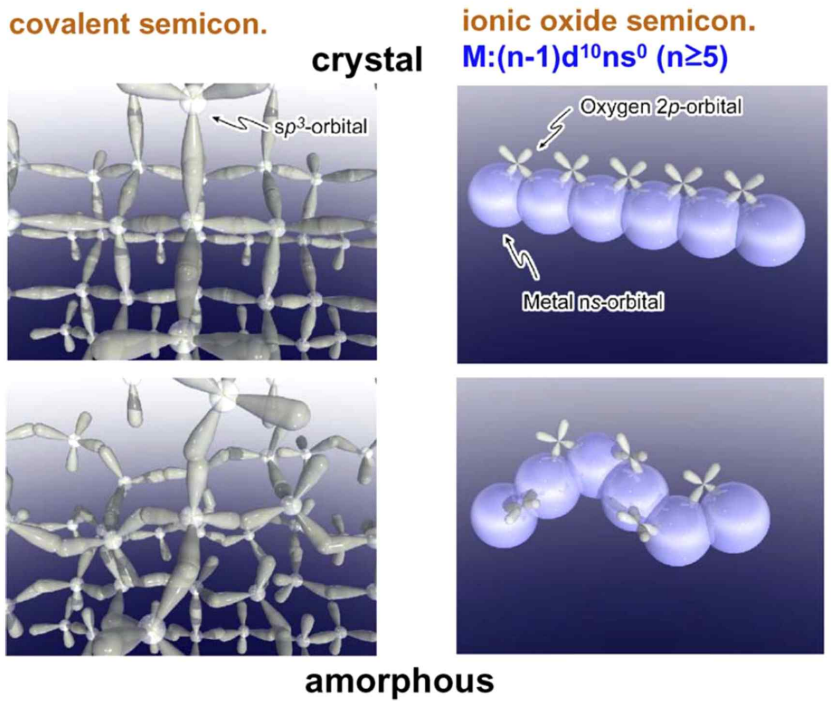

Figure 2.4 Structures of oxide semiconductor and Si-based semiconductor. [9]

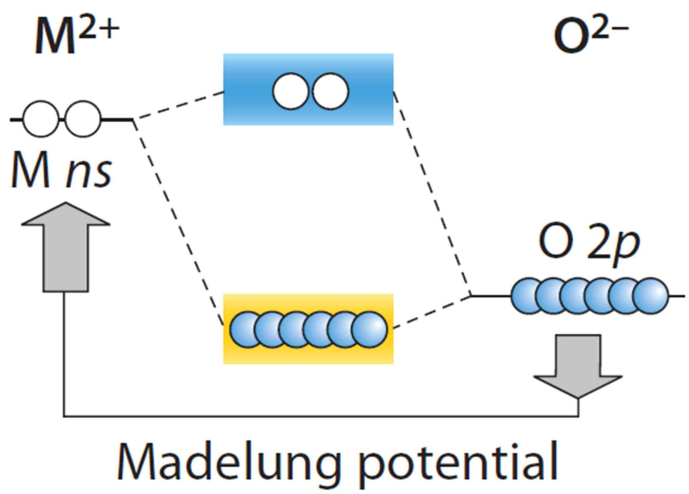

Figure 2.5 Bandgap formation of oxide semiconductor. [10]

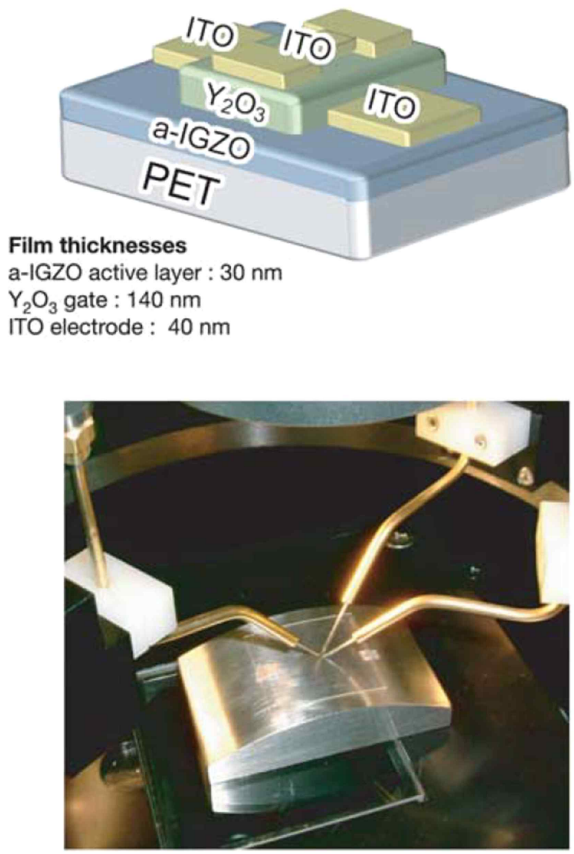

Figure 2.6 The example of IGZO TFT on flexible substrate. [11]

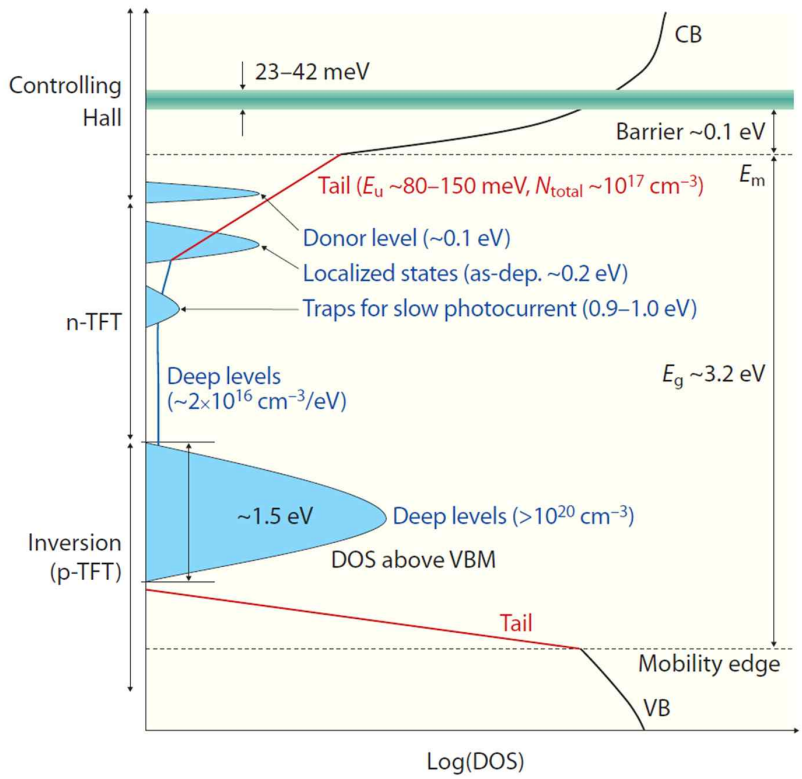

Figure 2.7 The electronic structure of amorphous IGZO semiconductor. [12]

2.3 Solution-process for oxide semiconductor TFT

Sputter deposition is one of representative methods to fabricate oxide semiconductor thin film due to their outstanding electrical and stable properties. However, it needs the high equipment investment cost, and conventional patterning process. [13, 14] Unlike the conventional vacuum process, the solution process uses a solution to fabricate a oxide semiconductor thin film. Accordingly, this process does not require a vacuum process facility. Also, since it can utilize techniques such as inkjet printing, a patterning process is not required. In addition, the continuous fabrication process is possible through the roll to roll process. Recent research on the solution process aims at producing not only oxide semiconductors but also dielectrics and electrodes in a broad sense.

Solution-processed oxide semiconductor TFTs have various advantages but exhibit relatively poor electrical characteristics compared with vacuum-processed oxide semiconductor TFTs. Recently, these problems are largely solved in three research directions.

(1) Development of oxide semiconductor TFT having high field-effect mobility

Since solution-processed oxide semiconductors are formed based on precursors and solvents, impurities affect the density, crystallinity, and the like in the formation of oxide thin films. Therefore, the

mobility, which is an important electrical property for TFT, can be reduced. In order to overcome this problem, various methods such as special precursors and doping method have been proposed. [15-18] This dissertation focuses the this problem.

(2) Development of high-performance oxide semiconductor TFT at low temperature process

In order to apply solution-processed oxide semiconductor TFT to plastic substrate, it is essential to form an oxide semiconductor thin film at a low temperature. Generally, a precursor used in a solution process can be decomposed and formed into an oxide semiconductor thin film only by heating at a specific high temperature. Recently researches through doping, novel precursors and ultraviolet (UV) method have been proposed for fabrication of oxide semiconductor thin films in a low temperature process. [6-8, 19]

(3) Understanding of solution-processed oxide semiconductor TFT for high electrical stability

The transistor, which is a switching device, basically requires electrical stability for repetitive operation. In the case of oxide semiconductor thin film fabricated by the conventional vacuum process, the physical properties and electrical stability can be controlled by adjusting the gas condition and the annealing

temperature. On the other hand, in the case of oxide semiconductor thin films fabricated by the solution process, the defects, physical property, and interfaces are changed by various variables such as the precursor type, annealing temperature and gas condition, resulting in the change in electrical stability. Systematic analyses of this are essential to enable commercialization of solution-processed oxide semiconductor TFT.

2.4 High mobility solution-processed oxide semiconductor TFT

2.4.1 The need of high mobility

For the development of advanced display such as ultra high resolution and large display, there remains a significant problem about device operation related with intrinsic resistance-capacitance (RC) delay. [20, 21] More TFTs in certain area of display fatally increase the intrinsic RC delay due to growth of parasitic capacitance coupling among gate electrodes, source-drain electrodes and pixel electrodes. (Figure 2.8) For decrease of intrinsic RC delay, as resistivity of transparent electrodes reach the limit in current technology, dielectric insulator and protection layer between interlayers should be designed to hold low capacitance. Even using the electrode with low resistivity such as Ag, Cu cannot be an alternative solution replacing low capacitance design in large scale display. However, reducing the capacitance for low capacitance TFT design intrinsically leads to lower operating current. In display technology such as high frame rate, high resolution and large scale, operating current of TFT should be increased for less charging time because one scanning period is decreased in high frame rate, high resolution display. For the reason, TFT should essentially have high field-effect mobility to realize low capacitance TFT design. Meanwhile, the cost problem should also be considered for application to high technology because a large number of pixels demand high-priced driver integrated circuits (ICs) as much.

Various circuits such as demultiplexer (DEMUX) circuit can be solution to reduce the number of driver ICs of display. [22-24] The various circuits enable 1 driver IC to function like several driver ICs through design of TFTs circuit. This means that switching speed of TFTs should be several times faster than existing TFTs. For the reason, high field-effect mobility property of TFT should be prepared to use application of various circuits for low cost fabrication.

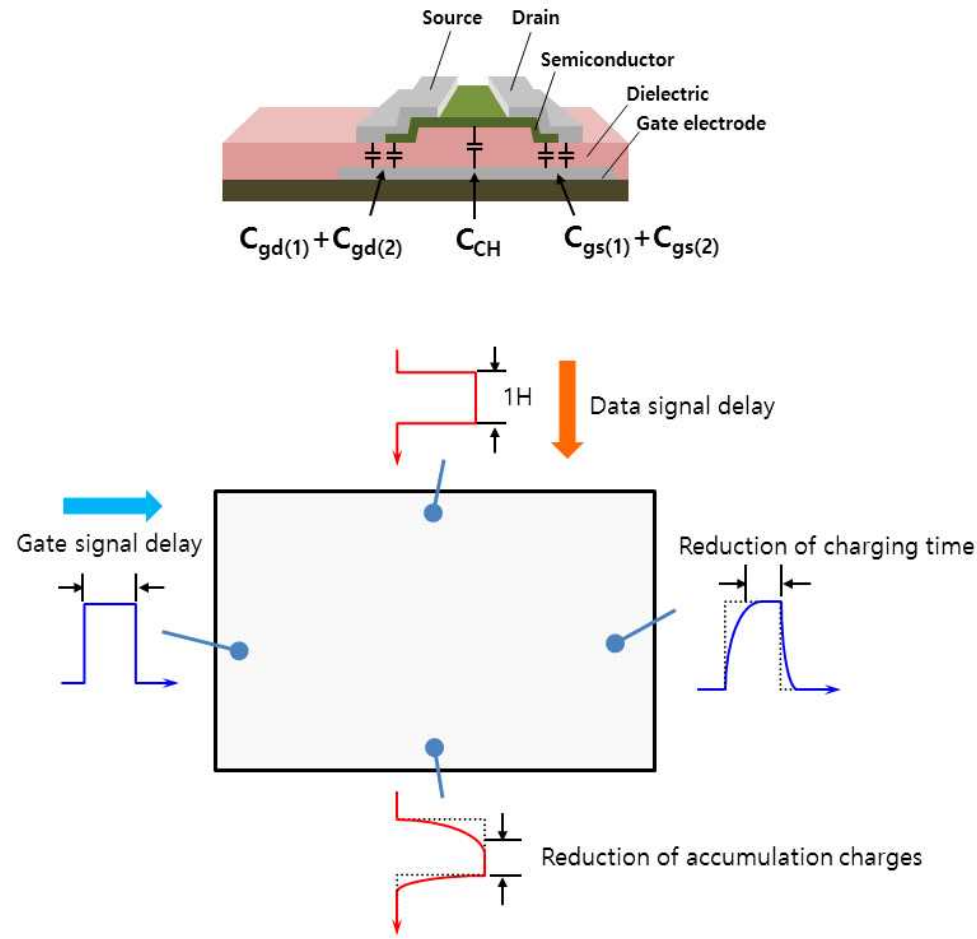

Figure 2.8 RC delay mechanism of TFT in display.

2.4.2 Trends and issues

Generally, solution-processed oxide semiconductors have a relatively large trap states due to the impurities of the precursor and the solvent compared with the vacuum process. With a lot of effort, solutions fabricated with precursors such as metal nitrates, metal acetates, and metal chlorides and solvents such as 2-methoxyethanol, and acetonitrile, have been developed for fabrication of solution-processed oxide semiconductor TFTs with high electrical performance. Nevertheless, the solution-processed oxide semiconductor TFT showed relatively low mobility compared to the vacuum-processed oxide semiconductor TFT.

To overcome this problem, various dopants, such as Li, Na, Zr, Sn, and Y have been proposed to enhance the electrical properties of solution-processed oxide semiconductors. Some results have shown a outstanding performance. [19, 25-28]

In recent years, research through structural changes has shown outstanding results. Yang group of the University of California in Los Angeles realized $InSn_xZn_yO_z$ (ITZO) TFT with high mobility (> 40 $cm^2\ V^{-1}\ s^{-1}$) through a double oxide layer structure (Figure 2.9) [17] In addition, Anthopoulos group of Imperial College showed a solution-processed oxide semiconductor TFT with high mobility (> 20$cm^2\ V^{-1}\ s^{-1}$) using super lattice structure. (Figure 2.10) [18] In the future, various researches are expected to be carried out in order to realize a higher mobility requirement for high performance display application.

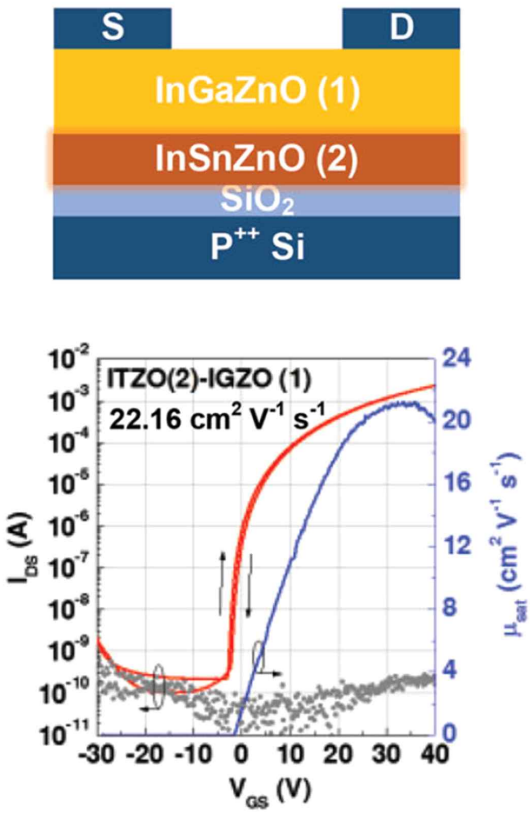

Figure 2.9 Solution-processed IGZO TFT with double layer method. [17]

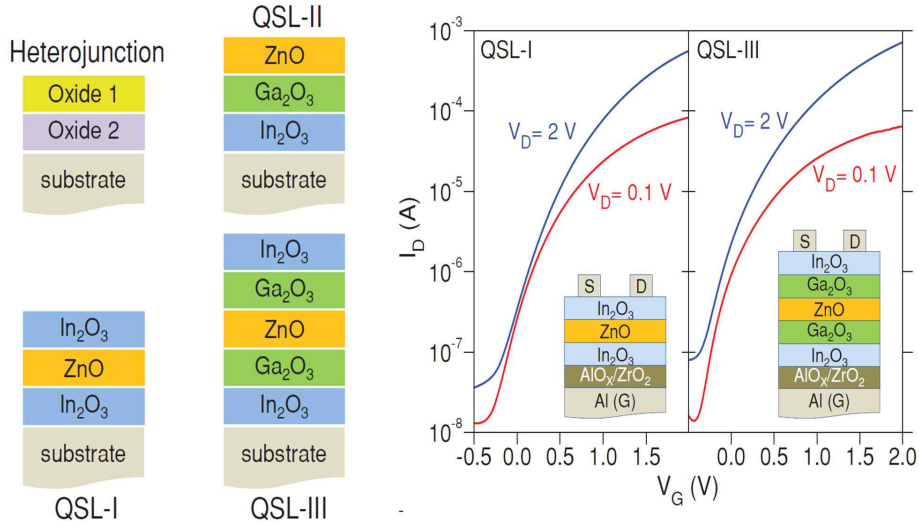

Figure 2.10 Solution-processed oxide semiconductor TFT with quasi-super lattice method. [18]

2.4.3 Alkali metal doping

In conventional MOSFET, dopant was used to change the amount of carrier concentration in semiconductor. Typically, the increase of the carrier concentration causes the impurity scattering, resulting in a decrease of the electron mobility. Otherwise, in oxide semiconductors, various dopant such as Li, Na, Zr, Sn, and Y have been studied for increasing the field-effect mobility. [19, 25-28] Among various dopant, alkali metal has attracted much attention due to their high mobility increasing properties.

In general, research on increasing the amount of carrier concentration by dopant with Li in ZnO has been conducted for a long time. Actually, research has been carried out to conduct ZnO into a conductor through such dopant. Zn of ZnO is ion-bonded in divalent cation state. [29, 30] Therefore, when Li is doped into the zinc oxide semiconductor as an interstitial doping, electrons are emitted. On the other hand, substitutional doping of the Zn atom reduces the amount of carriers.

$$Li = Li_i^+ + e^- \quad \text{(Interstitial doping)} \tag{6}$$

$$Li = Li_{zn} + h^+ \quad \text{(substitutional doping)} \tag{7}$$

Investigating the mechanism of alkali metal doping for enhancing the field-effect mobility in ZnO TFT or the ZnO-based oxide semiconductor TFT is one of the main issues. Most studies have

focused on the change in the morphology or the oxygen vacancy in ZnO-based metal oxide semiconductors depending on the alkali metal doping. However, the correlation between the alkali metal doping and the enhancement of the field-effect mobility in ZnO-based metal oxide semiconductors were not identified by the change in morphology or oxygen vacancy amount. To optimize the doping effect in ZnO-based oxide semiconductor, identifying the mechanism for the effects of alkali metal doping in ZnO-based oxide semiconductors TFTs has been required.

2.4.4 Dielectric engineering

Recently, there have been reported phenomena that the field-effect mobility of solution-processed oxide semiconductors is dramatically changed depending on specific solution-processed dielectrics such as AlO_x and ZrO_x. An interesting part of this phenomenon is that the oxide thin-film transistor through the solution process exhibits very high mobility electrical characteristics compared to the oxide semiconductor produced in the conventional vacuum process. Vivek Subramanian group at the University of California (Berkeley) implemented a solution-processed ZnO_x TFT with solution-processed ZrO_x, which has 20 times higher mobility than ZnO_x TFTs on SiO_2 insulators. [31] In addition, Lian Duan group in Tsinghua University of China developed SnO_x TFT with mobility of about 90 $cm^2\ V^{-1}\ s^{-1}$ using solution-processed AlO_x insulator. [32]

Recently, it is found that this phenomenon depends on the interfacial properties of oxide semiconductors, by deriving the theoretical TFT model. [33] In conventional semiconductor device physics, when the electric field induced by a gate voltage is applied to the TFTs, most charges accumulate near the interface between the semiconductor and the dielectric. Therefore, the field-effect mobility of TFTs is mostly determined by the interface properties between semiconductor region and dielectric region. However, there has been no systematic approach on the change in interfaces according to specific dielectrics yet.

2.5 References

[1] Correia, A. P. Pinto, C. Barquinha, P. Miguel, Goes, J. C. D. Palma, A Second-Order ΣΔ ADC Using Sputtered IGZO TFTs. Springer, 2016

[2] E. Fortunato, P. Barquinha, R. Martins, Adv. Mater. 2012, 24, 2945.

[3] J. S. Park, W.-J. Maeng, H.-S. Kim, J.-S. Park, Thin Solid Films 2012, 520, 1679

[4] W. E. Spear, P. G. Lecomber, Solid State Commun. 1993, 88, 1015.

[5] T. Kamiya, K. Nomura, H. Hosono. Sci. Technol. Adv. Mater. 2010, 11, 044305.

[6] Y.-H. Kim, J.-S. Heo, T.-H. Kim, S. Park, M.-H. Yoon, J. Kim, M. S. Oh, G.-R. Yi, Y.-Y. Noh, S. K. Park, Nature, 2012, 489, 128.

[7] M.-G. Kim, M. G. Kanatzidis, A. Facchetti, T. J. Marks , Nat. Mater. 2011, 10, 382.

[8] K. K. Banger, Y. Yamashita, K. Mori , R. L. Peterson, T. Leedham, J. Rickard, H. Sirringhaus, Nat. Mater. 2011, 10, 45.

[9] H. Hosono, J. Non-Cryst. Solids, 2006, 352, 851.

[10] T. Kamiya, H. Hosono, Npg Asia Mater. 2010, 2, 15.

[11] K. Nomura, H. Ohta, A. Takagi, T. Kamiya, M. Hirano, H. Hosono, Nature 2004, 432, 488.

[12] T. Kamiya, K. Nomura, H. Hosono, J. Disp. Technol. 2009, 5, 462.

[13] K.-H. Lim, K. Kim, S. Kim, S. Y. Park, H. Kim, Y. S. Kim, Adv. Mater. 2013, 25, 2994.

[14] K.-H. Lim, J.-E. Huh, J. Lee, N.-K. Cho, J.-W. Park, B.-I Nam, E. Lee, Y. S. Kim, ACS Appl. Mater. Interfaces, 2017, 9, 548.

[15] D. H. Lee, Y. J. Chang, G. S. Herman, C. H. Chang, Adv. Mater. 2007, 19, 843.

[16] J. Jang, R. Kitsomboonloha, S. L. Swisher, E. S. Park, H. Kang, V. Subramanian, Adv. Mater. 2013, 25, 1042.

[17] Y. S. Rim, H. J. Chen, X. L. Kou, H. S. Duan, H. P. Zhou, M. Cai, H. J. Kim, Y. Yang, Adv Mater 2014, 26, 427.

[18] Y.-H. Lin, H. Faber, J. G. Labram, E. Stratakis, L. Sygellou, E. Kymakis, N. A. Hastas, R. Li, K. Zhao, A. Amassian, N. D. Treat, M. McLachlan, T. D. Anthopoulos, Adv. Sci. 2015, 1500058.

[19] S. Y. Park, B. J. Kim, K. Kim, M. S. Kang, K. H. Lim, T. Il Lee, J. M. Myoung, H. K. Baik, J. H. Cho, Y. S. Kim, Adv. Mater. 2012, 24, 834.

[20] J. Y. Kwon, K. S. Son, J. S. Jung, T. S. Kim, M. K. Ryu, K. B. Park, B. W. Yoo, J. W. Kim, Y. G. Lee, K. C. Park, S. Y. Lee, J. M. Kim, IEEE. Electron Device Lett. 2008, 29, 1309

[21] J. C. Park, S. W. Kim, S. I. Kim, H. Yin, J. H. Hur, S. H. Jeon, S. H. Park, I H. Song, Y. S. Park, U I. Chung, M. K. Ryu, S. Lee, S. Kim, Y. Jeon, D. M. Kim, D. H. Kim, K.-W. Kwon, C. J. Kim, IEDM Tech. Dig., Dec. 2009, 7-9, 1-4

[22] J.-J Lih, C.-F. Sung, C.-H Li, T.-H. Hsiao, H.-H. Lee, J. Soc. Inf. Disp. 2004, 12, 367.

[23] Y.-J. Yun, B.-G. Jun, Y.-K. Kim, J.-W. Lee, Y.-M. Lee , Displays, 2009, 30, 17

[24] E. Fukumoto, T. Arai, N. Morosawa, K. Tokunaga, Y. Terai, T. Fujimori, T. Sasaoka, J. Sco. Inf. Disp. 2011, 19, 867

[25] C. Koo, K. Song, Y. Jung, W. Yang, S. Kim, S. Jeong, J. Moon, Acs Appl. Mater. Inter. 2012, 4, 1456.

[26] S. J. Seo, C. G. Choi, Y. H. Hwang, B. S. Bae, J. Phys. D Appl. Phys. 2009, 42, 035106.

[27] H. S. Shin, G. H. Kim, W. H. Jeong, B. Du Ahn, H. J. Kim, Jpn. J. Appl. Phys. 2010, 49, 03CB01.

[28] Y. S. Rim, D. L. Kim, W. H. Jeong, H. J. Kim, Electrochem. Solid St. 2012, 15, H37.

[29] G. Lefe`vre, M. Duc, P. Lepeut, R. Caplain, M. Fe´doroff, Langmuir, 2002, 18, 7530.

[30] F. Torricelli, J. R. Meijboom, E. Smits, A. K. Tripathi, M. Ferroni, S. Federici, G. H. Gelinck, L. Colalongo, Z. M. Kovacs-Vajna, D. de Leeuw, E. Cantatore, IEEE Trans. Electron Devices. 2011, 58, 2610.

[31] A. Zeumault, V. Subramanian, Adv. Func. Mater. 2016, 26, 955.

[32] G. Huang, L. Duan, G. Dong, D. Zhang, Y. Qiu, Appl. Mat. Interfaces. 2014, 6, 20786.

[33] E. Lee, J. Ko, K.-H. Lim, K. Kim, S. Y. Park, J. M. Myoung, Y. S. Kim, Adv. Func. Mater. 2014, 24, 4689.

Chapter 3. High Performance Amorphous Zinc Tin Oxide Thin-Film Transistor through Alkali Metal Doping

3.1 Overview

Recently, TFTs including various oxide semiconductors, such as In, Ga and Zn oxide, have attracted great interest for the switching devices for the next generation display such as smart window, transparent electronic wall, mobile display and smart sign. [1,2] In comparison with Si semiconductor, which is widely used in the display industry, metal oxide semiconductors show high electrical performance as well as unique properties such as transparence induced by the wide bandgap. [3]

Generally, in the application to TFTs, oxide semiconductors are deposited as a film on substrates by various vacuum techniques, such as pulsed laser deposition (PLD), [4] radio frequency (RF) sputtering, [5] and atomic layer deposition (ALD), [6] all of which have ensured outstanding electrical performance. Also, metal oxide semiconductors have good potential for use in printed electronics through various solution precursors. [7, 8] Recently, some remarkable results have been reported on the use of various solution precursors in ambient conditions for the fabrication of semiconductor in TFTs. [7, 9 ,10]

Thus, oxide semiconductor TFTs, such as In, Ga, and Zn oxides, have shown good potential for advanced TFTs in a next-generation display. [10-13] However, the use of In and Ga has latent problems

because of their high cost. In addition, there remains a serious issue in the use of In, which shows an uneven deposit and thus has become a strategically important material. For the indium-free oxide semiconductor, various dopants, such as Li, Sn, Y and Zr, have been introduced to improve the semiconducting property of ZnO-based oxide semiconductor and have shown good electrical performance. [7, 14-17] In particular, among the various dopants, alkali metals, such as Li and Na, have received much attention due to their high field effect mobility, good electrical stability in TFTs and compatiblility with a ZnO-based metal oxide semiconductor precursor solution. [7,14]

Meanwhile, the mechanism of alkali metal doping for enhanced mobility is one of main issues in the ZnO semiconductor or the ZnO-based oxide semiconductors. Most studies have only focused on the fluctuation of the morphology or the oxygen vacancy amount of alkali metal-doped ZnO-based oxide semiconductors. However, the correlation between doping concentration and enhancement of electrical performance of ZnO or the ZnO-based oxide semiconductors were not successfully explained by the analysis of the fluctuation of the morphology or the variation of oxygen vacancy amount. The absence of the exact mechanism analysis for alkali metal doping effect has undetermined the potential of the alkali metal doped ZnO-based oxide semiconductors TFTs.

In addition, a technique for monitoring on the electrical performance of the ZnO-based oxide semiconductors is essential in order to apply

the ZnO-based oxide TFTs to industry. Some techniques, such as Hall measurements, have been widely used to confirm the electrical properties of metal oxide semiconductor. However, because of surface roughness, Hall measurement is not easily applicable to ZnO-based oxide semiconductor films fabricated by the solution process. [18] Furthermore, the destructive methods, such as the electrode deposition used in Hall measurement, are not efficient as an industrial monitoring technique. For the faithful understanding for the electrical enhancement of the ZnO-based oxide semiconductors by alkali metal doping, the successful development of a monitoring technique on the variation of electrical performance in the ZnO-based oxide semiconductor TFTs is essential. In this reason, spectroscopy techniques, such as ultraviolet (UV)-visible spectroscopy, are worthy of note as a fast and non-destructive analysis. In conventional Si semiconductor TFTs, the opaque property hinders the use of UV-visible spectroscopy analysis. Otherwise, in the ZnO-based oxide semiconductors TFTs, UV-visible spectroscopy analysis can be simply used as analysis tool because of their unique optical property like transparence.

Here in, I newly introduce the solution-processed and alkali metals, Li and Na, doped amorphous zinc tin oxide (ZTO) semiconductor TFTs, which showed the better electrical performance, such as field effect mobility, than that of intrinsic amorphous ZTO semiconductor TFTs. I also successfully analyze the doping mechanism of alkali metals in the amorphous ZTO semiconductor through various

techniques such as X-ray photoemission spectroscopy (XPS), atomic force microscopy (AFM), Hall mobility and so on. Furthermore, using spectroscopic UV-visible analysis, I suggest the comprehensive monitoring technique for the variation of electrical performance of ZTO semiconductor induced by alkali metal doping in terms of the optical bandgap shift. Most importantly, this UV-visible spectroscopic analysis for monitoring the electrical performance of oxide semiconductor TFTs has good potential as a high fast and non-destructive analytical method.

3.2 Development of alkali metal doped ZTO TFTs and electrical properties

The alkali metal doped ZTO thin films were prepared by precursor solution, including zinc, tin, and alkali metals. The details are introduced in the Experimental details section. The precursor solution, including alkali metal ions of different molar ratios, was spin-coated onto 200 nm SiO_2 /Si wafer, and then heated at 500 °C for sintering. The alkali metals, Li and Na, doped amorphous ZTO films were analyzed by scanning electron microscopy (SEM), AFM, x-ray diffraction (XRD), high-resolution tunneling electron microscopy (HRTEM). Note that there were no significant changes in the surface morphology and in the structure in regard to alkali metal doping, as confirmed by SEM, AFM, XRD, HRTEM. (See Figure 3.1, 3.2, and 3.3) I also fabricated the TFTs including alkali metal-doped ZTO semiconductor films. The details of dimensions and process conditions for alkali metal-doped ZTO TFTs are introduced in Experimental details section. In the concise and comprehensive study on doping effects, I mainly focused on the effect of Li, among alkali metals, as a dopant in amorphous ZTO semiconductor TFTs. Figure 3.4 (a) shows the drain current versus the gate voltage derived by the semiconductor parameter analyzer of Li-doped ZTO TFTs depending on doping concentrations. Table 3.1 summarizes the values of average electrical performance of twenty-five Li-doped ZTO TFTs fabricated by one-run. The electrical properties containing threshold voltage and saturation field effect mobility were derived using a linear fit of the

plot of square root I_d at the saturation region.

All transfer curves were measured from -60 V to 60 V with a 60 V drain voltage. Figure 3.4 (b) shows the average field-effect mobility of the solution-processed alkali metals, Li and Na doped ZTO TFTs in comparison with that of solution-processed intrinsic ZTO TFTs. Interestingly, a systematic increase in I_d at a fixed V_g was observed upon the case of the ZTO semiconductor doped with Li and Na up to several mol%. These results demonstrated that alkali metal doping improves the electron transport of amorphous ZTO semiconductor. However, the introducing a greater amount of alkali metals into ZTO semiconductor resulted in a decrease of I_d, and they actually hampered electron transport. In the case of Li doping, I_d at a gate voltage of 60 V was increased by four times upon the initial adding of Li (0 - 5 mol%) and then decreased upon more being added (11 mol%). The Li-doped ZTO TFTs showed an average field effect mobility of 3.99, 8.04, 7.66, 5.31, and 2.68 $cm^2\ V^{-1}\ s^{-1}$ at 0 mol%, 2 mol%, 5 mol%, 8 mol%, and 11 mol%, which corresponded to the Li doping concentrations, respectively. In addition, the Na-doped ZTO TFTs showed 4.3, 4.62, 5.28, and 3.4 $cm^2\ V^{-1}\ s^{-1}$ at 0.5 mol%, 2 mol%, 5 mol%, and 8 mol%, which corresponded to the Na doping concentrations.

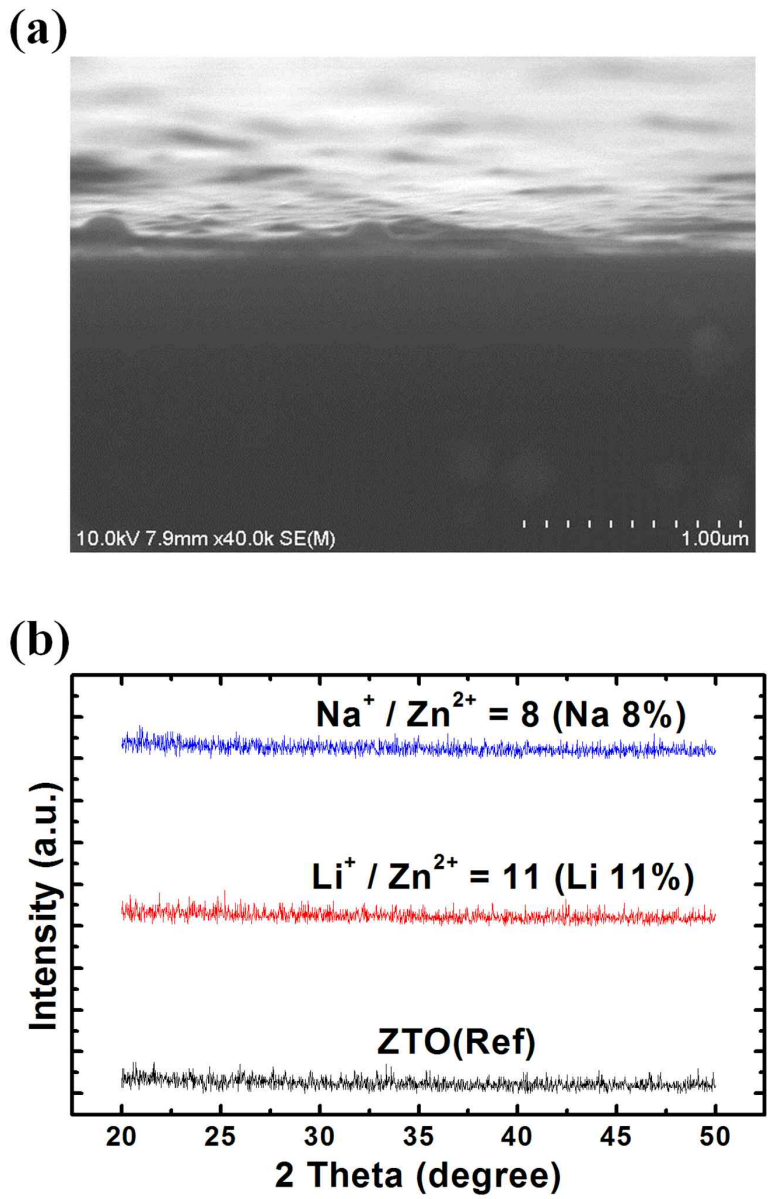

Figure 3.1 (a) The scanning microscopy image of ZTO film and (b) the X-ray diffractogram of the intrinsic ZTO and alkali metal doped ZTO films.

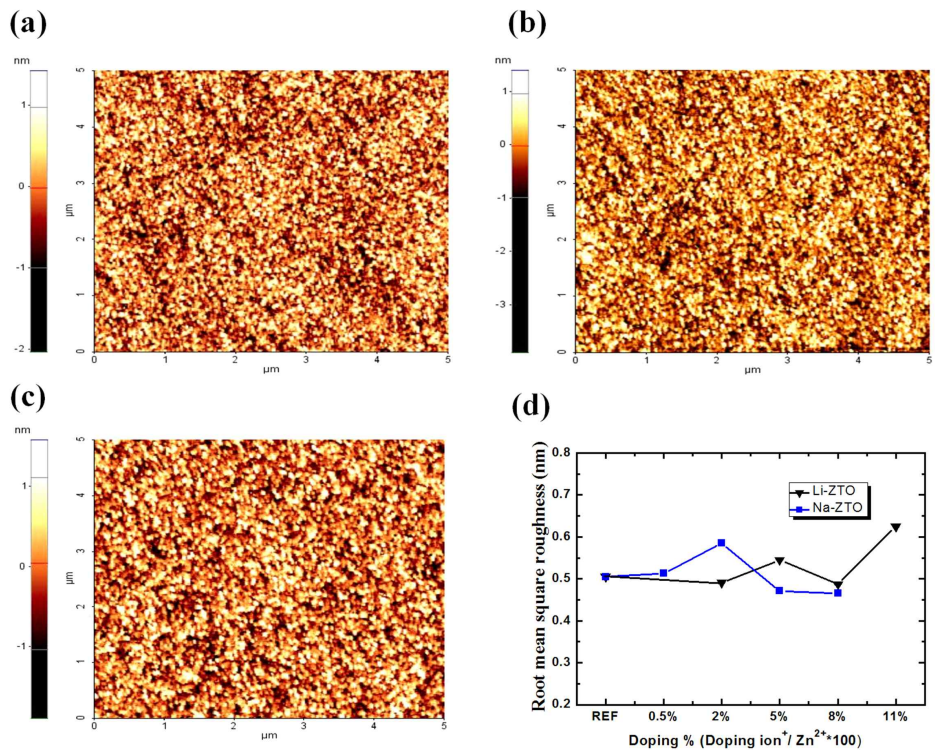

Figure 3.2 (a) The atomic force microscopy (AFM) image of intrinsic ZTO, (b) 2 mol% Li doped ZTO and (c) 11 mol% Li doped ZTO and (d) the average surface roughness root mean squre (RMS) data of doped ZTO film surface as an increase of alkali metals concentration.

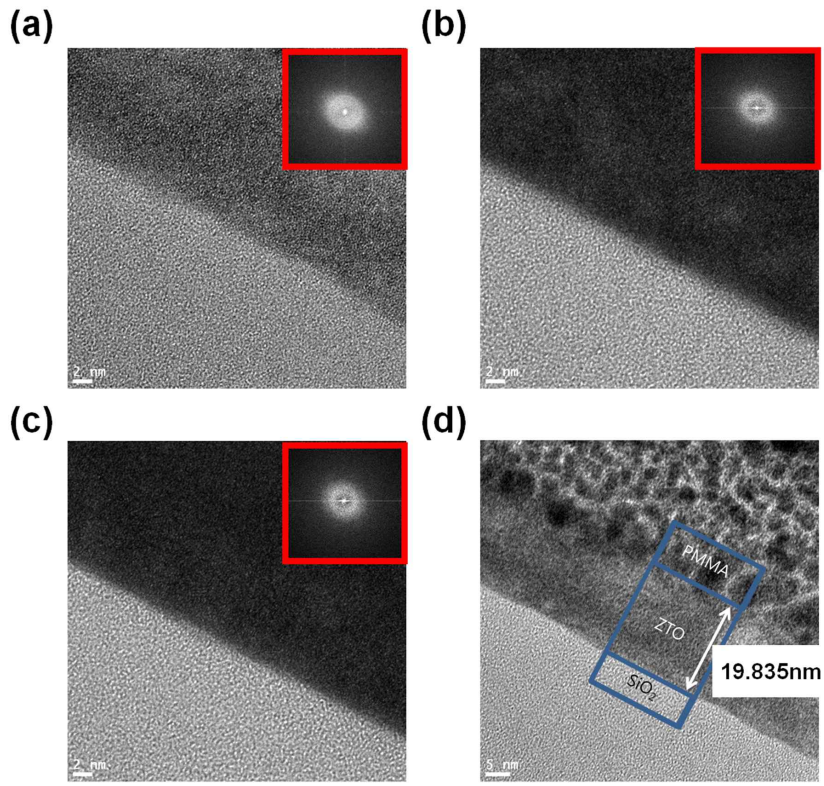

Figure 3.3 (a) The High resolution-tranmission electron microscopy (HR-TEM) images of the intrinsic ZTO film, (b) 2 mol% doped ZTO film and (c) 11 mol% Li doped -ZTO film. (d) The HR-TEM cross-section image of ZTO film.

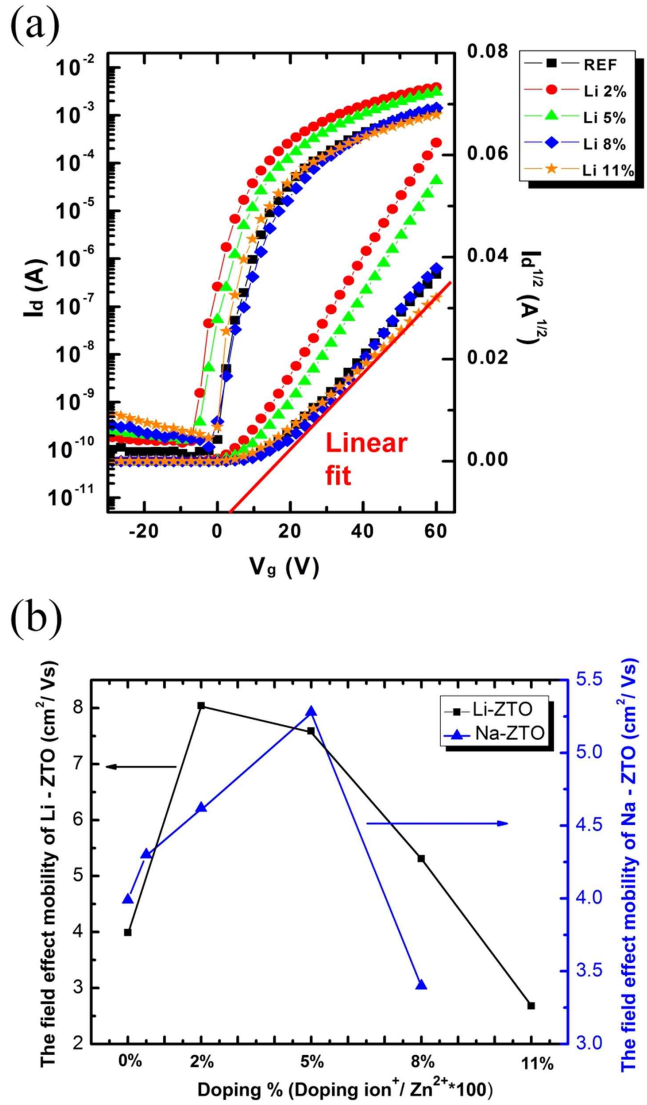

Figure 3.4 (a) The transfer characteristics of the intrinsic ZTO TFT and Li- doped ZTO TFTs and (b) the average field effect mobilities of the intrinsic ZTO TFT and alkali metals, Li and Na, doped ZTO TFTs.

	μ (cm^2 V^{-1} s^{-1}) <σ>	Threshold voltage (V) <σ>	on/off current ratio
ZTO	3.99 <0.55>	10.52 <3.28>	10^7
2 mol% Li-ZTO	8.04 <1.12>	6.41 <6.26>	10^7
5 mol% Li-ZTO	7.66 <0.99>	8.18 <6.98>	10^7
8 mol% Li-ZTO	5.31 <0.86>	9.29 <7.63>	10^7
11 mol% Li-ZTO	2.68 <0.47>	12.12 <8.52>	10^7

Table 3.1 The average field effect mobility, threshold voltage, and on/off current ratio of twenty-five intrinsic/Li-doped ZTO TFTs fabricated by one-run.

3.3 Analysis of chemical properties of alkali metal doped ZTO through XPS

In order to analyze the relationships between field effect mobility and oxygen vacancy content, I investigated the change of the O1s spectra of Li-doped ZTO semiconductor films in XPS spectra. Figure 3.5 show the O 1s XPS spectra of the intrinsic ZTO semiconductor film, 2 mol% Li-doped ZTO semiconductor film and 11 mol% Li-doped ZTO semiconductor film, respectively. The peaks that were fitted using Gaussian fitting were centered at 530.1 eV, which represents the oxygen bonds from oxide without oxygen vacancy (M-O), 531.08 eV, which represents the oxygen bonds with oxygen vacancy (O_{vac}), and 532.1 eV, which represents the oxygen bonds in the hydroxide (OH), respectively. [19] When the intrinsic ZTO semiconductor film and 2 mol% Li-doped ZTO semiconductor film were compared, the 2 mol% Li-doped ZTO film showed lower intensity in oxygen vacancy. In addition, in the case of the relationship between the 11 mol% Li-doped ZTO film and the intrinsic ZTO film, the 11 mol% Li-doped ZTO film relatively showed lower oxygen vacancy intensity than that of the intrinsic ZTO film (Figure 3.5). In this study, electrical properties, such as field effect mobility, did not coincide with the tendency of the oxygen vacancy peaks in the XPS spectra. Otherwise, as the doping concentration increased, the amount of oxygen vacancy decreased slightly in a direct correlation.

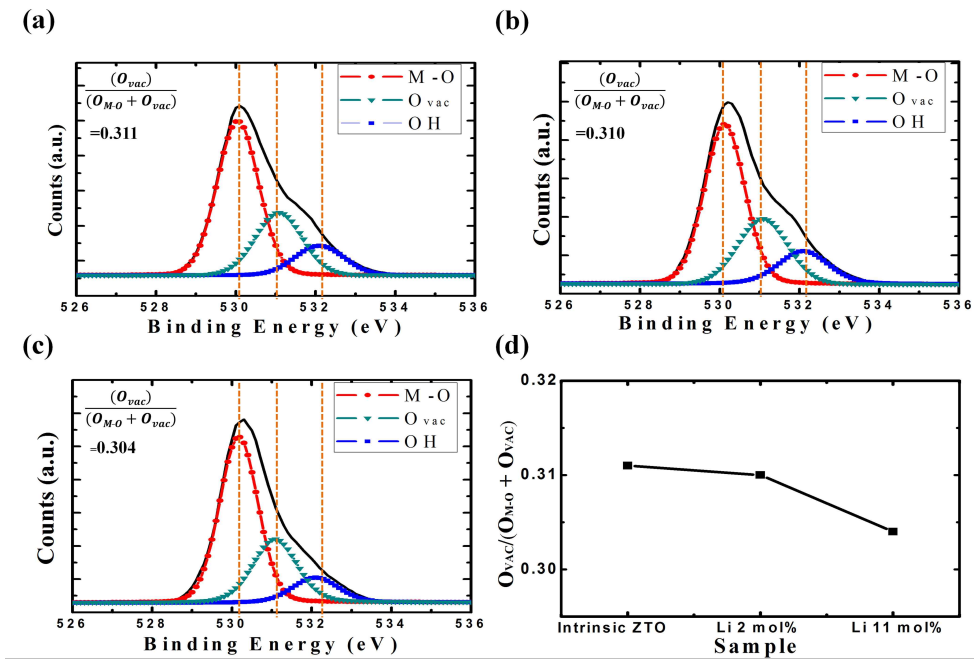

Figure 3.5 (a) The O 1s XPS spectra of the intrinsic ZTO film, (b) 2 mol% Li-doped ZTO film, (c) 11 mol% Li-doped ZTO film, and (d) the intensity ratio between oxygen vacancy intensity (O_{vac}) and the sum of oxygen vacancy intensity (O_{vac}) and oxygen intensity of metal oxide (M-O).

3.4 The study for role of alkali metal doping based on analyses

In previous reports, in both cases of Li interstitial and Li substitutional doping, the blue emission induced by oxygen vacancy is suppressed in both cathode-luminescence and photoluminescence, because the incorporation of Li into oxide semiconductor films causes the oxygen-enrichment of the surface. [20, 21] It is related to the lowering of the intensity peak of oxygen vacancy in the XPS spectra. Meanwhile, several researchers showed the increment of carrier concentration in proportion to the increase of oxygen vacancy amount. [11, 14] However, although the oxygen-enrichment of the surface cause the decrease of oxygen vacancy amount, the Li interstitial doping can induce faithfully the increase of carrier concentration in ZTO semiconductor films. In our XPS data, the variations of intensity of oxygen vacancy seem not to be enough to explain the influence on the electrical properties of ZTO semiconductor. In this study, I found that the variation of carrier concentration caused by the interstitial alkali metal doping influences more considerably on the electrical performance of ZTO semiconductor. Also, as the difference in the XPS spectra was too small, it was difficult to confirm the correlation between the enhancement of the electrical properties induced by Li interstitial doping and the changes in O 1s XPS spectra intensity. Although many researchers have suggested a correlation between oxygen vacancy contents and electrical performance in oxide semiconductor TFTs, [11, 14] it seems not to be sufficient to explain

in detail the mechanisms of the enhanced electrical performance of alkali metal doped oxide semiconductors. In addition, several reports have recently showed incompatible tendencies with regard to oxygen vacancy theory for electrical performance in oxide semiconductor. Thus, other mechanisms are required to clearly explain the electrical properties of amorphous ZTO TFTs related to doping with alkali metals.

Figure 3.6 (a) and (b) show the electrical properties of intrinsic ZTO TFTs and Li-doped ZTO TFTs which are measured by Hall measurement. One is the changes of threshold voltage and carrier concentration, and the other is the changes of the electrical conductivity and Hall mobility. As Figure 3.6 shows, the trade-off phenomena that coincided with the change in field effect mobility in TFTs depending on Li concentrations were clearly indicated. Table 3.2 summarizes the details of the electrical properties by Hall measurement. The threshold voltage at 2 mol% Li-doped TFTs negatively shifted from 10.52 to 6.41 V and then reduced the shift values according to the increment of Li doping concentration. On the other hand, in terms of the carrier concentration, when 2 mol% Li-doped ZTO showed the highest and then decreased. (Figure 3.6 (a)) The negative shift of threshold voltage can be explained by the increase of carrier concentration, because the charge density in the channel layer corresponds to the threshold voltage. [22] In brief, the negative shift of threshold voltage is considered in terms of the increased carrier concentration. Similarly, Hall mobility and electrical

conductivity showed the same tendency with the change of carrier concentration depending on Li doping concentrations (Figure 3.6(b)). Field effect mobility in case of the conventional covalent bonding semiconductor as Si is decreased by the increment of carrier concentration due to the carrier scattering effect. [3] Otherwise, field effect mobility in the Li-doped ZTO TFTs is increased by the increment of carrier concentration. These phenomena can be explained by the percolation conduction model. [23, 24] Previously, Hosono et. al. already proved that the electron mobility is enhanced in proportion to the carrier concentration in the oxide semiconductors. In the region of percolation conduction, the increment of carrier concentration enhances the field effect mobility in oxide semiconductors. [23, 24] Field effect mobility and carrier concentration in ZTO semiconductors were increased at 2 mol% and 5 mol% Li doping and then decreased at an excess of Li doping.

Considering the tendencies of XPS spectra and carrier concentration, the electrical trade-off at the Li doping can be deduced in relation to interstitial doping. The interstitial doping of Li in ZTO can be expressed by Equation (6), and the substitutional doping of Li in ZTO can be represented by Equation (7)

Actually, Li forms the interstitial defects more easily than the substitutional exchange of Zn in the zinc oxide matrix. [25] In the case of the ZnO PLD process under moderate partial pressure of oxygen and low Li concentration, interstitial doping is dominant on Li doping in zinc oxide matrix, because the energy of the Li interstitial

doping is lower than the energy of the Li substitution exchange. [26] I think that the electrical properties were considerably changed in the trade-off point between the interstitial Li doping and substitutional Li doping. At 11 mol% Li-doped ZTO, although interstitial doping occurred, substitutional Li doping occurred both simultaneously and considerably. As a result, field effect mobility was reduced by the neutralization of the holes, which were induced by the substitutional doping (Equation (7)), and the electrons, which were induced by interstitial doping (Equation (6)). The average field effect mobility of Li-doped ZTO TFTs showed the improvement and then the degradation depending on the concentration of Li (Figure 3.4 (b)). In general, the concept of an interstitial atom is principally explained in the crystalline structure. However, several researchers have reported interstitial doping in amorphous silicon or amorphous oxide semiconductors. [27, 28]

In conventional MOSFET, the doping phenomenon occurs with small amount doping atoms. On the other hand, oxide semiconductor typically needs large amount of doping atoms for inducing the doping phenomenon. [26] It is considered that the alkali metal atoms are not all involved in the doping phenomenon. Importantly, although many alkali metal are added in oxide semiconductor, the structure of oxide semiconductor is not changed, which means that alkali metal doping in oxide semiconductor does not lead to alloy process. [29]

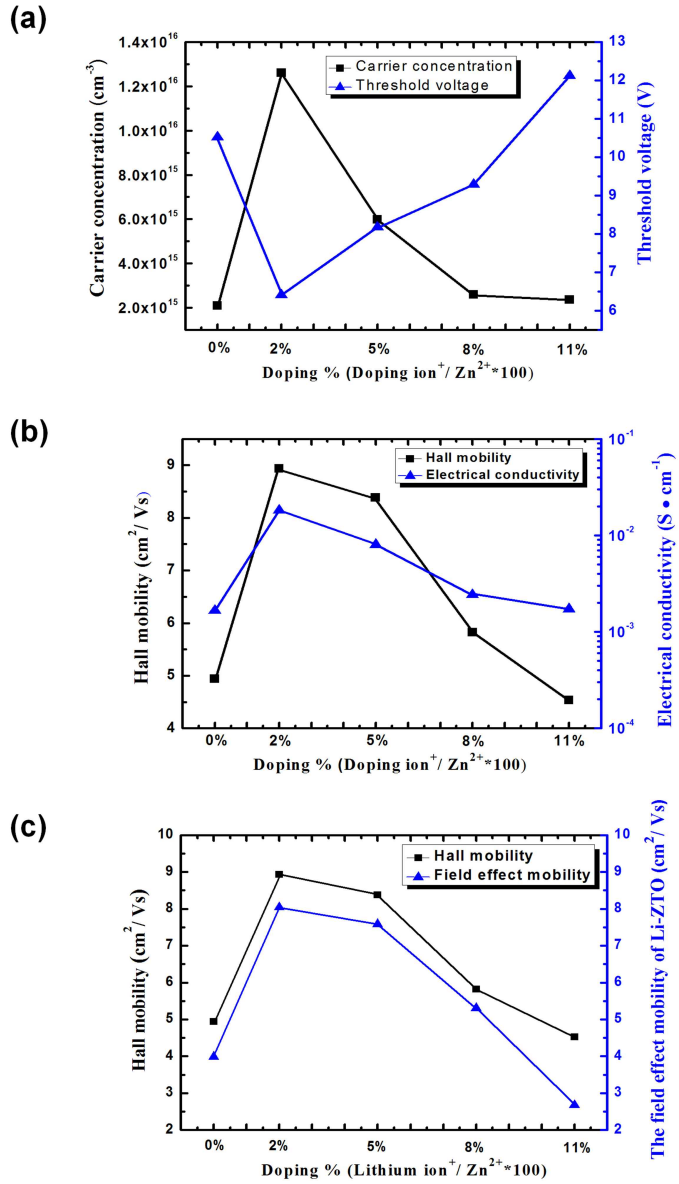

Figure 3.6 (a) Threshold voltage and carrier concentration, (b) electrical conductivity and Hall mobility, and (c) Hall mobility and field effect mobility of the intrinsic ZTO TFTs and Li-doped ZTO TFTs.

	Hall mobility ($cm^2\ V^{-1}\ s^{-1}$)	Carrier concentration (cm^{-3})	Conductivity ($S\ cm^{-1}$)
ZTO	4.94	$2.09 \cdot 10^{15}$	$1.66 \cdot 10^{-3}$
2 mol% Li-ZTO	8.93	$1.26 \cdot 10^{16}$	$1.81 \cdot 10^{-2}$
5 mol% Li-ZTO	8.38	$5.98 \cdot 10^{15}$	$8.03 \cdot 10^{-3}$
8 mol% Li-ZTO	5.82	$2.59 \cdot 10^{15}$	$2.42 \cdot 10^{-3}$
11 mol% Li-ZTO	4.53	$2.36 \cdot 10^{15}$	$1.72 \cdot 10^{-3}$

Table 3.2 Hall mobility, carrier concentration, and conductivity of intrinsic and Li-doped ZTO semiconductor films.

3.5 The investigation of the role of alkali metal doping through UV-visible spectroscopy

Figure 3.7 (a) and Figure 3.8 shows the transmittance spectra of the intrinsic ZTO film and alkali metal-doped ZTO films on quartz substrate through UV-visible spectroscopy. Slight blue shifts in the transmittance of Li-doped ZTO films from that of intrinsic ZTO films were observed (inset image of Figure 3.7 (a)). The optical bandgap, E_g^{opt}, can be obtained by the absorption coefficient (α). The α coefficient can be obtained by Equation (8) [30, 31] as follows:

$$\alpha = \frac{1}{d} ln\left(\frac{1}{T}\right) \qquad (8)$$

, where d and T represent the film thickness and transmittance, respectively. The thickness of Li-doped ZTO films is about 20 nm. In addition, the optical bandgap, E_g^{opt}, can be expressed by the Tuac relation [31, 32] as follows:

$$(\alpha h\nu)^m = A(h\nu - E_g) \qquad (9)$$

, where h is Planck's constant, and v is the photon frequency. The value of m is commonly 1/2 at the amorphous semiconductor in the case of a non-direct semiconductor. [32] The optical bandgap of intrinsic ZTO is about 3.3 eV (see the inset image in Figure 3.7 (b), Figure 3.9). However, to show a precise description of the optical bandgap edge, we applied the m value, m=2, induced by the direct semiconductor model. (Figure 3.7 (b)) Generally, in order to determine the difference of the optical bandgap edge in a non-direct semiconductor, the m value induced by the direct semiconductor

model has been commonly used. [32] The blue shifts of the bandgap caused by Li doping can be explained as the Burstein-Moss effect. According to the Burstein-Moss effects, since the doubly occupied state is restricted by the Pauli principle and the optical transition would be vertical, extra energy should be required to enable the valence electrons to be excited to higher states in the conduction band, which causes the widening of the optical bandgap. [20, 30, 33] Figure 3.7 (d) shows that the optical bandgap is widened upon the initial Li doping (2 mol%) and then narrowed at the high concentration (11 mol%). Interestingly, while 11 mol% Li-doped ZTO TFTs have shown degenerated field effect mobility compared with intrinsic ZTO TFTs, the optical bandgap of intrinsic ZTO films is still wider than that of 11 mol% Li-doped ZTO films. The wider optical bandgap of 11 mol% Li-doped ZTO films than that of intrinsic ZTO films is supported by the higher carrier concentration of 11 mol% Li-doped ZTO films than that of intrinsic ZTO films. (see Table 3.2) However, the Hall mobility and field effect mobility of 11 mol% Li-doped ZTO TFTs was lower than that of intrinsic ZTO TFTs because the excess of Li doping induced segregation and acted as an impurity and scattering sites in the passing of electrons. [14]

These phenomena indicate that the widening of optical bandgap according to doping is induced from the increment of electron carrier concentration. This relation indicates the possibility that the change of field effect mobility in oxide TFTs can be easily monitored through the observation of the optical bandgap shift by UV-visible

spectroscopy. In order to exclude the optical hinderence of substrate in UV-visible spectroscopy and observe exactly the change of optical bandgap of Li-doped ZTO semiconductor films, I investigated the absorption of UV-visible ray by ellipsometer. (Figure 3.7 (c)) The same blue shifts of optical bandgap in Li-doped ZTO semiconductor films were observed. The Li located at interstitial sites in the ZTO matrix caused the increase in the carrier concentration and the widening of the optical bandgap. The 2 mol% Li-doped ZnO TFTs showed the highest value in terms of carrier concentration; otherwise, in exceeding the optimum Li concentration, both the variation of optical bandgap and the carrier concentration were diminished. (Figure 3.7 (d))

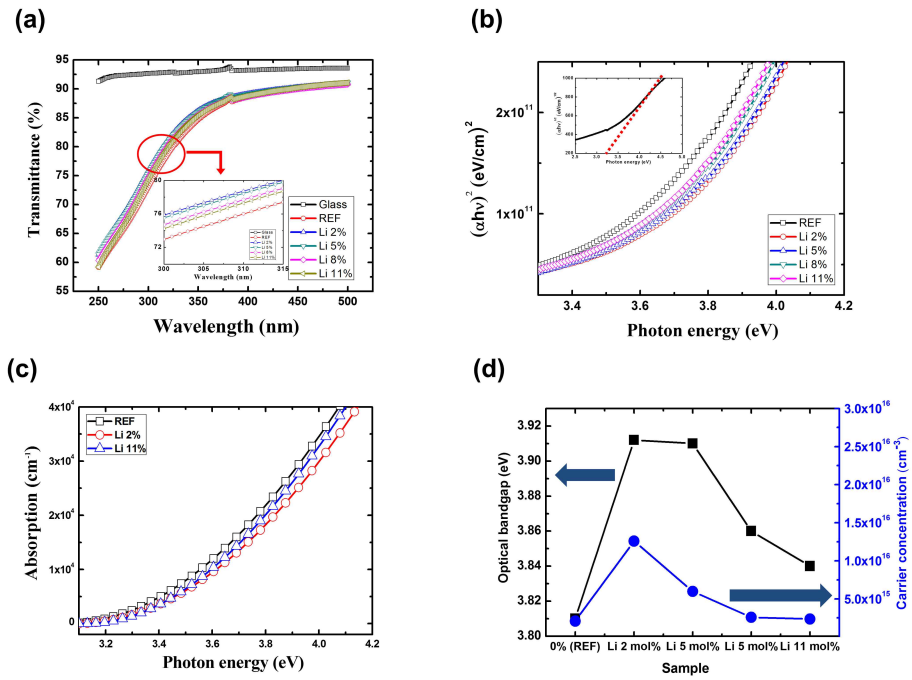

Figure 3.7 (a) The average transmittance of intrinsic ZTO film and alkali metal-doped ZTO films, (b) the $(\alpha hv)^2$ vs. photon energy plot of the intrinsic ZTO film and alkali metal-doped ZTO films (inset: $(\alpha hv)^{1/2}$ vs. photon energy plot of intrinsic ZTO film), (c) absorption vs. photon energy plot of intrinsic ZTO film and Li-doped ZTO films through ellipsometry, (d) the variation of optical bandgap and carrier concentration of Li-doped ZTO films according to Li concentrations.

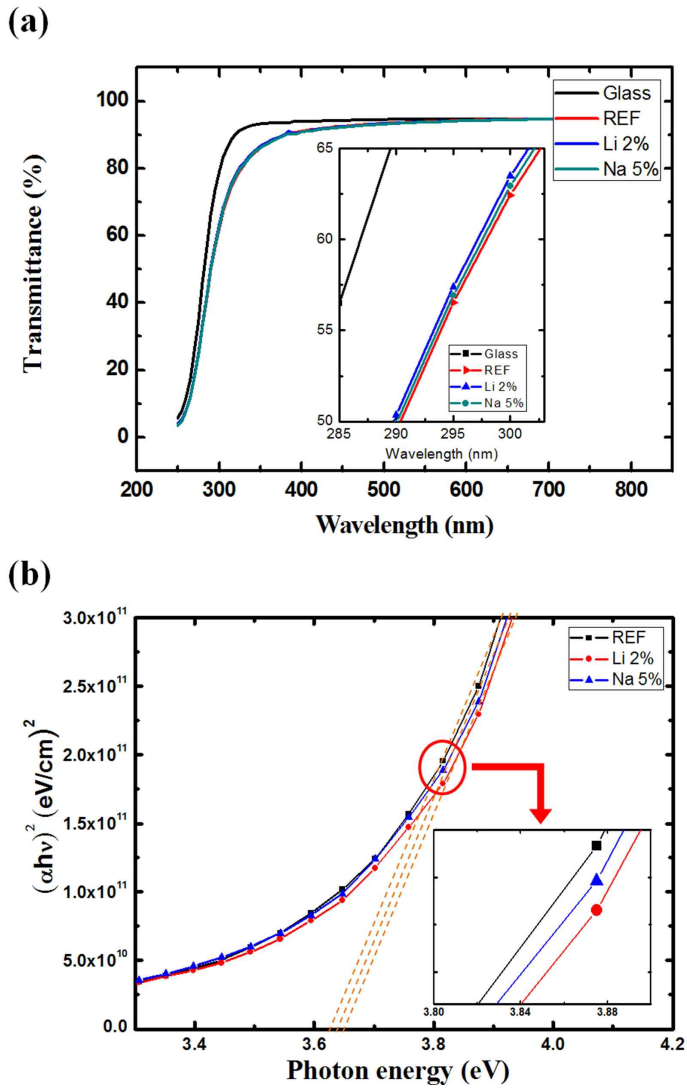

Figure 3.8 (a) The transmittance of the intrinsic ZTO film and alkali metals, Li and Na, doped ZTO films in the slicate glass. (b) the $(\alpha h\nu)^2$ vs photon energy plot of the intrinsic ZTO film and alkali metals, Li and Na, doped ZTO films in the silicate glass.

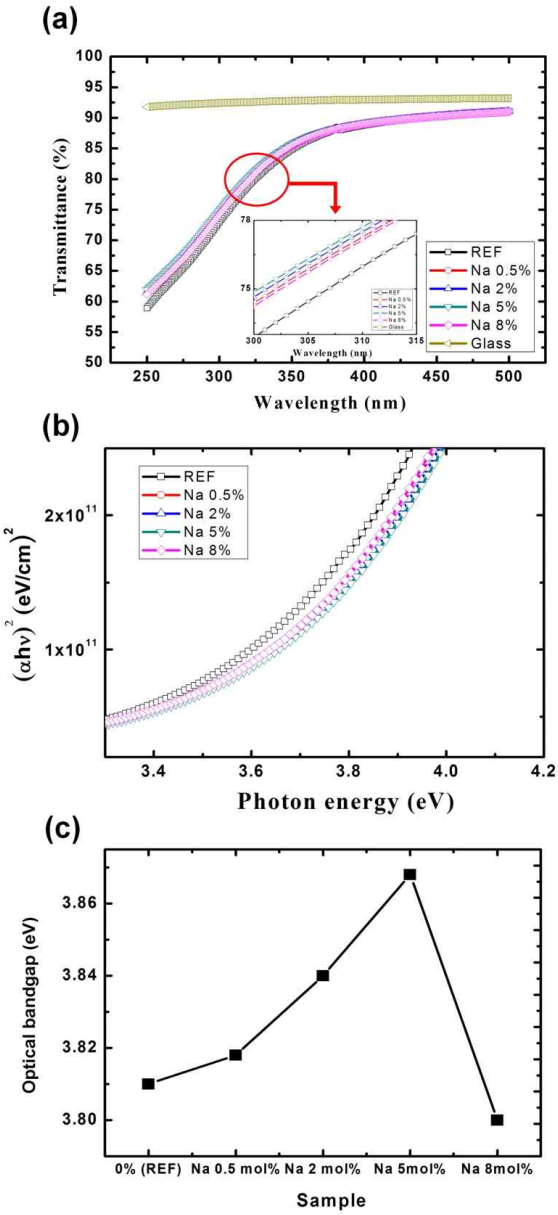

Figure 3.9 (a) Transmittance of intrinsic ZTO film and Na-doped ZTO films, (b) the $(\alpha h\nu)^2$ vs. photon energy plot of the intrinsic ZTO film and alkali Na-doped ZTO films, (c) optical bandgap and carrier concentration of intrinsic ZTO and Na-doped ZTO TFTs.

3.6 Experimental details

Fabrication of alkali metal doped ZTO TFT

A zinc tin oxide (ZTO) solution was prepared using 0.15M zinc acetate ($Zn(CH_3COO)_2$) [Sigma Aldrich, 99.99%] and 0.225 M tin chloride ($SnCl_2$) [Sigma Aldrich, 99.99%] dissolved in 2-methoxyethanol (Zn^{2+}:Sn^{2+}=4:6) under ambient condition. Additionally, 0.15 M ethanolamine [Sigma Aldrich, 99.5%] was added to the ZTO solution to make a stable solution and then stirred for 6 hours at atmosphere. To make the doped ZTO semiconductors, lithium acetate ($Li(CH_3COO)$) [Sigma Aldrich 99.95%] and sodium acetate ($Na(CH_3COO)$) [Sigma Aldrich 99%] in methanol were each added to a ZTO solution with a Li^+/Zn^{2+} ratio of 0.02 (2 mol wt%), 0.05 (5 mol wt %), 0.08 (8 mol wt %), 0.11 (11 mol wt %) and a Na+/Zn2+ ratio of 0.005 (0.5 mol wt %), 0.01 (1 mol wt %), 0.02 (2 mol wt %), 0.05 (5 mol wt %), and 0.08 (8 mol wt %), respectively. Alkali metal doped ZTO films were spin coated at 5000 rpm and then kept at 500°C for 1 hour during sintering. Al electrodes were thermally evaporated to 100 nm thickness with a 1000 μm width and 50 μm length. Thermally grown 200 nm SiO_2 on highly B-doped Si substrate was used as a dielectric layer and gate electrode (See Figure 3.10).

Characterization and measurements

The I-V characteristics were measured by semiconductor parameter analyzer (Agilent 4155B) under ambient condition. The thickness and

morphology of the films were characterized by an ellipsometer (V-VASE, Wollam. Inc.), SEM (FESEM; S-4800: Hitachi) and AFM (AFM; XE100: PSIA). The optical absorption analyses by ellipsometer were complied with the Tauc-Lorentz model. The crystal structure was defined using XRD (AXS D8 Advanced, Bruker). In addition, XPS (SIGMA PROBE (ThermoVG, U.K)) was used to characterize the electronic state of the doped ZTO films. It was calibrated by the carbon 1s peak (284.6 eV). The Hall mobility, carrier concentration and conductivity were measured by Hall measurement system (ECOPIA HMS-3000). The optical properties were characterized using a UV-visible spectrometer (Lambda 35, Perkinelmer).

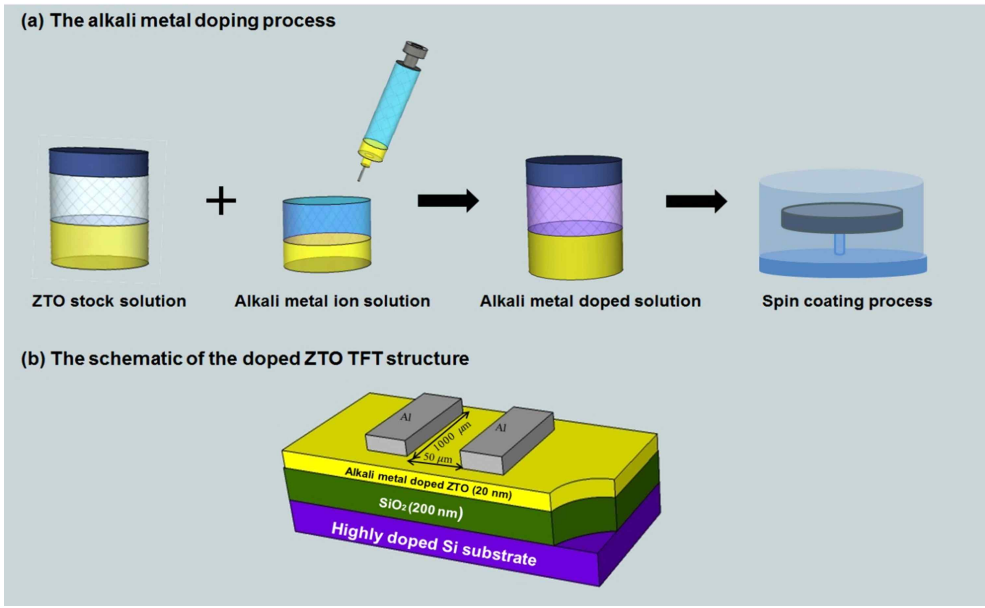

Figure 3.10 (a) Detailed fabrication process for the alkali metal doped zinc tin oxide (ZTO) thin film and (b) The schematic of the alkali metal doped ZTO thin-film transistor.

3.7 References

[1] J. Kim, S. H. Lim, Y. S. Kim, J. Am. Chem. Soc. 2010, 132, 14721.

[2] K. Kim, S. Park, J. B. Seon, K. H. Lim, K. Char, K. Shin, Y. S. Kim, Adv. Funct. Mater. 2011, 21, 3546.

[3] T. Kamiya, H. Hosono, Npg Asia Mater. 2010, 2, 15.

[4] K. Nomura, H. Ohta, K. Ueda, T. Kamiya, M. Hirano, H. Hosono, Science 2003, 300, 1269.

[5] E. Fortunato, P. Barquinha, A. Pimentel, L. Pereira, G. Goncalves, R. Martins, Phys. Status. Solidi-R 2007, 1, R34.

[6] S. J. Lim, S. J. Kwon, H. Kim, J. S. Park, Appl. Phys. Lett. 2007, 91,183517.

[7] S. Y. Park, B. J. Kim, K. Kim, M. S. Kang, K. H. Lim, T. Il Lee, J. M. Myoung, H. K. Baik, J. H. Cho, Y. S. Kim, Adv. Mater. 2012, 24, 834.

[8] C. Avis, Y. G. Kim, J. Jang, J. Mater. Chem. 2012, 22, 17415.

[9] D. H. Lee, Y. J. Chang, G. S. Herman, C. H. Chang, Adv. Mater. 2007, 19, 843.

[10] M. G. Kim, M. G. Kanatzidis, A. Facchetti, T. J. Marks, Nat. Mater. 2011, 10, 382.

[11] S. Y. Han, G. S. Herman, C. H. Chang, J. Am. Chem. Soc. 2011, 133, 5166.

[12] K. K. Banger, Y. Yamashita, K. Mori, R. L. Peterson, T. Leedham, J. Rickard, H. Sirringhaus, Nat. Mater. 2011, 10, 45.

[13] K. Park, D. Lee, B. Dim, H. Jeon, N. Lee, D. Whang, ,H. Lee, Y.

J. Kim, J. Ahn, Adv. Funct. Mater. 2010, 20, 3577.

[14] C. Koo, K. Song, Y. Jung, W. Yang, S. Kim, S. Jeong, J. Moon, Acs Appl. Mater. Inter. 2012, 4, 1456.

[15] S. J. Seo, C. G. Choi, Y. H. Hwang, B. S. Bae, J. Phys. D Appl. Phys. 2009, 42, 035106.

[16] H. S. Shin, G. H. Kim, W. H. Jeong, B. Du Ahn, H. J. Kim, Jpn. J. Appl. Phys. 2010, 49, 03CB01.

[17] Y. S. Rim, D. L. Kim, W. H. Jeong, H. J. Kim, Electrochem. Solid St. 2012, 15, H37.

[18] A. Vandooren, S. Cristoloveanu, D. Flandre, J. P. Colinge, Solid State Electron. 2001, 45, 1793.

[19] S. J. Seo, Y. H. Hwang, B. S. Bae, Electrochem. Solid St. 2010, 13, H357.

[20] G. Srinivasan, R. T. R. Kumar, J. Kumar, J. Sol-Gel Sci. Techn. 2007, 43, 171.

[21] P. Ruankham, T. Sagawa, H. Sakaguchi, S. Yoshikawa, J. Mater. Chem. 2011, 21, 9710.

[22] N. L. Dehuff, E. S. Kettenring, D. Hong, H. Q. Chiang, J. F. Wager, R. L. Hoffman, C. H. Park, D. A. Keszler, J. Appl. Phys. 2005, 97, 064505.

[23] K. Nomura, H. Ohta, A. Takagi, T. Kamiya, M. Hirano, H. Hosono, Nature 2004, 432, 488.

[24] T. Kamiya, K. Nomura, H. Hosono, J. Disp. Technol. 2009, 5, 462.

[25] J. R. Duclere, M. Novotny, A. Meaney, R. O'Haire, E. McGlynn,

M. O. Henry, J. P. Mosnier, Superlattice Microst. 2005, 38, 397.

[26] J. B. Yi, C. C. Lim, G. Z. Xing, H. M. Fan, L. H. Van, S. L. Huang, K. S. Yang, X. L. Huang, X. B. Qin, B. Y. Wang, T. Wu, L. Wang, H. T. Zhang, X. Y. Gao, T. Liu, A. T. S. Wee, Y. P. Feng, J. Ding, Phys. Rev. Lett. 2010, 104, 137201.

[27] W. Beyer, R. Fischer, Appl. Phys. Lett. 1977, 31, 850.

[28] S. Narushima, M. Orita, M. Hirano, H. Hosono, Phys. Rev. B. 2002, 66, 035203.

[29] G. Adamopoulos, A. Bashir, S. Thomas, W. P. Gillin, S. Georgakopoulos, M. Shkunov, M. A. Baklar, N. Stingelin, R. C. Maher, L. F. Cohen, D. D. C. Bradley, T. D. Anthopoulos, Adv. Mater. 2010, 22, 4764

[30] J. G. Lu, J. L. Dai, J. B. Zhu, X. P. Song, Z. Q. Sun, J. Wuhan Univ. Technol. 2011, 26, 23.

[31] S. W. Xue, X. T. Zu, W. L. Zhou, H. Deng, X. Xiang, L. Zhang, H. Deng, J. Alloy Compd. 2008, 448, 21.

[32] A. J. Leenheer, J. D. Perkins, M. F. A. M. van Hest, J. J. Berry, R. P. O'Hayre, D. S. Ginley, Phys. Rev. B 2008, 77, 115215.

[33] B. E. Sernelius, K. F. Berggren, Z. C. Jin, I. Hamberg, C. G. Granqvist, Phys Rev B 1988, 37, 10244.

Chapter 4. Dramatic Enhancement of Field-Effect Mobility in Oxide Semiconductor Thin-Film Transistor through Dielectric Engineering

4.1 Overview

Oxide semiconductors TFTs have emerged as promising switching devices for the next generation display such as smart window, mobile display, and transparent electronic wall because they have high electrical performance, optical transparency, mechanical flexibility. [1-7] To date, the silicon-based TFTs are widely used in conventional display, however, the poor transparency of silicon-based TFTs is a crucial drawback because transparency is one of the key issues for future display technology. [6, 7] Also, the oxide semiconductors have great potential for next-generation processing based on various solution precursors, such as ink-jet printing and screen printing. [5, 7, 8] Unlike vacuum-based deposition, it can allow a large-area fabrication and a low-cost manufacturing. [5, 7, 8] Despite many benefits of deposition processes based on various solution precursors, their relatively low field-effective mobility is the biggest obstacle to apply them to next generation display demanding the higher resolution and larger size. [5, 8, 9] Thus, many researchers have tried to improve the field-effect mobility of solution-processed oxide semiconductor TFTs through various methods (e.g., doping methods, confining structures, etc.). [7, 8, 10-13] However, they are still suffered from a low field-effect mobility under 50 $cm^2 V^{-1} s^{-1}$.

Recently, the high performance oxide semiconductor TFTs by application of specific dielectric film such as solution-processed AlO_x and ZrO_x, which showed a high field-effect mobility of more than 50 $cm^2\ V^{-1}\ s^{-1}$, were reported. [14-17] Because many researchers have speculated that the enhanced field-effect mobility of oxide semiconductor TFTs is affected by the high capacitance of gate dielectrics, [18] the development of the high k gate dielectrics has been strongly accomplished. [19, 20] However, the field-effect mobility of oxide semiconductor TFTs is not always increased despite the use of solution-processed high k dielectrics and which is hardly discovered in vacuum-processed high k dielectrics. Then, the fresh speculation is recently reported that other factors, such as the interface, are dominantly related to the abnormal increase of the field-effect mobility of oxide semiconductor TFTs by solution-processed high k dielectrics. [21, 22] However, there has been no systematic approach on the physical and chemical changes of semiconductor region according to solution-processed high-k dielectrics. Also, the main factors which lead to such changes for the optimization of the oxide semiconductor TFT performance have not been investigated until now.

Here, I introduce the dielectric engineering for inducing the dramatic enhancement of effective field-effect mobility of solution-processed oxide semiconductor TFTs. In particular, I focus on the factor which can lead to such change in the specific gate dielectric, Al_2O_3. In this study, it is found that the control of humidity condition during Al_2O_3

dielectric fabrication can realize the solution-processed $Zn_xSn_yO_z$ (ZTO) TFTs with a very high effective field-effect mobility of approximately 462 cm^2 V^{-1} s^{-1} with 10^6 on/off current ratio. For verification of abnormally enhanced effective field-effect mobility, the electrical properties are strictly investigated through various electrical tests. Furthermore, based on the investigation by the TFT models, such as multiple-trapping-and-release (MTR) and variable-range-hopping (VRH) percolation mechanisms, and systematic analyses with the temperature dependence of the devices, HRTEM, energy-dispersive X-ray spectroscopy (EDX), electron energy loss spectroscopy (EELS), XRD, AFM, X-ray reflectivity (XRR), and XPS, I propose a novel electron transport mechanism which can explain the abnormal enhancement of the effective field-effect mobility of ZTO TFTs by the dielectric engineering in fabrication of solution-processed AlO_x.

4.2 Development of HCA dielectric layer for dramatically enhancing a field-effect mobility

For the study regarding the enhancement of field-effect mobility of oxide semiconductor TFTs on solution-processed AlO_x film, finding the variables inducing the abnormal phenomenon is essential because the field-effect mobility of oxide semiconductor TFTs does not always increase by simple application of solution-processed AlO_x dielectric. [23, 24] Considering that the solution-process is affected by humidity condition and the surface of Al_2O_3 films easily reacts with water, [25] I focus on dielectric engineering by controlling the relative humidity during the heating process in Al_2O_3 dielectric fabrication. Thus, Al_2O_3 films were fabricated in various relative humidity conditions, 0%, 10%, 20%, 40%, and 60% at 25 ºC, during the annealing process of the Al_2O_3 film fabrication. The humidity-controlled Al_2O_3 (HCA) films show a constant capacitance with a 141 nF cm^{-2} from low frequency to high frequency in both atmospheric and vacuum measurement environment (with Agilent 4284A) (Figure 4.1 and 4.2). In different capacitance measurement condition (with Bio-Logic SP-150, Figure 4.1 (c)), the capacitance show similar values. Also, in low frequency condition (< 5 Hz), the dramatic change in capacitance is not found, which means that the ion effect in the HCA is not large. For a channel layer for TFTs, a ZTO film was deposited on HCA and SiO_2 as a reference. The details are described in Experimental details section.

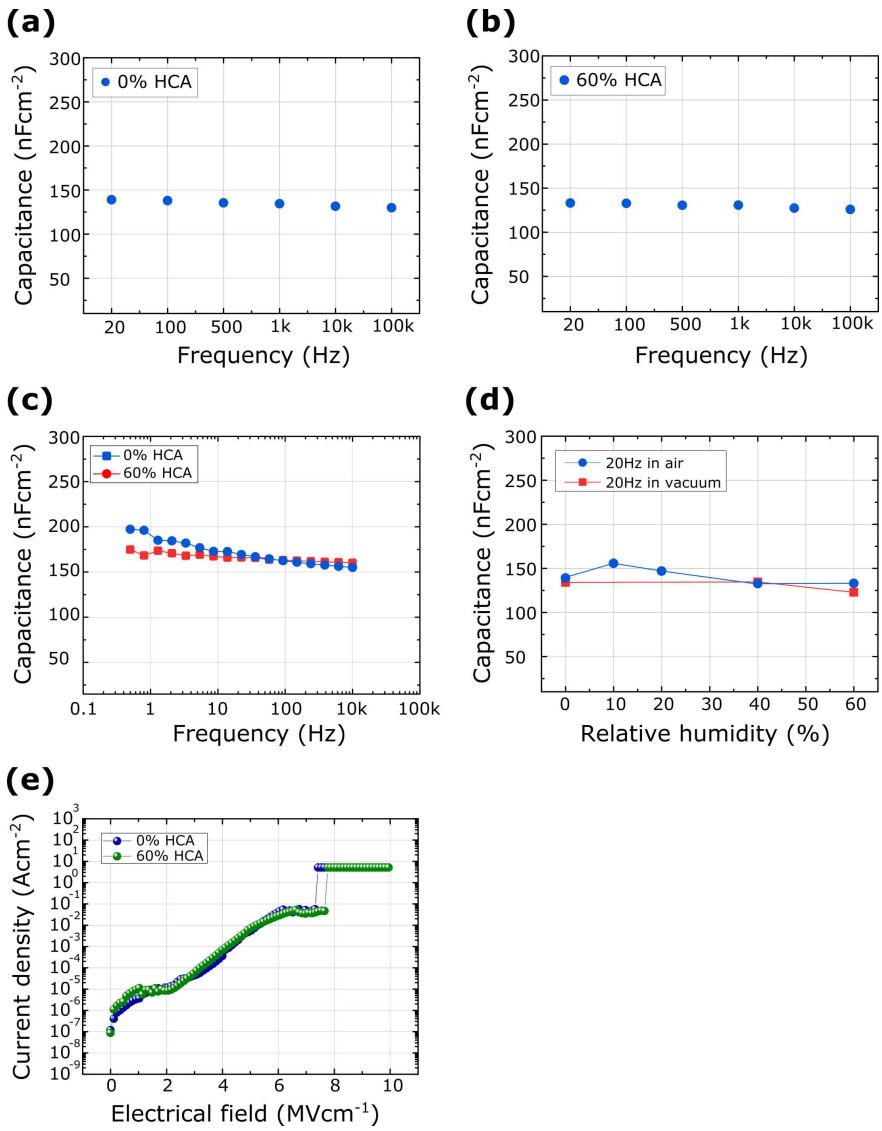

Figure 4.1 The capacitance of HCA dielectrics. The capacitance of (a) 0% HCA and (b) 60% HCA dielectrics measured from 20 Hz to 100 kHz. (c) the capacitance of HCA in low frequency measurement condition. (It is measured by Bio-Logic SP-150. (d) the capacitance of HCA dielectrics in air condition and vacuum condition at 20 Hz. (e) the leakage current and breakdown voltage of HCA dielectrics.

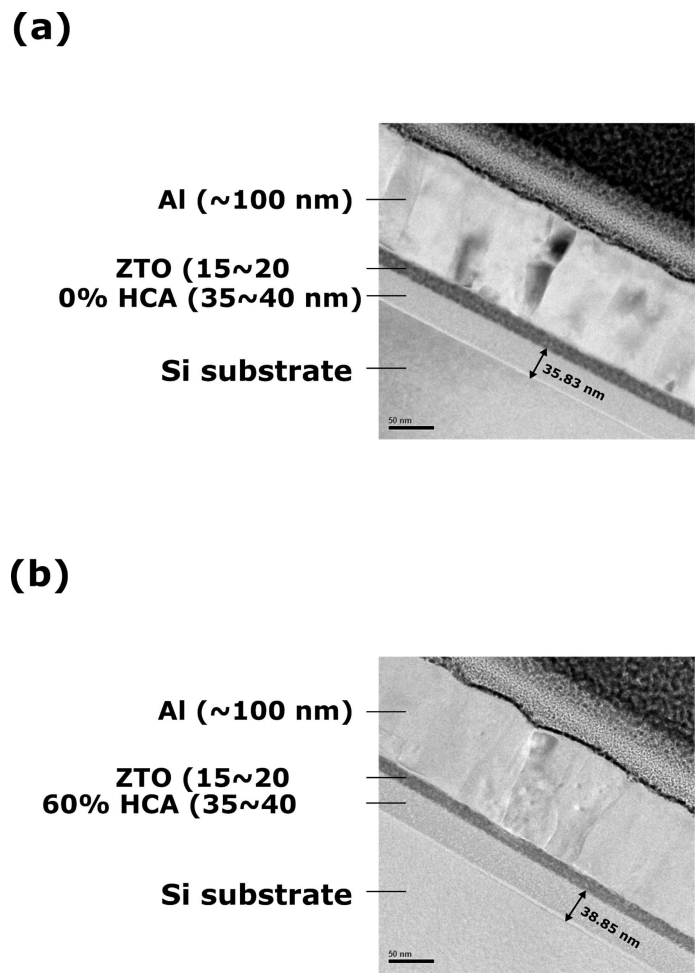

Figure 4.2 Thickness of each layer in ZTO TFT on HCA. Cross-sectional HRTEM images of ZTO TFTs on (a) 0% HCA and (b) 60% HCA.

4.3 Electrical characterization of ZTO TFTs on HCA

Figure 4.3 (a) shows the transfer characteristics of the ZTO TFTs on the SiO_2 film with a channel width and length of 1000 μm and 50 μm. Like conventional ZTO TFTs on SiO_2, [7] at the drain-source voltage (V_{ds}) of 100 V, the fabricated ZTO TFTs on SiO_2 shows a maximum saturation field-effect mobility of 5.87 cm^2 V^{-1} s^{-1} with an on/off current ratio of 10^7. Figure 4.3 (b) and (c) show the transfer curves of the ZTO TFTs on 0% HCA and 60% HCA at V_{ds} = 5 V, respectively. Like the ZTO TFTs on the SiO_2, the ZTO TFTs on 0% HCA have a similar maximum field-effect mobility of 2.55 cm^2 V^{-1} s^{-1} in the linear region. Surprisingly, the ZTO TFT on 60% HCA shows the maximum effective field-effect mobility of 442 cm^2 V^{-1} s^{-1} with an on/off current ratio of 10^6 in the linear region. The improved electrical properties have an apparent tendency related to the humidity conditions. A systematic increase in the average effective field-effect mobility was observed for the case of the ZTO TFTs on HCAs up to a 40% humidity condition (Figure 4.3 (d), 4.4, 4.5, and Table 4.1).

Typically, the field-effect mobility of conventional TFTs with localized states by grain boundary and disordered geometry, such as organic TFTs and oxide semiconductor TFTs, is enhanced by increase of V_{gs}. [9, 18] Accordingly, the field-effect mobility of TFTs derived in whole V_{gs} range is indicated. Interestingly, when the field-effect mobility of these devices is calculated by the equation of conventional TFT theory, the enhancement of field-effect mobility is

divided into two parts: gradual enhancement region (V_{gs} < 6 V) and dramatic enhancement region (V_{gs} > 6 V). In the gradual enhancement region, the field-effect mobility is gradually increased until about 50 cm^2 V^{-1} s^{-1} like the behavior of general oxide semiconductor TFTs having localized states. (Figure 4.6) In the dramatic enhancement region, the field-effect mobility is more dramatically increased. Considering threshold voltage at low V_{gs} and electrical current level at 10 V_{gs} of the ZTO TFT on 60% HCA, it shows similar electrical performance to ideal field-effect transistor having a field-effect mobility of about 180 cm^2 V^{-1} s^{-1}. (Figure 4.7) Meanwhile, due to the abnormal behavior of these devices, the wording 'effective field-effect mobility' is used instead of 'field-effect mobility', which is concretely described in discussion part. Also, various electrical analyses for verification of device performance such as different measuring condition, switching stability and hysteresis tests are tested. (See the Figure 4.8 and 4.9) Typically, the fringe current increases the drain current, whereas, the gate-drain leakage current can reduce the drain current in the linear region. (Figure 4.10) In this device, after patterning process, the maximum effective field-effect mobility with a high uniformity is not changed by the patterning process. (Figure 4.11 and 4.12).

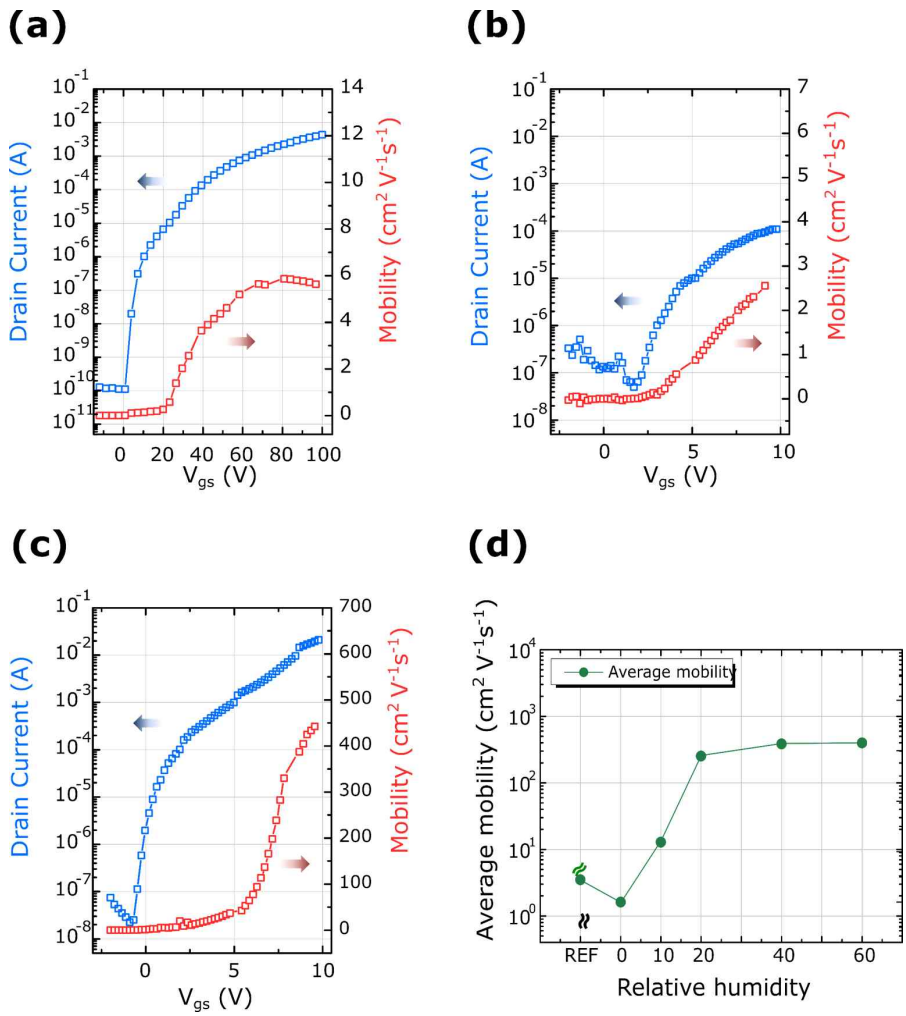

Figure 4.3 Electrical performance of solution-processed ZTO TFTs on SiO_2, HCA and a bilayer dielectric composed of HCA and SiN_x fabricated in different humidity condition. Transfer characteristics of ZTO TFTs on (a) SiO_2, (b) 0% HCA and (c) 60% HCA. (d) systematic transition of maximum linear field-effect mobility according to humidity conditions during the fabrication of AlO_x dielectric films.

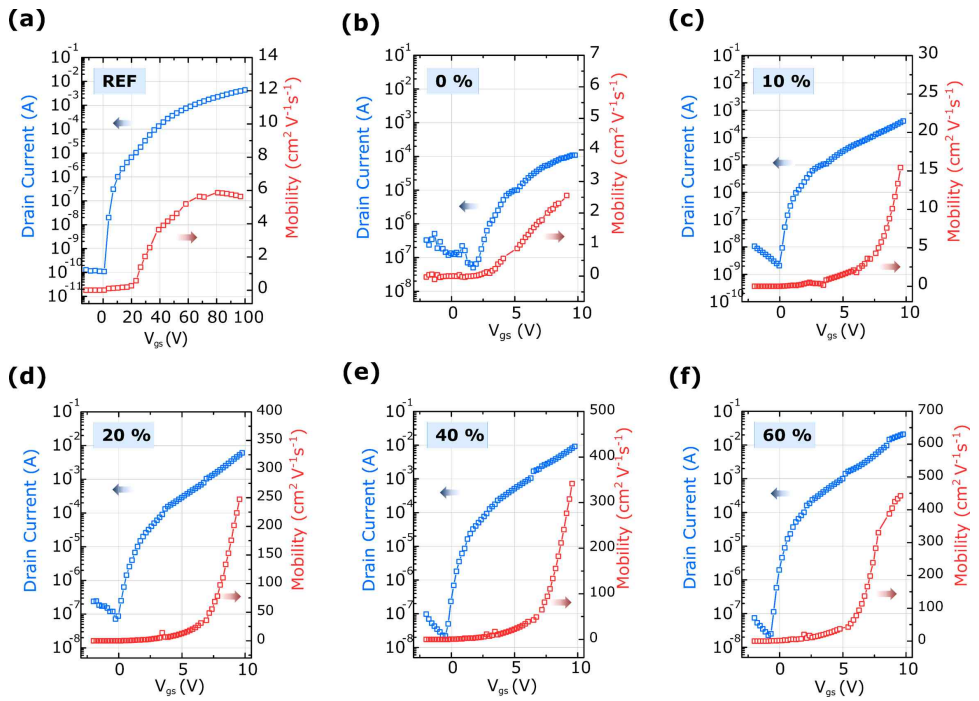

Figure 4.4 Transfer characteristics of ZTO TFTs. (a) ZTO TFT on SiO_2. (b) ZTO TFT on 0% HCA. (c) ZTO TFT on 10% HCA. (d) ZTO TFT on 20% HCA. (e) ZTO TFT on 40% HCA. (f) ZTO TFT on 60% HCA. The transfer curves and field-effect mobility curves inform the change of operating current and mobility change of ZTO TFTs according to humidity control during AlO_x fabrication.

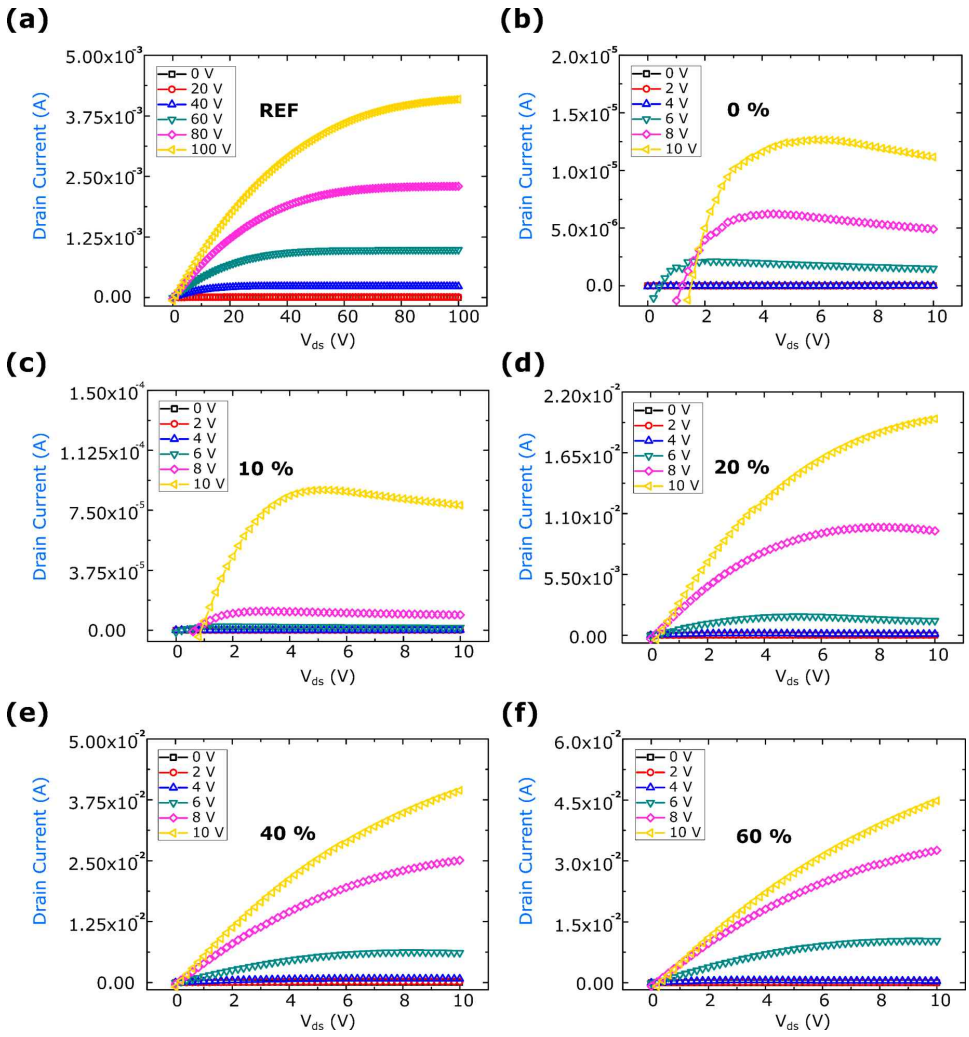

Figure 4.5 Output characteristics of ZTO TFTs. (a) ZTO TFT on SiO_2. (b) ZTO TFT on 0% HCA. (c) ZTO TFT on 10% HCA. (d) ZTO TFT on 20% HCA. (e) ZTO TFT on 40% HCA. (f) ZTO TFT on 60% HCA. The normal output curves inform that ZTO TFTs on HCA work faithfully as a TFT.

	μ_{max} ($cm^2\ V^{-1}\ s^{-1}$)	μ_{avg} ($cm^2\ V^{-1}\ s^{-1}$)	Standard deviation ($cm^2\ V^{-1}\ s^{-1}$)	On/off	V_{on-avg} (V)
ZTO TFTs on SiO_2	5.87	3.48	1.40	10^7	-15
ZTO TFTs on 0% HCA	2.55	1.61	0.86	10^4	1.4
ZTO TFTs on 10% HCA	18.3	12.8	3.98	10^4	0.92
ZTO TFTs on 20% HCA	274	252	16.9	10^5	-0.31
ZTO TFTs on 40% HCA	462	384	71.7	10^6	-0.51
ZTO TFTs on 60% HCA	442	399	38.9	10^6	-0.41
ZTO TFTs on 200 nm SiN_x	10.2	7.89	1.92	10^9	-0.41

Table 4.1 The maximum and average field effect mobility, the standard deviation (S.D.) of field effect mobility, average on/off current ratio, and average operating voltage of 30 ZTO TFTs on HCA and SiN_x fabricated by one-run.

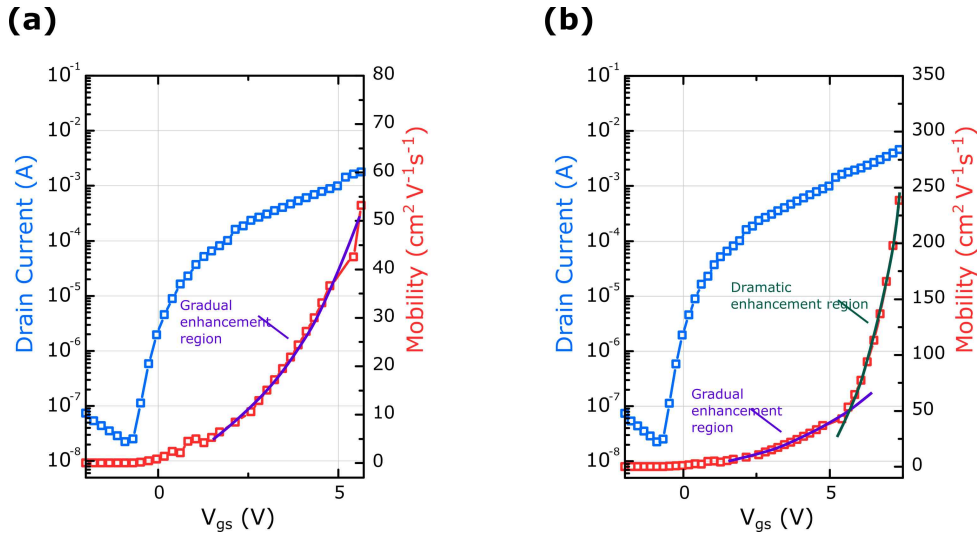

Figure 4.6 The abnormal behavior of field-effect mobility in ZTO TFT on 60% HCA. The transfer characteristics and field-effect mobility at V_{gs} from (a) -2 to 5.7 V and (b) -2 to 7.5 V.

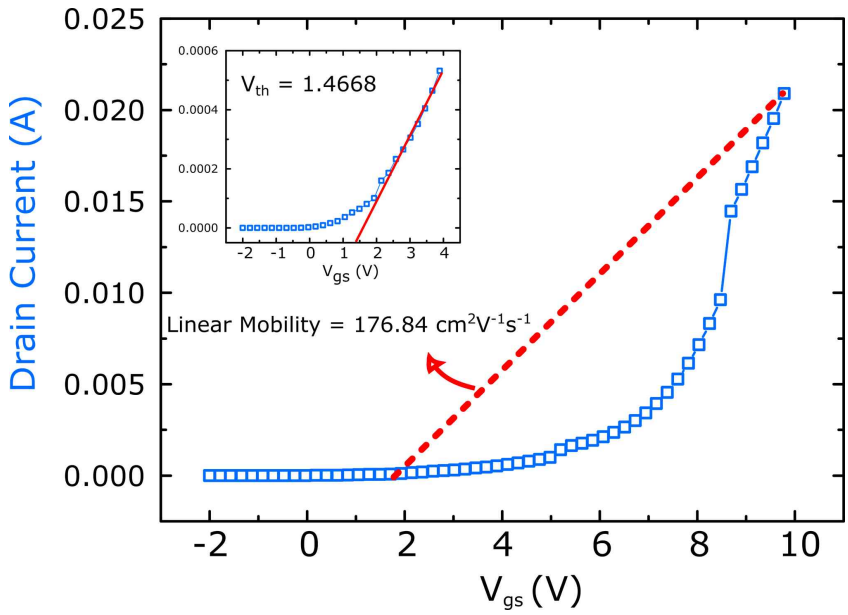

Figure 4.7 The expected field-effect mobility of ZTO TFTs on 60% HCA considering threshold voltage at low V_{gs} and current level at V_{gs} of 10 V to compare with the ideal field-effect transistor.

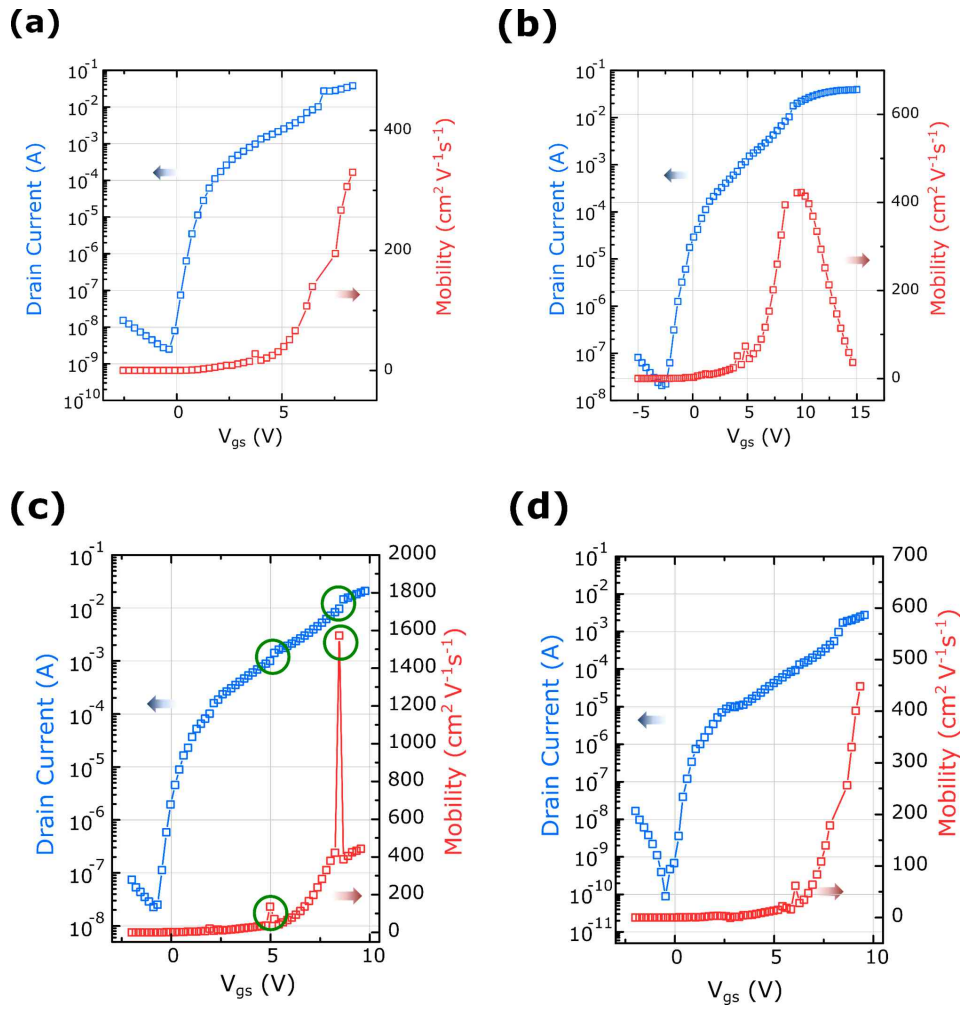

Figure 4.8 (a) transfer characteristics of ZTO TFT on 60% HCA with 1000 μm channel width and 15 μm channel length. (b) transfer characteristics of ZTO TFT on 60% HCA with 1000 μm channel width and 50 μm channel length in 15 V_{gs} sweep mode. (c) the soaring peaks of the field-effect mobility caused by a sudden change in the drain current. (d) the transfer characteristics of ZTO TFTs on 60% HCA operated at V_{ds} = 1 V.

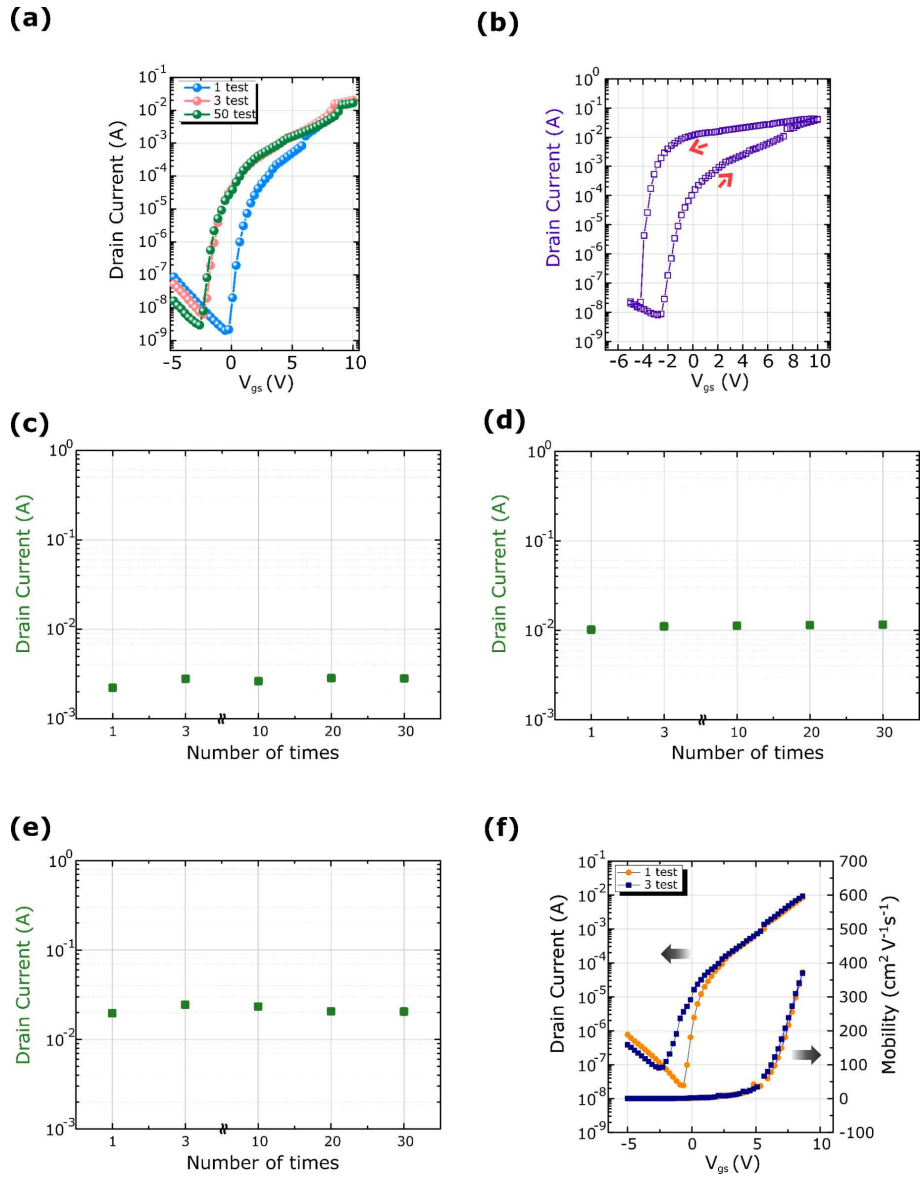

Figure 4.9 (a) The hysterysis of ZTO TFTs on 60% HCA with 1000 μm channel width and 15 μm channel length. The change of drain current and field-effect mobility of ZTO TFTs on 60% HCA by repeat test at constant gate voltage and drain voltage, (b) V_{gs} = 6 V,

V_{ds} = 5 V (c) V_{gs} = 8 V, V_{ds} = 5 V (d) V_{gs}= 10 V, V_{ds} = 5 V. (e) Transfer characteristics and (f) field-effect mobility of ZTO TFTs on 60% HCA with 1000 μm channel width and 50 μm channel length after switching test.

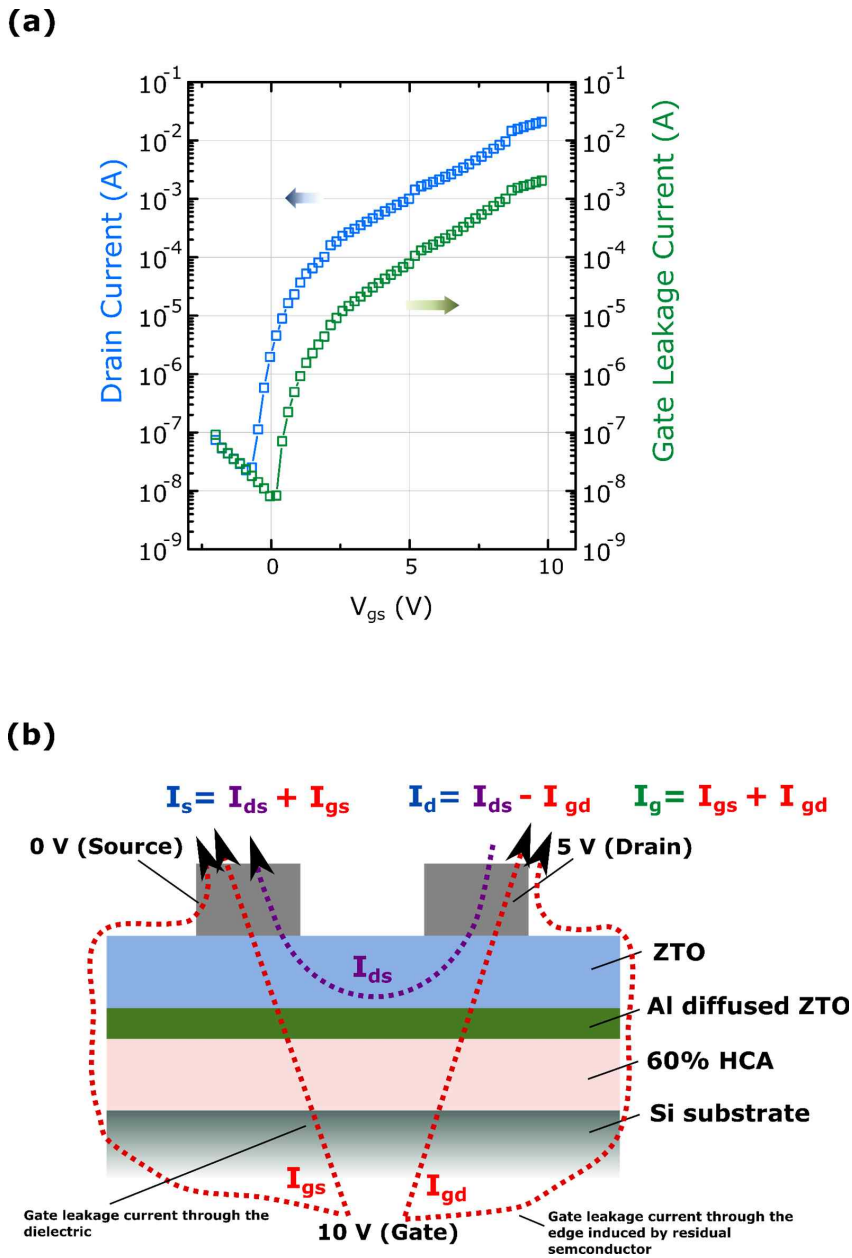

Figure 4.10 (a) The leakage current of ZTO TFTs on 60% HCA with 1000 μm channel width and 15 μm channel length. (b) The schematic of leakage current mechanism in these devices.

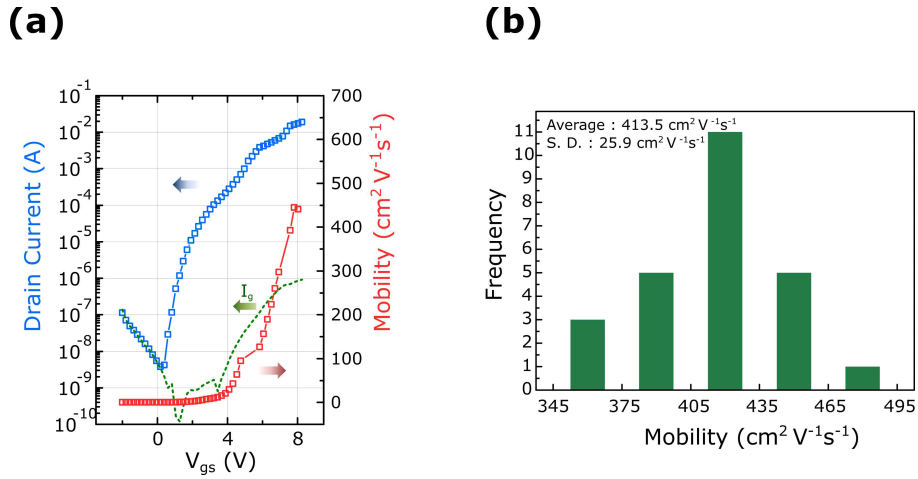

Figure 4.11 (a) transfer characteristics and gate leakage current of patterned ZTO TFTs on a 60% HCA. (b) The histogram of the field-effect mobility of the patterned ZTO TFTs on 60% HCA.

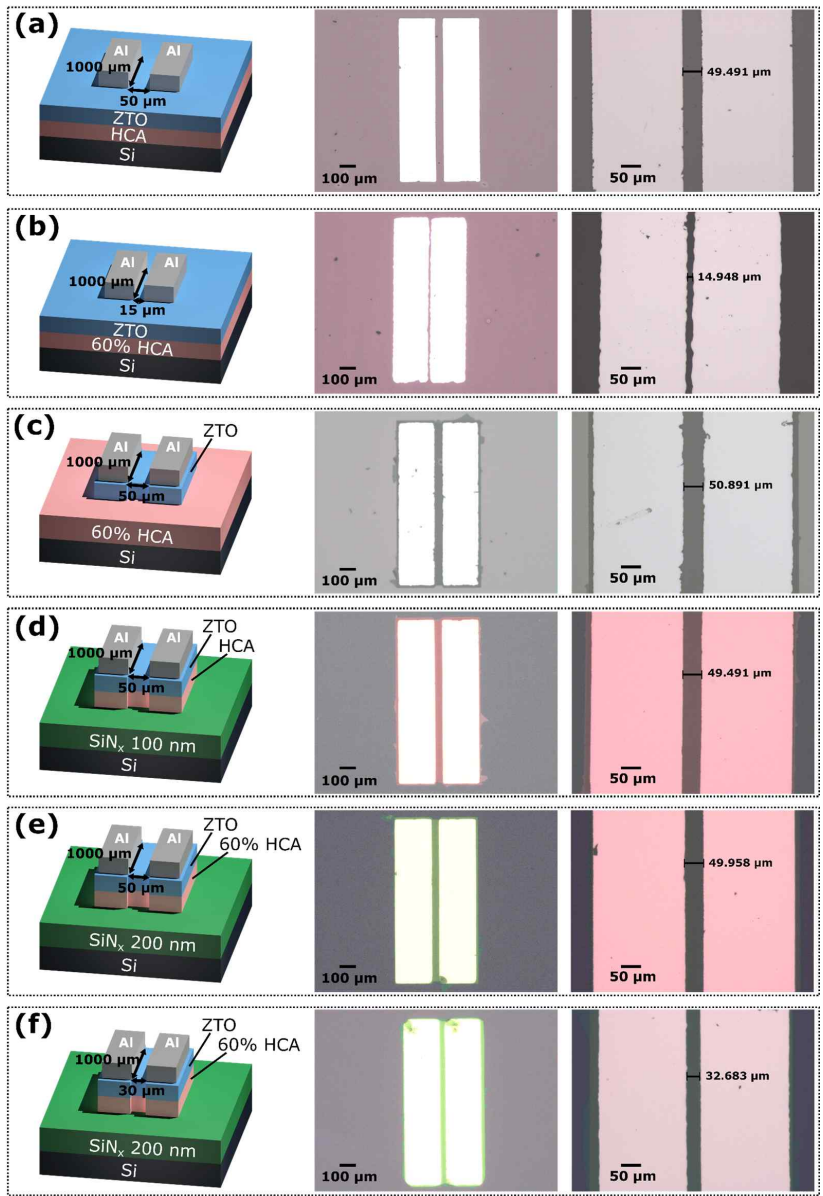

Figure 4.12 (a) ZTO TFT on 60% HCA with 1000 μm channel width and 50 μm channel length. (b) ZTO TFT on 60% HCA with 1000 μm channel width and 15 μm channel length. (c) patterned ZTO TFT on

60% HCA with 1000 μm channel width and 50 μm channel length. (d) patterned ZTO TFT on a bilayer dielectric composed of 60% HCA and 100 nm SiN_x with 1000 μm channel width and 50 μm channel length. (e) patterned ZTO TFT on a bilayer dielectric composed of 60% HCA and 200 nm SiN_x with 1000 μm channel width and 50 μm channel length. (f) patterned ZTO TFT on a bilayer composed of 60% HCA and 200nm SiN_x with 1000 μm channel width and 30 μm channel length.

4.4 Electrical characterization of ZTO TFTs on a bilayer dielectric layer

To confirm the fundamental effects of the dielectric engineering, SiN_x layers with a low capacitance, which is used in conventional display technology, are introduced to the ZTO TFTs on HCA (Figure 4.12). Figure 4.13 show the transfer curves of the patterned ZTO TFTs on a bilayer dielectric composed with HCA, an upper layer, and a SiN_x, bottom layer, with V_{ds} = 20 V. The electrical analyses of these devices are detailed in Supplementary information. (Figure 4.14, 4.15, 4.16, 4.17, 4.18, 4.19 and Table 4.2) The ZTO TFTs on a bilayer dielectric composed with HCA and SiN_x still show a similar electrical tendency depending on the humidity conditions during the annealing process of the Al_2O_3 comparing with the ZTO TFTs on HCA, which means that the HCA layer is fundamental for the enhancement of the effective field-effect mobility. Figure 4.13 shows the transfer characteristics of the patterned ZTO TFTs on a bilayer dielectric composed with 60% HCA and SiNx with an average capacitance of 22.6 nF cm^{-2}. They show the average effective field-effect mobility of 223.6 cm^2 V^{-1} s^{-1} and the standard deviation of 13.1 cm^2 V^{-1} s^{-1}. (Figure 4.16) The effective field-effect mobility of ZTO the TFT on a bilayer dielectric composed with 60% HCA and SiN_x is relatively lower than that of ZTO TFT on a 60% HCA due to change of scattering effect (Figure 4.16). Nevertheless, it is about 20 times greater than that of the reference ZTO TFT on a 200 nm SiN_x. (Figure 4.18)

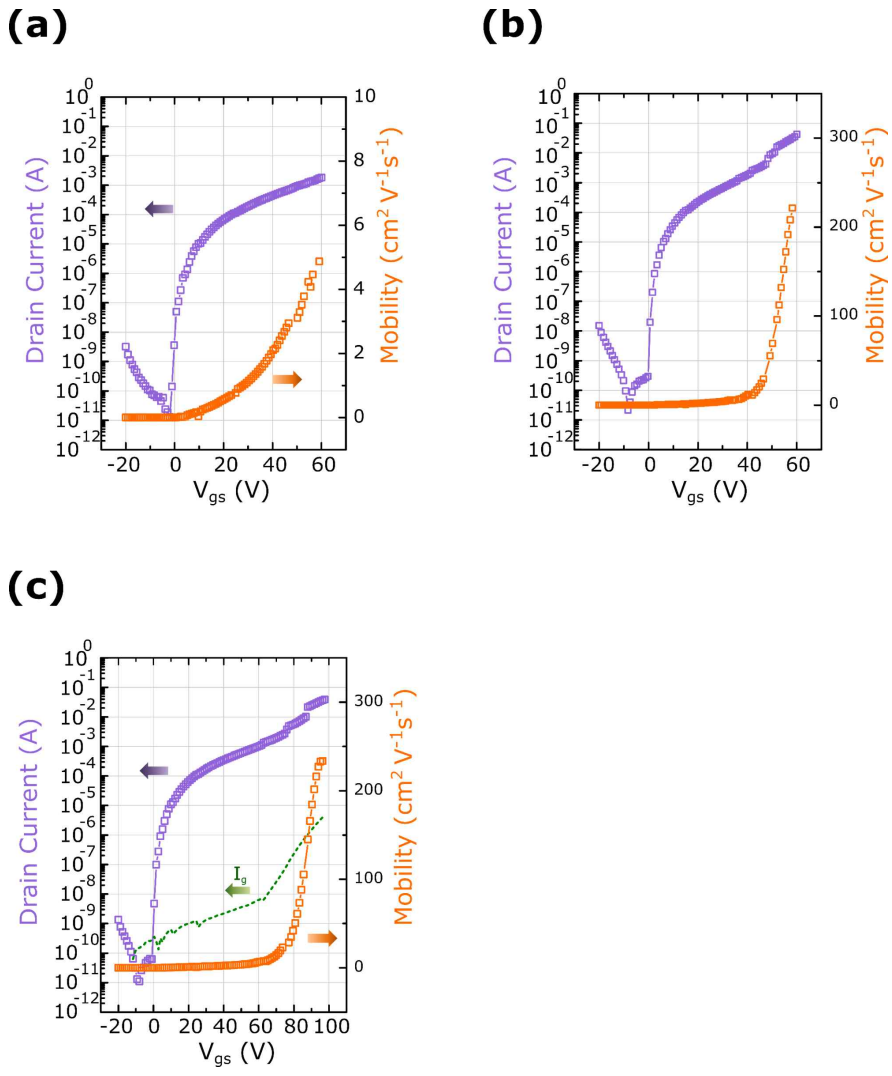

Figure 4.13 Transfer characteristics of patterned ZTO TFTs on a bilayer dielectric composed of (a) 0% HCA and 100 nm SiN_x, and (b) 60% HCA and 100 nm SiN_x. (c) the transfer characteristics and gate leakage current of patterned ZTO TFT on a bilayer dielectric composed of 60% HCA and 200 nm SiN_x. The V_{ds} is fixed at 5 and 20 V in ZTO TFTs on HCA and a bilayer dielectric composed of HCA and SiN_x, respectively.

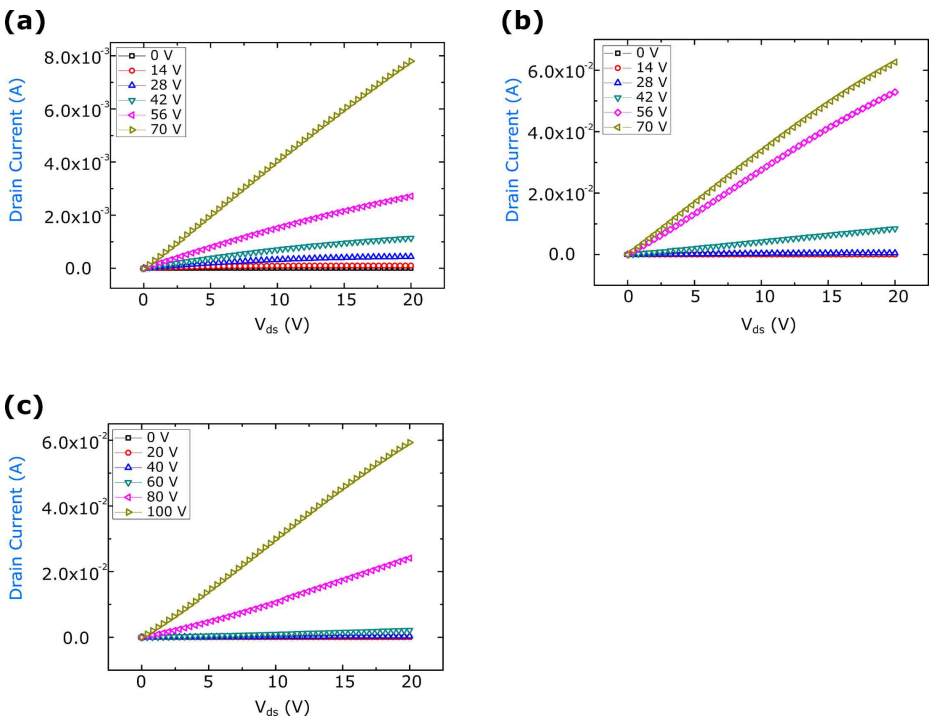

Figure 4.14 (a) 0% HCA and 100 nm SiN_x. (b) 60% HCA and 100 nm SiN_x. (c) 60% HCA and 200 nm SiN_x.

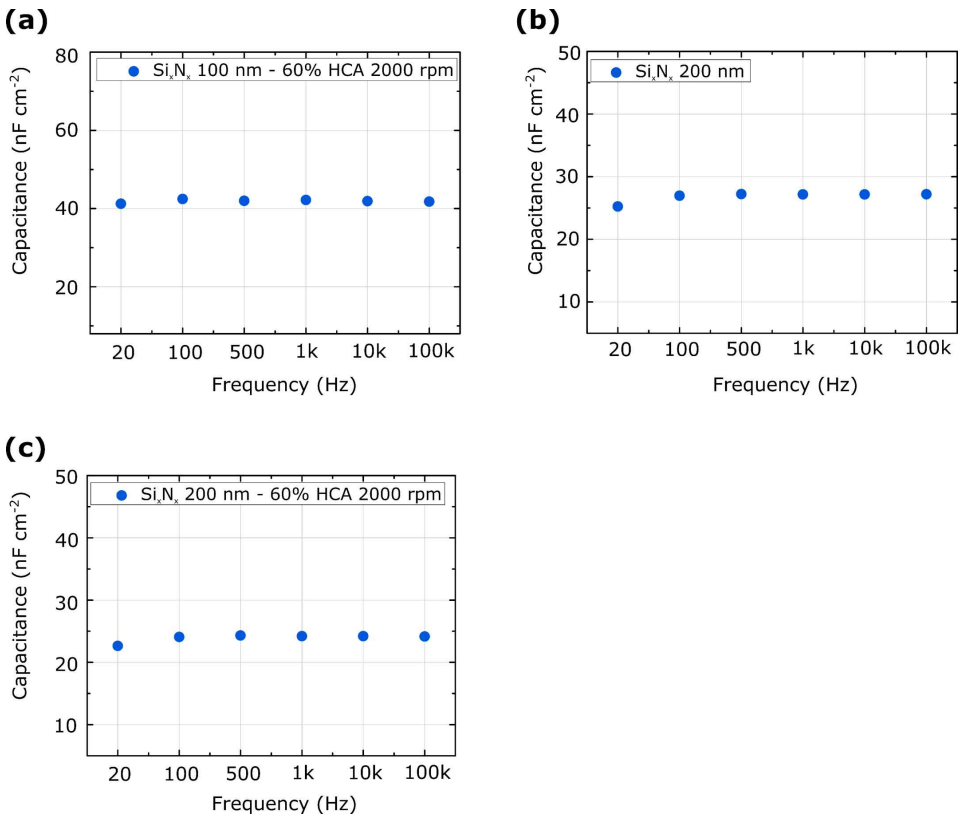

Figure 4.15 (a) A bilayer dielectric composed of 60% HCA and 100 nm SiN_x. (b) 200 nm SiN_x. (c) A bilayer dielectric composed of 60% HCA and 200 nm SiN_x.

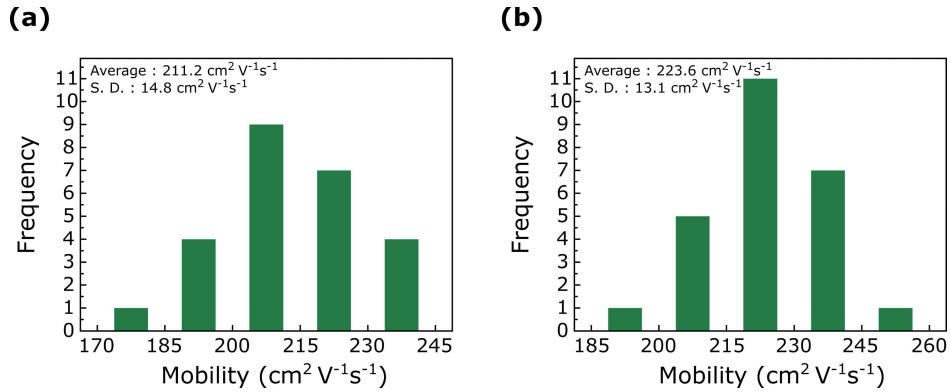

Figure 4.16 The histogram of the field-effect mobility of the patterned ZTO TFTs on a bilayer dielectric composed of 60% HCA and SiN_x. ZTO TFTs on a bilayer composed of (a) 60% HCA and 100 nm SiN_x and (b) 60% HCA and 200 nm SiN_x.

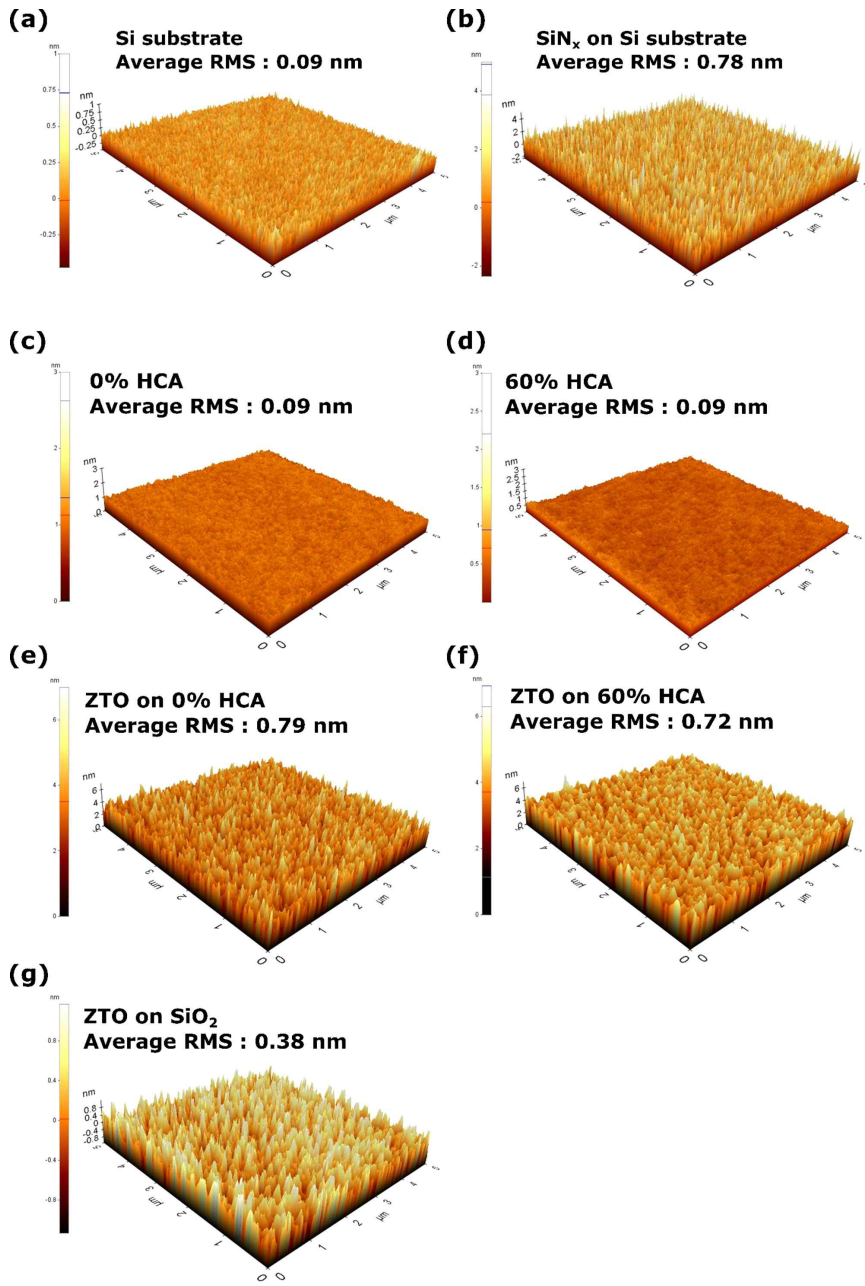

Figure 4.17 The AFM images. (a) Si substrate. (b) SiN_x on Si substrate. (c) 0% HCA. (d) 60% HCA. (e) ZTO on 0% HCA. (f) ZTO on 60% HCA. (g) ZTO on SiO_2.

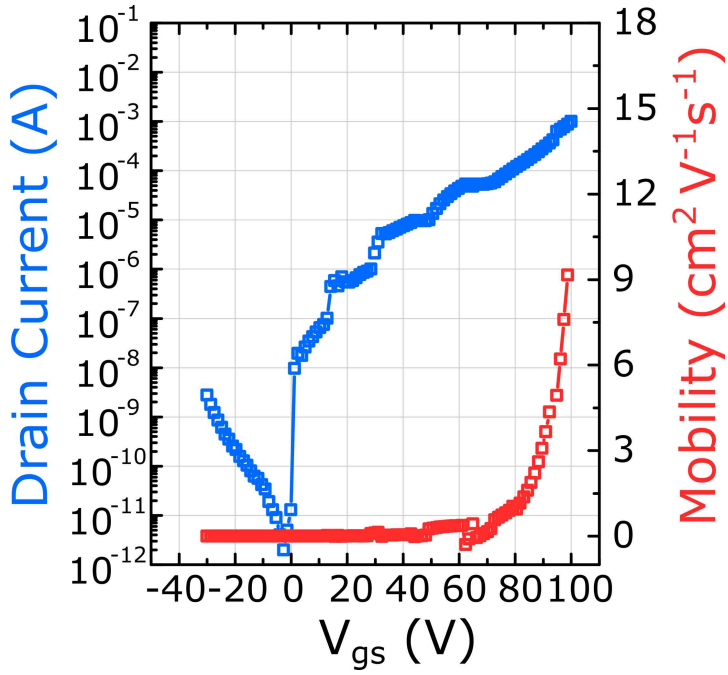

Figure 4.18 Transfer characteristics of the ZTO TFT on 200 nm SiN_x. The average field-effect mobility of ZTO TFT on 200 nm SiN_x with 1000 μm channel width and 50 μm channel length show about 7.89 $cm^2\ V^{-1}\ s^{-1}$.

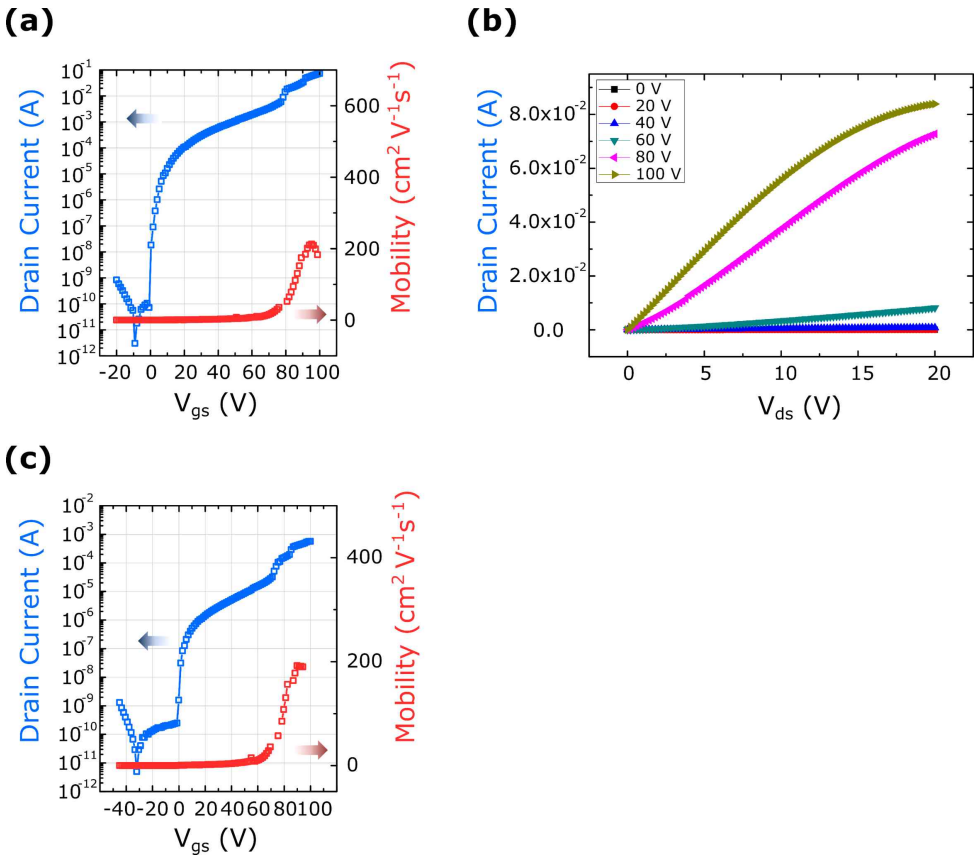

Figure 4.19 Electrical characteristics of patterned ZTO TFTs on 60% HCA and 200 nm SiN_x with 1000 μm channel width and 30 μm channel length. (a) Transfer characteristics operated at V_{ds} = 20 V. (b) Output characteristics. (c) Transfer characteristics operated at V_{ds} = 0.1 V.

	μ_{max} (cm^2 V^{-1} s^{-1})	μ_{avg} (cm^2 V^{-1} s^{-1})	Standard deviation (cm^2 V^{-1} s^{-1})	On/off	V_{on} (V)
Patterned ZTO TFTs on 60% HCA	473.5	413.5	25.9	10^7	0.37
Patterned ZTO TFTs on 0% HCA and 100 nm SiN_x	8.75	7.83	0.78	10^8	-2.0
Patterned ZTO TFTs on 60% HCA and 100 nm SiN_x	235.6	211.4	14.4	10^8	-0.2
Patterned ZTO TFTs on 60% HCA and 200 nm SiN_x	253	223.6	13.1	10^9	-0.85

Table 4.2 The maximum and average field effect mobility, the standard deviation (S.D.) of field effect mobility, average on/off current ratio, and average operating voltage of patterned ZTO TFTs on HCA and a bilayer composed of 60% HCA and SiN_x fabricated by one-run.

4.5 Characterization of abnormal electrical behavior in ZTO TFTs on HCA

Figure 4.20 show the theoretical fit by the developed TFT model based on the VRH percolation model for ZTO TFTs. The VRH percolation model (or MTR model for nano-crystalline) is described as [21, 26]

$$I_D = \frac{W\sigma_0\delta V_T}{L(\gamma-1)}\left(\sqrt{\frac{2\epsilon_0\epsilon_s k_B T_0 \sin(\pi T/T_0)}{q^2 N_t^{tot}\pi T/T_0}}\right)^{\gamma}\left(\frac{C_i}{\epsilon_0\epsilon_s}\right)^{\gamma-1} \times\left[\left(\frac{V_{GS}-V_{FB}-\phi_{sS}}{\gamma V_T}+\frac{\gamma}{\gamma-1}\right)\left(\frac{V_{GS}-V_{FB}-\phi_{sS}}{\gamma V_T}\right)^{\gamma-1} -\left(\frac{V_{GS}-V_{FB}-\phi_{sD}}{\gamma V_T}+\frac{\gamma}{\gamma-1}\right)\left(\frac{V_{GS}-V_{FB}-\phi_{sD}}{\gamma V_T}\right)^{\gamma-1}\right] \quad (10)$$

,where N_t^{tot} is the total number of localized state per unit volume, T is the temperature of devices (298.15 K), T_0 is the characteristic temperature of the localized states indicating the width of the exponential distribution, $\gamma=2T_0/T$, σ_0 is the conductivity factor, k_B is the Boltzmann constant, q is the electron charge, $V_T = k_B T/q$ is the thermal voltage, W and L are the width and length of TFT, ε_0 is the electrical permittivity in a vacuum, ε_s is the relative permittivity of the oxide semiconductors, C_i is the gate-dielectric capacitance per area, V_{fb} is the flat-band voltage, V_{gs} is the gate-source voltage, $\delta = [\pi(T_0/T)^3 N_t^{tot}/B_c(2a)^3](T_0/T)$(or δ =1 for the MTR model), a is the effective overlap parameter, B_c, which is the critical number for percolation onset, is about 2.8 in the three-dimensional amorphous systems, ϕ_{sS} and ϕ_{sD} are the surface potential at the source and drain electrodes, and the approximation is described in the reference. [21,

26]

The fitting results show the change of physical parameters depending on the dielectric engineering. (Table 4.3 and 4.4) Despite the increase of capacitance, the physical parameters of ZTO TFTs on 0% HCA such as T_0, a, σ_0 , and N_t^{tot} related with the orbital overlap and the density of localized states show similar values comparing with them of ZTO TFTs on SiO_2. Otherwise, the ZTO on 60% HCA has the lower T_0, N_t^{tot} and higher a values. Accordingly, when the Fermi level lies at 0.2 eV below the conduction band, the conductivity and mobility of the ZTO on 60% HCA is 50 times greater than those of ZTO on SiO_2 or 0% HCA. More importantly, the obtained physical parameters do not satisfy the electrical behavior of dramatic enhancement region.

To analyze the dramatic enhancement region, the electrical behaviors of the patterned ZTO TFTs on a bilayer dielectric composed with 60% HCA and 200 nm SiN_x, are investigated at various temperatures in vacuum condition. (Figure 4.21 (a)) As the temperature rises, the specific V_{gs} in dramatic enhancement region begins negatively shifts. At analysis of the Arrhenius behavior, the abnormal behavior is prominently featured (Figure 4.21 (b)). At a low V_{gs} of 17.2 V and 36.4 V, the effective field-effect mobility follows the Arrhenius behavior with the activation energy of 0.15 eV and 0.11 eV. However, at a high V_{gs} of 62.8 V, a different Arrhenius behavior with the high activation energy appears for temperatures over 303 K. Evidently, the results indicate that the electron transport path of ZTO film on 60%

HCA is changed in the dramatic enhancement region, which strongly implies the existence of two different localized states for transporting electrons: the general localized state at low energy level like conventional oxide semiconductor and the unusual localized state located in high energy level inducing the dramatic enhancement region.

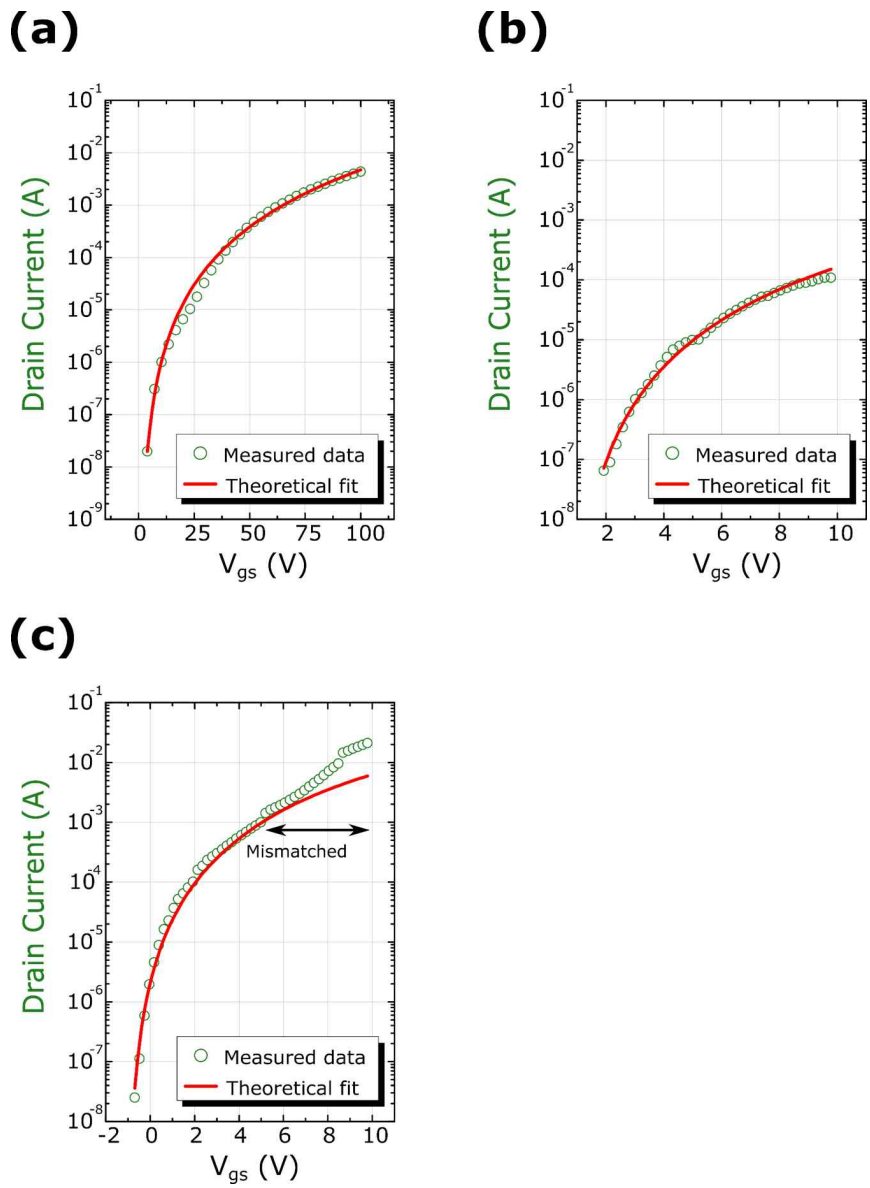

Figure 4.20 Theoretical fits using developed TFT model and the behavior of electrical properties according to temperature change. Theoretical fits to measured transfer characteristics of ZTO TFT on (a) SiO_2, (b) 0% HCA and (c) 60% HCA based on VRH model.

Variables	Information
T_0	Characteristic temperature of the localized state
N_t^{total}	Total number of localized state per unit volume
a	Effective overlap parameter
σ_0	Conductivity prefactor

Table 4.3 The parameter variables and information for theoretical fitting.

	ZTO on SiO_2	ZTO on 0% HCA	ZTO on 60% HCA
T_0 (K)	531.27	528.44	475.01
$N_t^{total}(cm^{-3})$	$1.0*10^{20}$	$1.0*10^{20}$	$3.55*10^{19}$
a (cm^{-1})	$1.2*10^{8}$	$1.3*10^{8}$	$8.8*10^{7}$
σ_0 (S cm^{-1})	$1.4*10^{10}$	$1.3*10^{10}$	$1.5*10^{10}$
σ (S cm^{-1})	0.13	0.09	0.377
μ (cm^2 V^{-1} s^{-1})	0.34	0.25	4.08

Table 4.4 The physical parameters of ZTO on SiO_2 and HCA resulted from theoretical fitting based on MTR model.

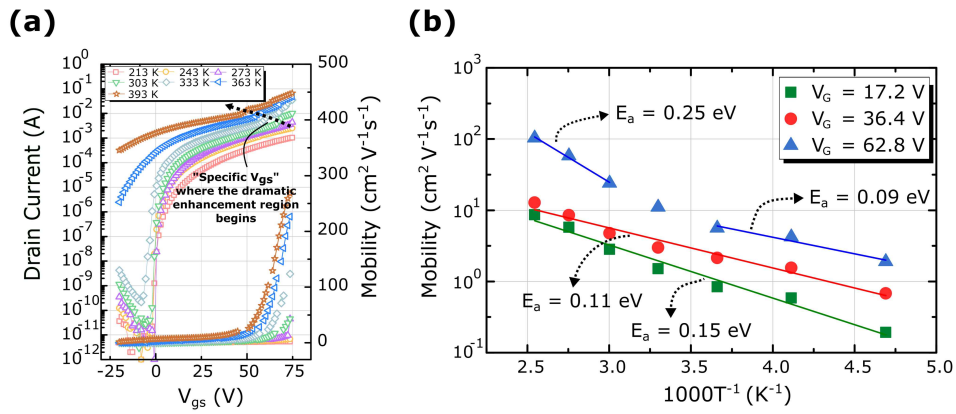

Figure 4.21 (a) The transfer characteristics of ZTO TFT on a bilayer dielectric composed of 60% HCA and 200 nm SiN_x with 1000 μm channel width and 30 μm channel length according to temperature change. (b) The temperature and V_{gs} dependence of field-effect mobility of ZTO TFT on a bilayer dielectric composed of 60% HCA and 200 nm SiN_x. The V_{ds} is fixed at 20 V.

4.6 Analysis of structure and material characterization with ZTO and HCA

To investigate structure and material characterization for the existence of two different localized states according to dielectric engineering, ZTO TFTs on SiO_2 and ZTO TFTs on HCA are analyzed by AFM, HRTEM, in-plain XRD (Figure 4.22 and 4.17). The HCA films had a similar surface roughness regardless of the humidity condition during the annealing process of the Al_2O_3 film fabrication (Figure 4.17 (c) and (d)). In the HRTEM images, while the ZTO films on the SiO_2 film showed an amorphous-like structure (white and yellow squares in Figure 4.22 (a)), the ZTO films on the HCA films showed a nano-crystalline structure at both 0% HCA and 60% HCA (white and yellow squares in Figure 4.22 (b) and (c)). In in-plane mode XRD analysis, the ZTO films on HCA shows a SnO_x nano-crystalline property with (110), (101), (211) peaks (referenced by JCPDS 41-1445) unlike ZTO film on SiO_2 which shows amorphous-like properties (Figure 4.23 (a) and 4.24), which means the segregation of SnO_x nano-crystalline matter from amorphous ZTO film, and the existence of two phases in the ZTO on HCA. The two phases consist of crystalline SnO_x nano-composites and amorphous Zn-based oxide semiconductor in actual channel of ZTO TFT can be considered as a clue which explains an existence of two different localized state. When the SnO_x films and ZnO_x are solely fabricated, the change of crystallinity and electrical properties is not observed according the type of dielectric layer and humidity conditions during

the annealing process of the Al_2O_3 film fabrication (Figure 4.23 (b) and (c)). Meanwhile, SnO_x show the conductor-like electrical properties with similar on-current level in comparison to that of ZTO TFT on 60% HCA at the high V_{gs}. (Figure 4.25 (a)) Interestingly, the electrical performance of SnO_x film is not affected by the type of dielectrics and humidity conditions during the annealing process of the Al_2O_3 film fabrication. (Figure 4.25 (a) and 4.26) Otherwise, although the field-effect mobility and on-current level of ZnO_x TFT on HCA are not as high as that of ZTO TFT on 60% HCA, they are significantly changed by humidity conditions during the annealing process of the Al_2O_3 film fabrication. (Figure 4.25 (a)) When the ZnO_x TFTs on HCA are fitted through the MTR model, the change of physical parameter has similar tendency in comparison with the ZTO TFTs on HCA. (Figure 4.25 (b), (c) and Table 4.5) Strictly, the properties of SnO_x and ZnO_x cannot be the same as the properties of SnO_x and Zn-based oxide semiconductor in ZTO film because the chemical potential and defect formation energy are different in process of the film formation. However, from these investigation, I could deduce the tendency that high electrical performance and the unusual localized states of ZTO TFT on 60% HCA are related to the SnO_x nano-composites, and the general localized states and change of electrical properties of ZTO depending humidity condition in Al_2O_3 film fabrication is related to amorphous Zn-based oxide semiconductor region.

To find out the origin of the change of physical properties of

Zn-based oxide semiconductor region depending on the humidity conditions during the annealing process of the Al_2O_3 film fabrication, the chemical properties at the interface are investigated. The EDX data show that distribution of Al atoms at interface is changed in the 60% HCA (Figure 4.27). To exactly verify the dispersion of Al atoms at the interface, the films were analyzed by EELS. By comparing the Al_2O_3 reference energy loss peak at about 79 and 98 eV, the existence of the Al atoms can be verified (Figure 4.28). Figure 4.28 show the dispersion of the Al atoms near the interface. In ZTO on 0% HCA, the Al atoms are hardly detected in Zn-based region near the interface. (Figure 4.29 (a) and (c)) Otherwise, in the case of ZTO on 60% HCA, Al atoms from 1 nm to 4 nm on the interface are variously distributed. (Figure 4.29 (b) and (d)) To find out the origin of the difference of Al atoms distribution near the interface, XRR, XPS analyses are carried out. In the XRR fitting results, I found that the surface layer and Al_2O_3 layer of 60% HCA have different densities and thicknesses compared with the 0% HCA. (Figure 4.30 (a) and Table 4.6) The average Al_2O_3 density and surface layer density of 0% HCA film are relatively higher than that of the 60% HCA film. In particular, the surface layer density of 60% HCA which is averagely 0.53 g cm^{-3}, has a very small value, which shows that the surface layer of HCA is changed by the humidity conditions during the annealing process of the Al_2O_3 film fabrication. The XPS results show that the surface of 60% HCA includes more aluminium complex with O_2, OH^-, and H_2O (Figure 4.31). It means that the low

density surface mainly consists of dangling bonds and hydroxyl groups. The aluminium complex has a lower decomposition and melting temperature comparing with those of pure Al_2O_3, which increases the possibility of Al dispersion at the interface with chemical reaction during the annealing process.

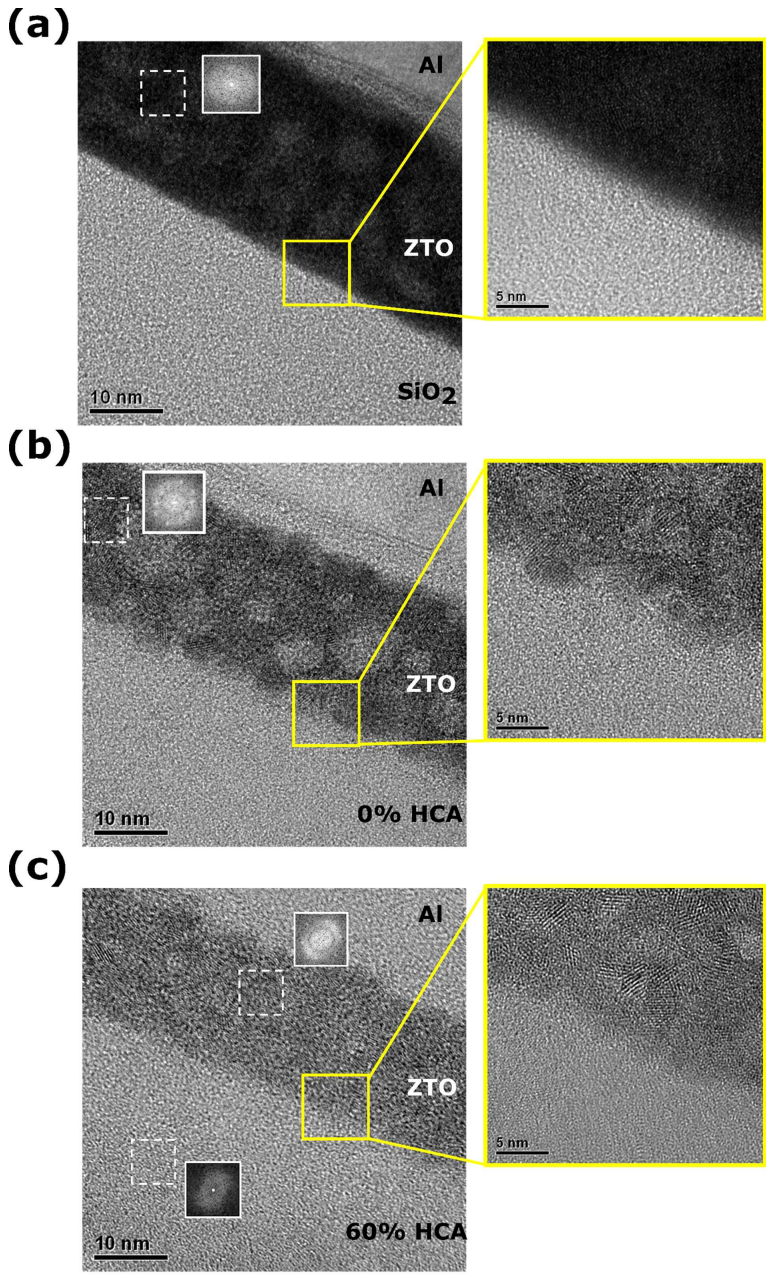

Figure 4.22 Transition of structure and material characterization with ZTO films on SiO_2, HCA fabricated in different humidity condition.

Cross-sectional HRTEM images of ZTO films on (a) SiO_2, (b) 0% HCA, and (c) 60% HCA. The white square in (a), (b) and (c) show the state of ZTO films through the fast Fourier transformation (FFT) pattern. The yellow squares of (a), (b) and (c) show HRTEM images of the enlarged interface through higher magnification (X800,000).

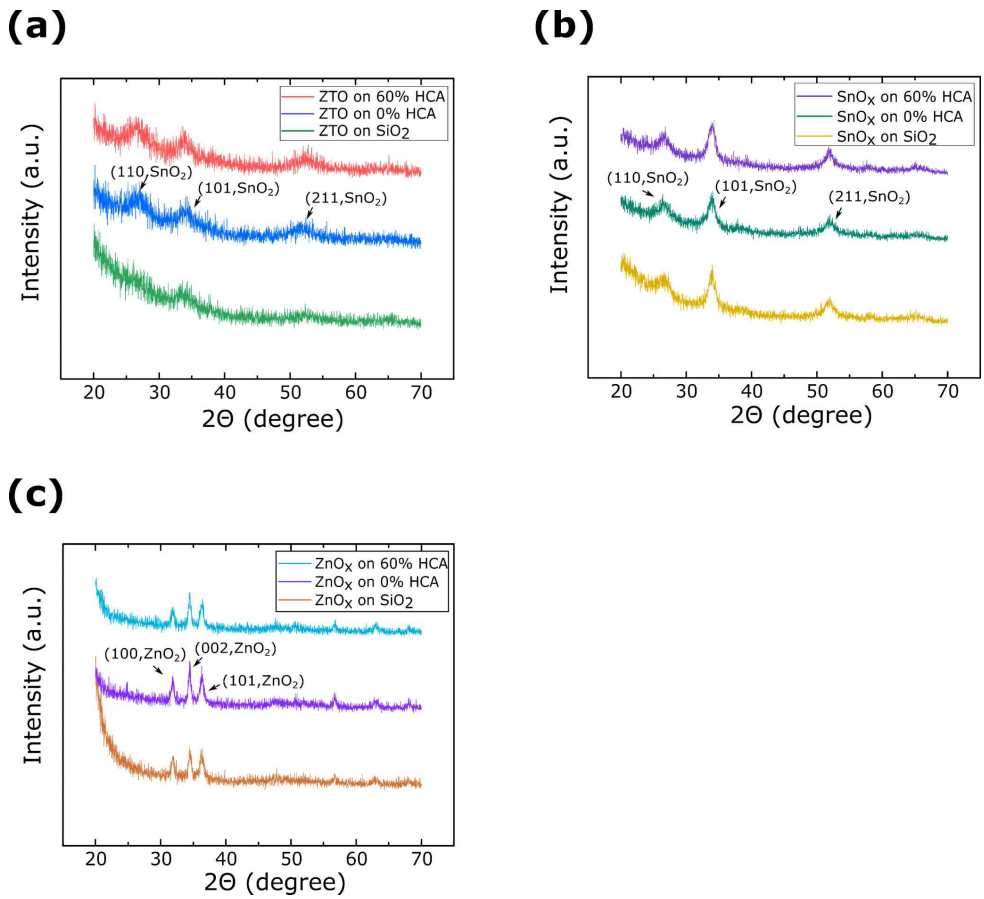

Figure 4.23 The in-plane XRD patterns of (a) ZTO films on HCA film or SiO_2 film, (b) SnO_x films on HCA film or SiO_2 film, and (c) ZnO_x films on HCA film or SiO_2 film

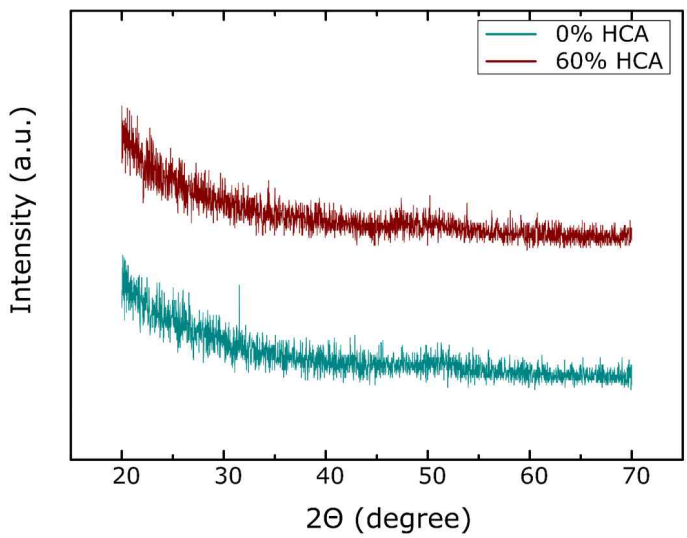

Figure 4.24 The in-plane XRD patterns of HCA films.

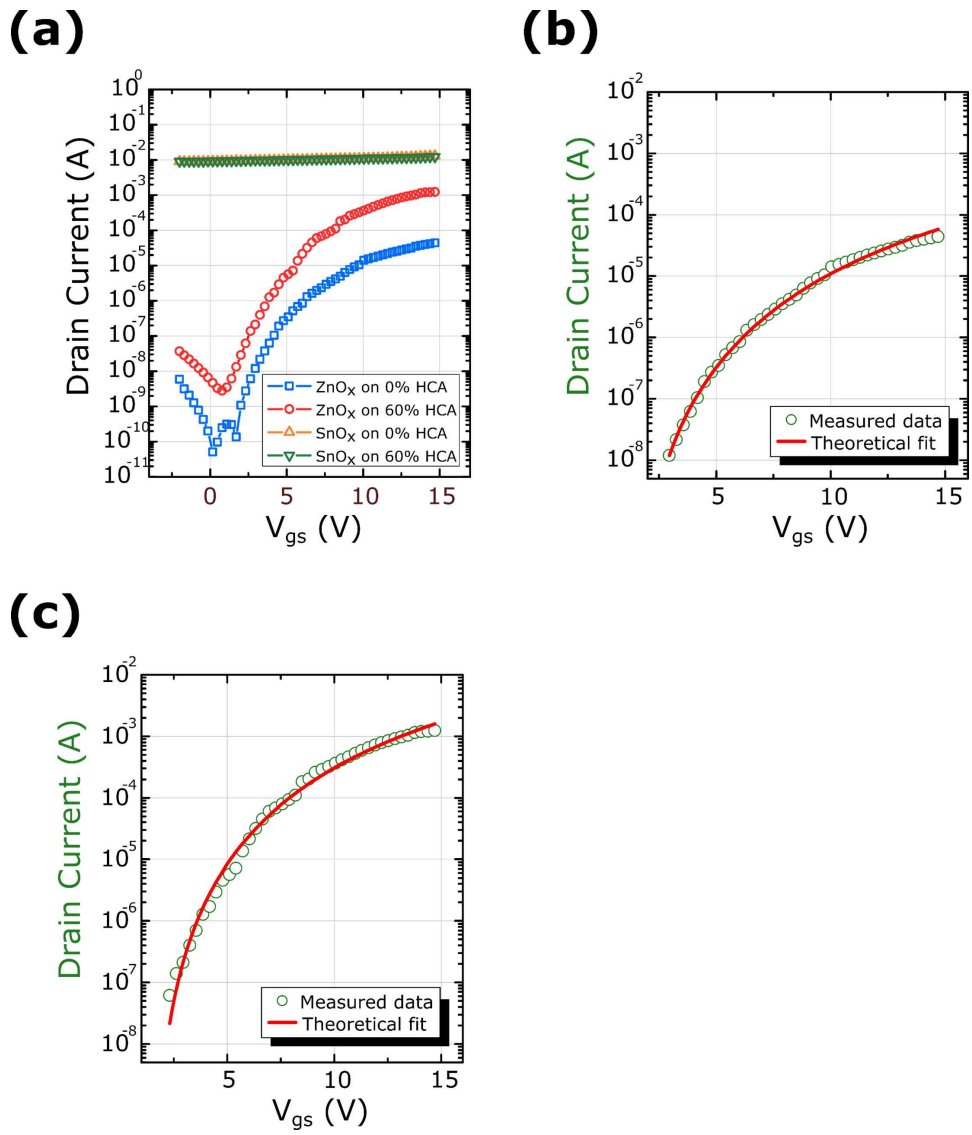

Figure 4.25 (a) Transfer characteristics of ZnO_x TFTs and SnO_x TFTs on HCA films. Theoretical fits to measured transfer characteristics of ZnO_x TFTs on (b) 0% HCA and (c) 0% HCA based on MTR model.

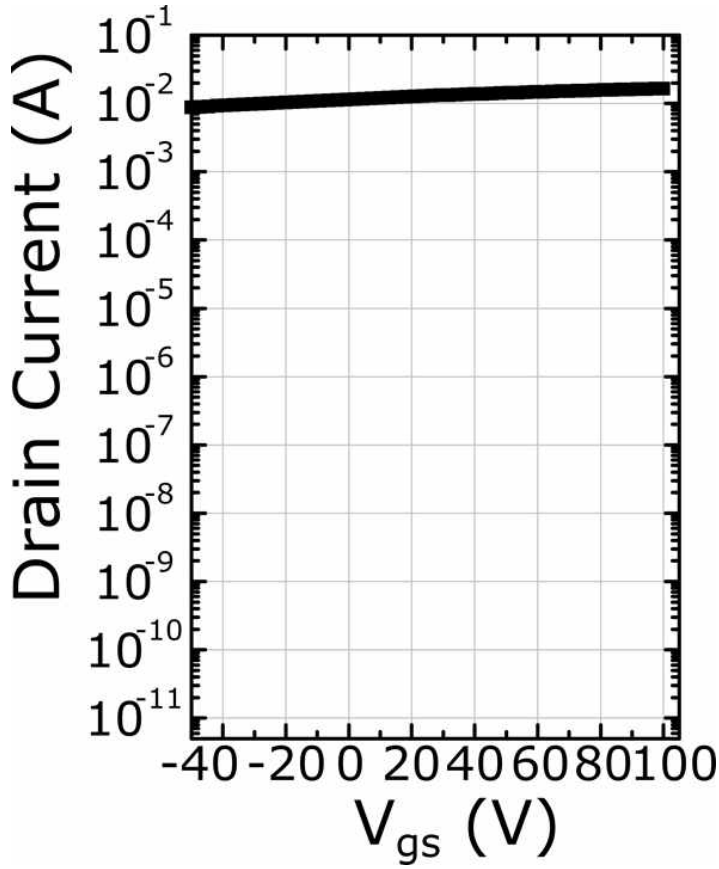

Figure 4.26 Electrical characteristics of SnO_x TFTs on SiO_2. The device is designed on 200 nm SiO_2 with 1000 μm channel width and 50 μm channel length.

	ZnO_x on 0% HCA	ZnO_x on 60% HCA
T_0(K)	609.75	585.57
N_t^{total}(cm^{-3})	$7.5*10^{19}$	$1.6*10^{19}$
a (cm^{-1})	-	-
σ_0 (S cm^{-1})	10.90	17.83
σ (S cm^{-1})	0.0045	0.0074
μ (cm^2 V^{-1} s^{-1})	0.0111	0.092

Table 4.5 The physical parameters of ZnO_x on HCA resulted from theoretical fitting based on MTR model.

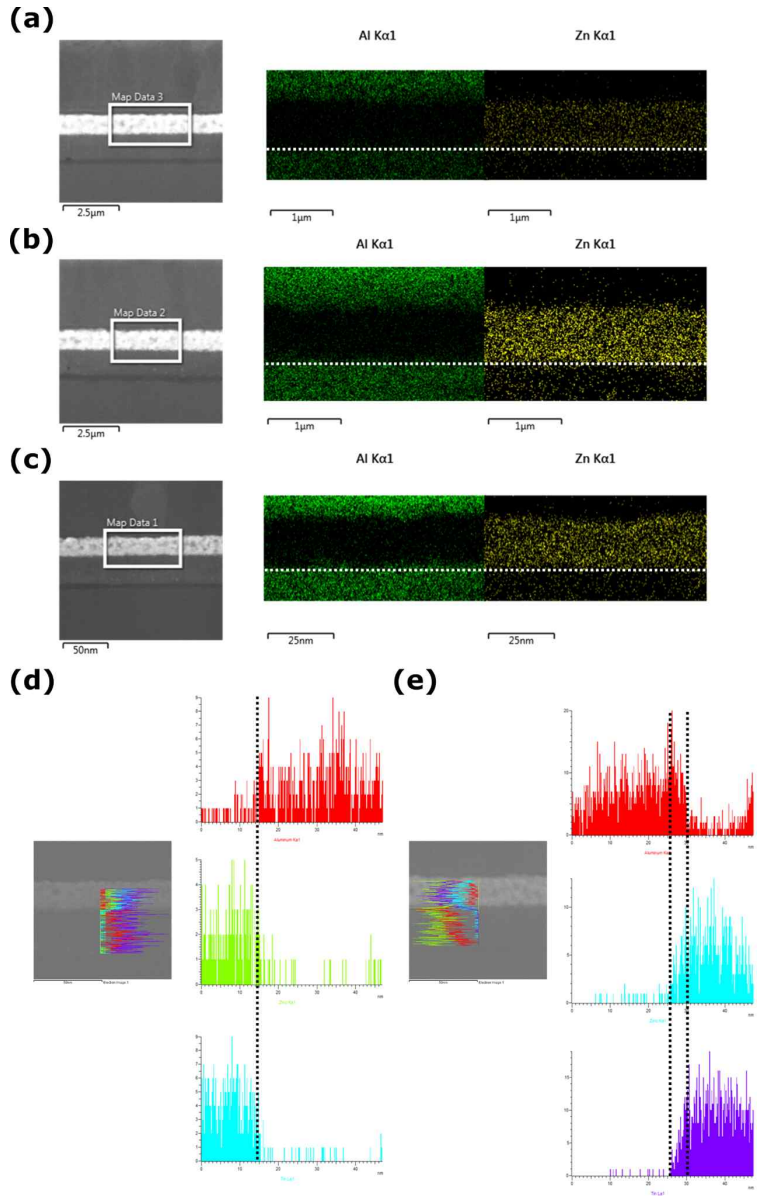

Figure 4.27 The EDX data for dispersion of Al atoms. Square analysis of (a) 0% HCA, (b) 10% HCA, and (c) 60% HCA. Line analysis of (d) 0% HCA and (e) 60% HCA.

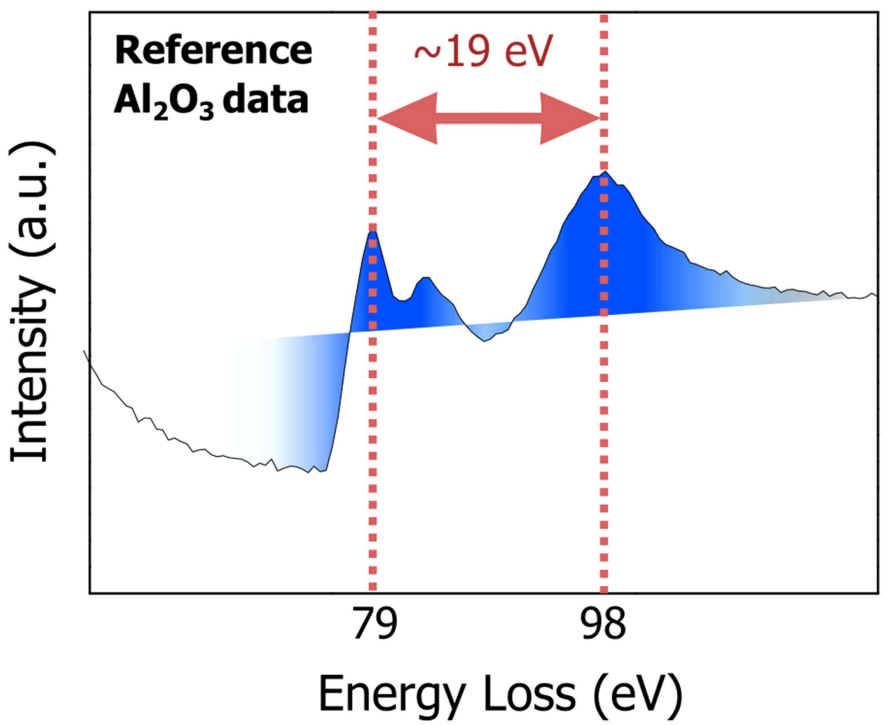

Figure 4.28 The EELS reference data of Al_2O_3. The EELS refrence data of Al_2O_3 show the peaks at about 79 and 98 eV.

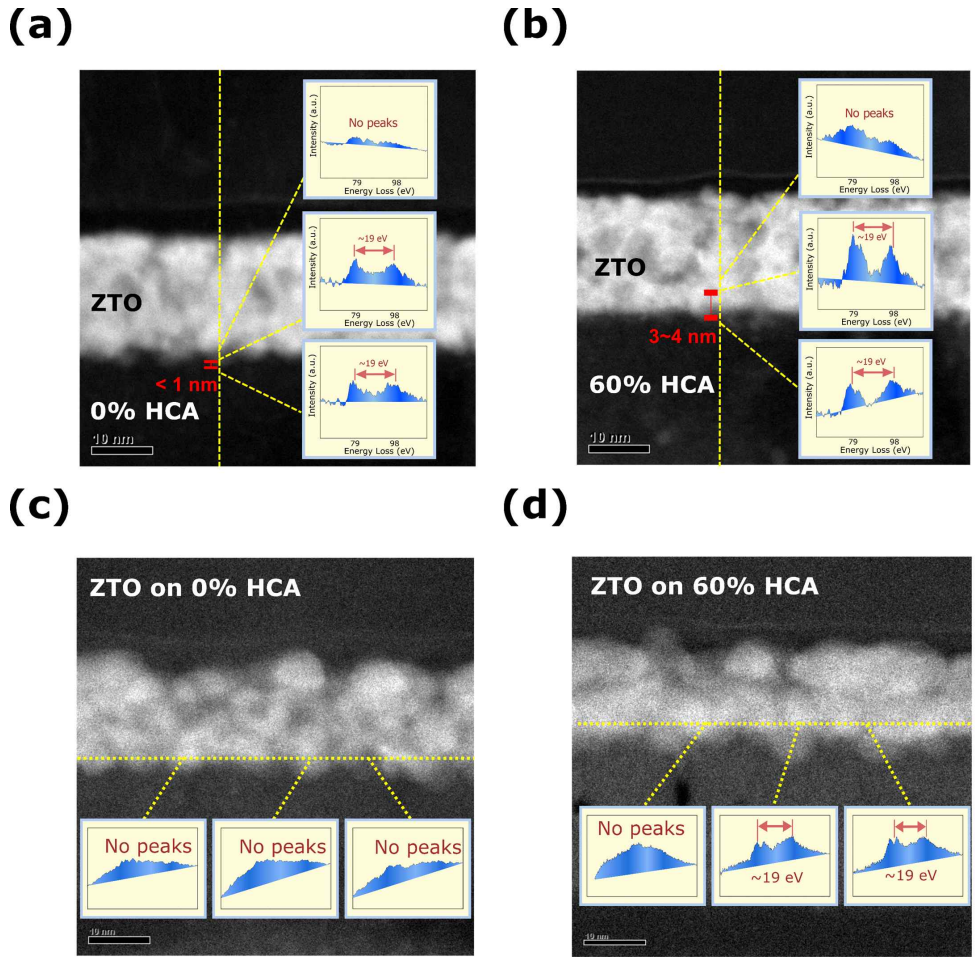

Figure 4.29 Interface and physical properties of ZTO/HCA films. The Al atoms existence of horizontal direction at the interface with ZTO films on (a) 0% HCA and (b) 60% HCA. The Al atoms existence of vertical direction at the interface with ZTO films on (c) 0% HCA and (d) 60% HCA. The insets in (a), (b), (c) and (d) confirm the existence of Al atoms at the interface through the EELS peaks comparing to the reference peak of AlO_x.

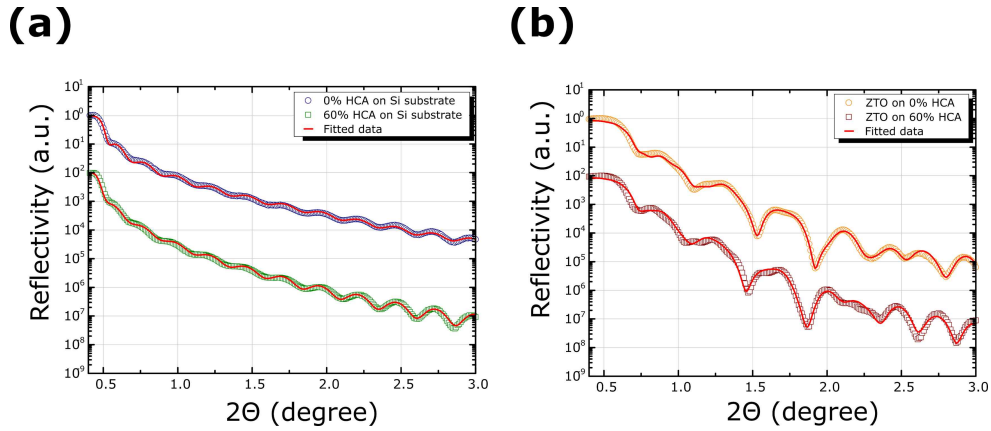

Figure 4.30 (a) and (b) XRR characterization of the HCA films and ZTO films on HCA. Red lines mean the theoretical fits.

	0% HCA	60% HCA
Thickness of surface layer	3.26 nm	1.60 nm
Density of surface layer	2.94 g cm^{-3}	0.53 g cm^{-3}
Thickness of HCA layer	31.30 nm	33.83 nm
Density of HCA layer	2.67 g cm^{-3}	2.59 g cm^{-3}
Thickness of native SiO_2	1.87 nm	1.61 nm
Density of native SiO_2	2.35 g cm^{-3}	2.60 g cm^{-3}

Table 4.6 XRR fitting of HCA films on Si substrate fabricated by one-run. The average thickness and density of the suface layer, HCA layer, and native oxide are obtained.

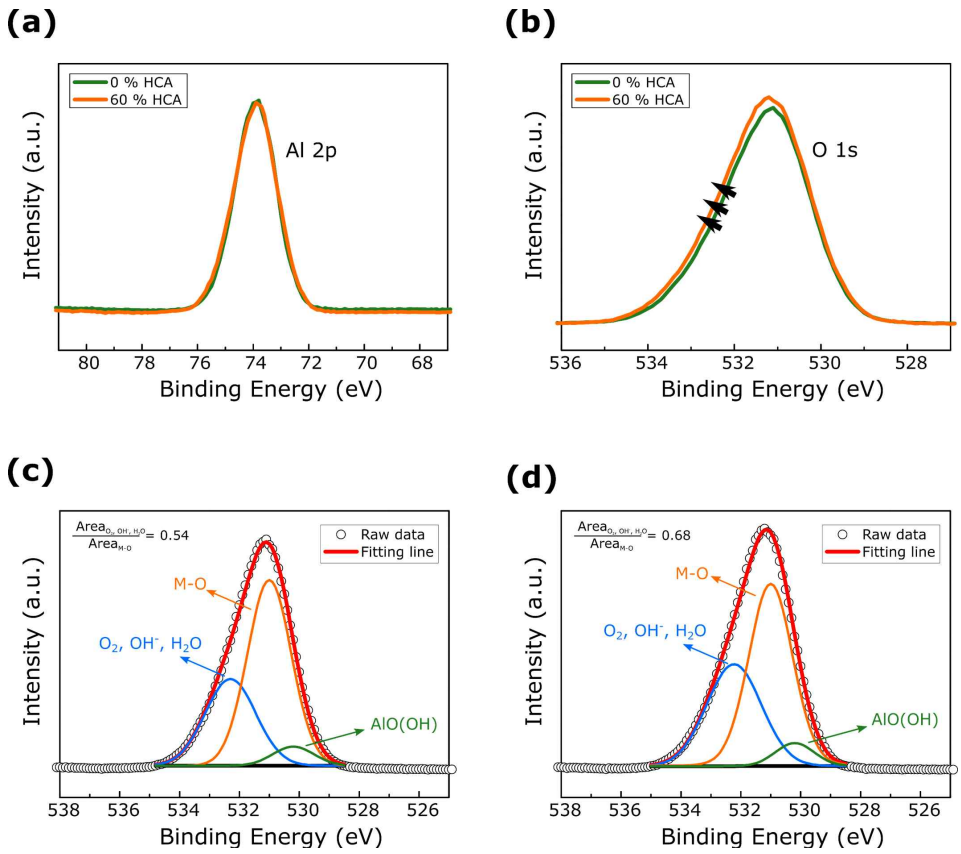

Figure 4.31 The XPS spectra of aluminum oxide dielectric. (a) Al 2p peaks of HCA films. (b) O 1s peak of HCA films. The fitted spectrums of O 1s peaks of (c) 0% HCA and (d) 60% HCA.

4.7 Role of Al atoms in interface between ZTO and HCA

Theoretically, Al atoms can induce the carrier density in oxide semiconductors by doping effects. [27, 28] However, in this case, the doping effects cannot be a main factor explaining the abnormal phenomenon, because the change of maximum effective field-effect mobility and physical parameters cannot be explained by doping mechanism. The most likely possibility is that Al atoms distribution in Zn-based region increases the physical density of Zn-based region near the interface, which reduces a density of localized state or increases orbital overlap related with characteristic temperature and α coefficient. Similarly, some studies have shown that the density of localized states in Zn-based semiconductor can be reduced by AlO_x dielectrics. [29, 30] If the trap density or the width of the localized state distribution are increased under unusual localized state, much more accumulations of electrons and higher activation energy are needed in order that electrons move the unusual localized state located in high energy. This approach is supported by the XRR analyses, subthreshold swing (S) value, and fitting results based on above TFT models. The XRR analyses show that physical density of interface region in ZTO film on 60% HCA (3.71 g cm^{-3}) is enhanced in comparison with that in ZTO film on 0% HCA (3.14 g cm^{-3}) by the dielectric engineering. (Figure 4.30(b) and Table 4.7) Also, the S value of ZTO TFT on 60% HCA is 0.31 V $decade^{-1}$, which is lower than that of ZTO TFT on 0% HCA, 0.72 V $decade^{-1}$. Trap densities

are obtained from the relation as follows [31]

$$S = \ln 10 \cdot \frac{k_B T}{q}\left[1 + \frac{q(D + tN_b)}{C_i}\right] \qquad (11)$$

,where k_B is the Boltzmann constant, T is the temperature of devices, q is the electron charge, t is the channel layer thickness, C_i is the gate-dielectric capacitance per area, D_{it} is the density per area of shallow traps at the interface and N_b is the density per volume of the shallow traps in the semiconductor bulk region. The total shallow trap density (D_{it}+tN_b) of ZTO TFTs on 60% HCA shows the $5.49 \cdot 10^{12}$ cm^{-2} eV^{-1}, which is lower than that of ZTO TFTs on 0% HCA, $1.16 \cdot 10^{13}$ cm^{-2} eV^{-1}. Similarly, in the fitting result through the VRH model, the ZTO films on 60% HCA show the lower T_0, N_t^{tot} and higher a values comparing with them of ZTO on 0% HCA. Furthermore, in MTR model, the physical parameters of ZnO_x films on HCA also show similar tendency.

In the (metal-insulator-semiconductor-metal) MISM structure, the capacitance shows similar range compared with the capacitance in MIM structure. (because the ion effect is not induced by deposition of semiconductor region.) The slope of capacitance depending on voltage in MISM device with 60% HCA is higher compared with that in MISM device. In conventional semiconductor theory, the slope of capacitance in MISM device is related with the trap density of semiconductor region. In typical, when the slope is higher, the amount of traps is lower. Accordingly, the tendency of capacitance slope in MISM device with HCA corresponds to results in SS values.

ZTO/HCA/Si	0% HCA	60% HCA	ZTO/SiO_2/Si	60% HCA
Thickness of ZTO surface layer	2.74 nm	2.73 nm	Thickness of ZTO surface layer	3.10 nm
Density of ZTO surface layer	8.15 g cm^{-3}	8.01 g cm^{-3}	Density of ZTO surface layer	7.91 g cm^{-3}
Thickness of ZTO bulk layer	16.47 nm	17.06 nm	Thickness of ZTO bulk layer	19.53 nm
Density of ZTO bulk layer	5.12 g cm^{-3}	5.10 g cm^{-3}	Density of ZTO bulk layer	5.72 g cm^{-3}
Thickness of ZTO near the interface	2.71 nm	1.26 nm	Thickness of ZTO near the interface	1.93 nm
Density of ZTO near the interface	3.14 g cm^{-3}	3.71 g cm^{-3}	Density of ZTO near the interface	2.90 g cm^{-3}
Thickness of HCA near the interface	2.14 nm	1.23 nm	Thickness of SiO_2 layer	205.80 nm
Density of HCA near the interface	3.47 g cm^{-3}	2.76 g cm^{-3}	Density of SiO_2 layer	2.40 g cm^{-3}
Thickness of HCA bulk layer	30.32 nm	30.46 nm		
Density of HCA bulk layer	2.87 g cm^{-3}	2.81 g cm^{-3}		
Thickness of native SiO_2	2.78 nm	3.23 nm		
Density of native SiO_2	2.50 g cm^{-3}	2.50 g cm^{-3}		

Table 4.7 XRR fitting of ZTO films on HCA films or SiO_2 film fabricated by one-run.

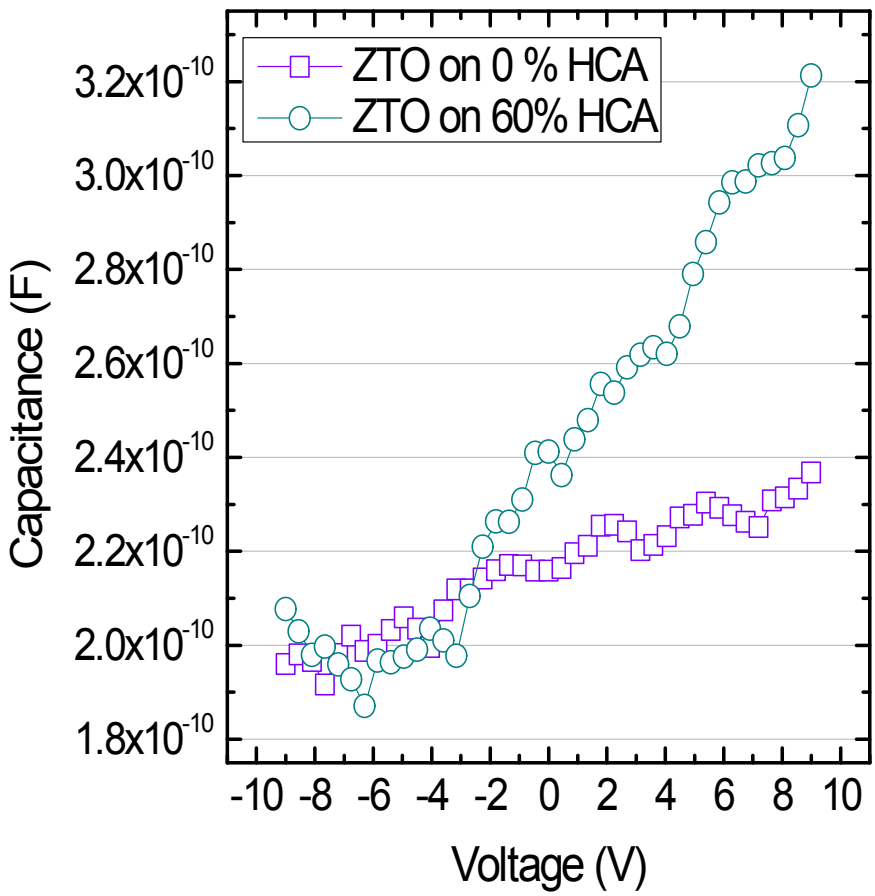

Figure 4.32 The capacitance of MISM (metal - Insulator - semiconductor - metal) structure. (The semiconductor and top metal region were patterned in circle shape, R = 250 μm, 20 Hz frequency condition)

4.8 Electrical transport model for ZTO TFTs on HCA

In these respects, it is deduced the effective field-effect mobility of ZTO TFTs on 60% HCA is abnormally enhanced by two main concepts: The first is that the phase separation in ZTO film on HCA occurs, resulting in two different localized states for the transport of electrons: the general localized state at low energy level in Zn-based region and the unusual localized state located in high energy level in SnO_x nano-composites. The second is that the part of Zn-based oxide semiconductor is reacted Al atoms, which increases the density of Zn-based region near the interface, resulting in the decrease of the trap density or the increase of orbital overlap of Zn-based oxide semiconductor. Based on these concepts, I propose a mechanism for electron transport in ZTO TFTs on 60% HCA. (Figure 4.32) In case of ZTO TFT on 0% HCA, no matter how V_{gs} is increased until electrical breakdown voltage, the electrons in the Zn-based region hardly move the unusual localized state of crystalline SnO_x nano-composites located in high energy level due to many traps or large wide width of the localized state distribution. (Figure 4.32 (a)) On the contrary, in case of ZTO TFT on 60% HCA, Zn-based region has smaller traps or narrowing the width of localized state distribution by the Al diffusion. Accordingly, when the gate-source voltage is lower than the specific gate-source voltage, the Fermi level lies at lower energy level, and the movement of electrons follows the electron transport mechanism of Zn-based oxide semiconductor region.

(Figure 4.32 (b)) However, over the specific gate-source voltage higher, as the Fermi level can lie at a high energy level, electron can move the unusual localized state in SnO_x nano-composites, and move faster, resulting in the dramatic improvement of field-effect mobility. (Figure 4.32 (c)) In this region, although the electron path is composed of highly conductive SnO_x nano-composites and the improved Zn-based oxide semiconductors (about 50 cm^2 V^{-1} s^{-1}), it shows homogeneous-like electrical properties in the micro-scale. For the reason, the concept 'effective field-effect mobility' is used instead of 'field-effect mobility' to avoid confusion related to theoretical intrinsic mobility.

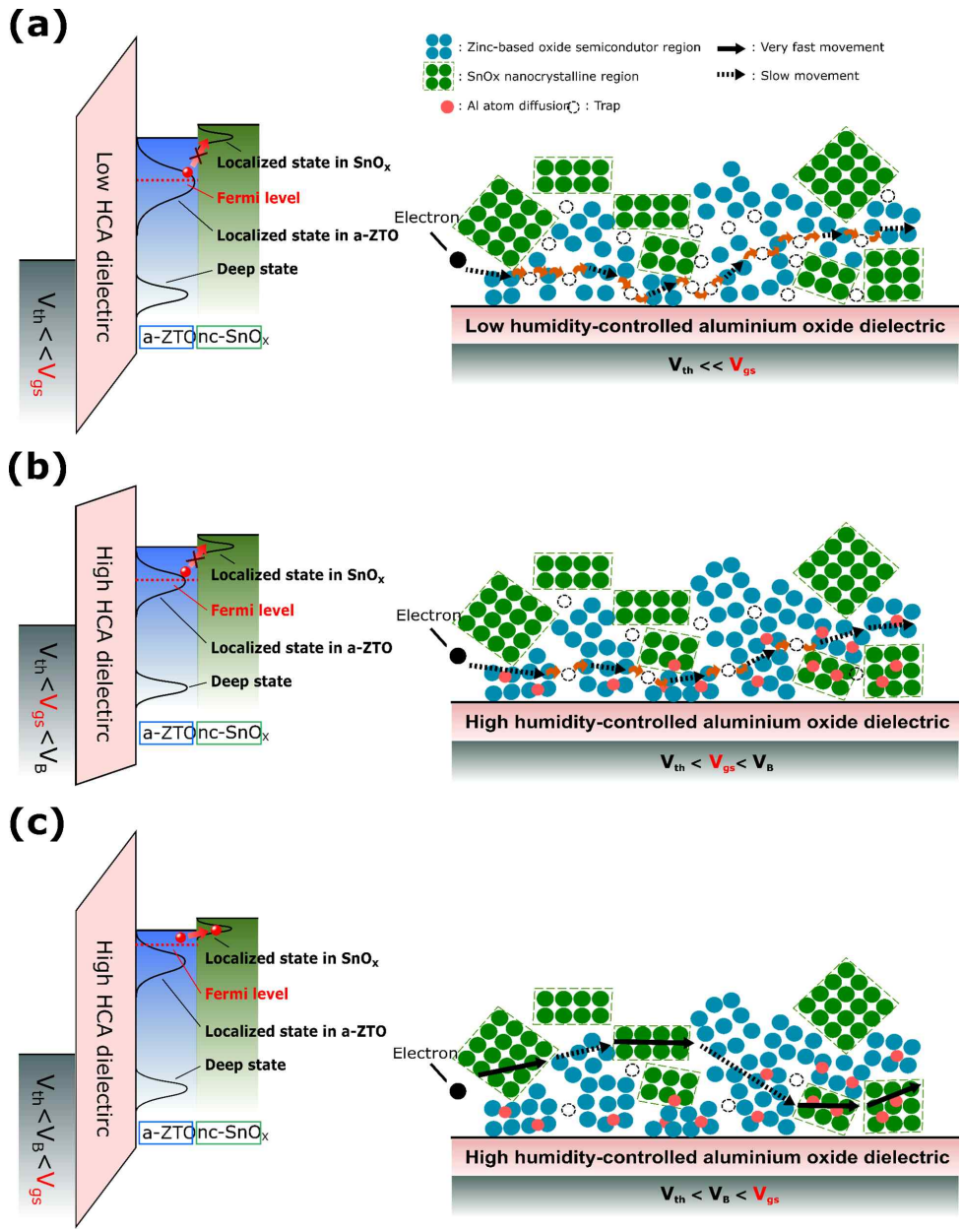

Figure 4.33 The electron transport mechanism at ZTO TFTs on HCA. (a) The band diagram and electron transport mechanism of ZTO TFT on 0% HCA at high V_{gs} (ZTO TFTs on 0% HCA at V_{gs}

= 10 V). The band diagram and electron transport mechanism of ZTO TFT on 60% HCA when (b) V_{gs} is lower than specific voltage (ZTO TFTs on 0% HCA at V_{gs} < 6 V, gradual enhancement region) or (c) V_{gs} is higher than specific voltage (ZTO TFTs on 0% HCA at V_{gs} > 6 V, dramatic enhancement region).

4.9 Experimental details

Solution synthesis for oxide thin-films in TFT

A $Zn_xSn_yO_z$ (ZTO) solution was prepared using the method described in ref. [7]. 0.3 M zinc acetate ($Zn(CH_3COO)_2$) and 0.3 M ethanolamine were dissolved in 10 mL of 2-methoxyethanol and then, the 0.45 M tin chloride ($SnCl_2$) in 10 mL of 2-methoxyethanol were added to the above solution. To make stable solution, before combining the two solution, each solution was stirred at 1000 rpm for 6 hours. In addition, The zinc oxide (ZnO_x) solution and the tin oxide (SnO_x) solution were prepared by 0.375 M zinc acetate ($Zn(CH_3COO)_2$) with 0.3 M ethanolamine and 0.375 M tin chloride ($SnCl_2$) in 10 mL of 2-methoxyethanol, respectively. For fabricating the HCA film, 0.3 M aluminium nitrate nonahydrate ($Al(NO_3)_39H_2O$) was dissolved in 10 mL of 2-methoxyethanol. Additionally, this Al_2O_3 solution was stirred on 120°C for 1 hour.

Dielectric-engineered ZTO/HCA film fabrication

All ZTO TFTs were prepared on highly boron-doped Si substrates which were washed using the detergent, acetone and isopropyl alcohol. Al_2O_3 solution was spin-coated onto Si substrate or SiN_x layer at 2000 rpm for 30 seconds and soft-baked at 200°C for 30 minutes in nitrogen glove box. And then, the film kept at 500°C for 30 minutes in humidity-controlled atmosphere condition. The heating rate of tube furnace is controlled to 16.6°C/minutes. Humidity condition is controlled by clean dry air and humidifier in tube furnace.

0% humidity condition means the clean dry air environment within 3% humidity and then, 10%, 20%, 40%, 60% relative humidity condition at about 25°C has margin of error of plus or minus 3% (e.g., 10% humidity means the humidity between 7%-13%). The ZTO solution was spin-coated on fabricated humidity-controlled Al_2O_3 film at 5000 rpm for 30 seconds in nitrogen glove box. Finally, the ZTO film spin-coated on Al_2O_3 film was directly baked at raised 500°C for 30 minutes in 60% humidity condition atmosphere. The ZnO_x and SnO_x TFTs are fabricated by same method which is above mentioned.

Dielectric-engineered ZTO/HCA/SiN_x film fabrication.

100 nm and 200 nm SiN_x layers of all ZTO/Al_2O_3/SiN_x TFTs were fabricated by PECVD process in about 300°C. And the, HCA layer and ZTO films are fabricated in same method which is above mentioned.

Thin-film transistor fabrication and patterning process

For TFT fabrication, Al electrodes were thermally evaporated onto fabricated ZTO layer up to 100 nm thickness with 1000 μm width and 15~50 μm length through the shadow masks. For the precise pattern, the shadow masks having magnetic property are used. The evaporation speed is about 0.1 nm/s up to 10 nm and 0.4 nm/s from 10 nm to 100 nm.

For patterning process of ZTO/HCA and ZTO/HCA/SiN_x TFTs, the

photolithography process is accomplished to obtain the patterned devices, with AZ GXR-601 photoresist and AZ 300 MIF developer, dilute HF etchant. In this process, controlling the etching time is important to prevent the AlO_x region and electrical degradation of ZTO film.

Characterization and measurements

The transfer and output characteristics were measured by semiconductor parameter analyzer (Agilent 4155B) under dark and ambient condition (25°C, about 40% humidity condition). Only, the electrical behavior of oxide semiconductor TFT according to various temperatures is measured at vacuum condition. The capacitance was analyzed by precision LCR meter (Agilent 4284A) under ambient and vacuum condition. Also, the capacitance in low frequency (< 20 Hz) is obtained by Bio-Logic SP-150. The effective field-effect mobility of oxide semiconductor TFTs in both saturation and linear regime is evaluated by general MOSFET model as Equation (3) and (4). Only, the field-effect mobility of reference ZTO TFT on SiO_2 is calculated in saturation regime. Remaining oxide semiconductor TFTs such as ZTO TFTs on HCA, and ZTO TFTs on a bilayer dielectric composed of HCA and SiN_x are evaluated in linear regime to avoid the current compliance problem in I-V measurement. Cross-sectional images, EDX and EELS data were prepared and obtained using a focused ion beam instrument and Analytic TEM (JEM-2100F, JEOL, NOVA 600 NanoLab, FEI Co.). XRR (SmartLab, Rigaku Co.) was used to obtain

the density and thickness of the HCA films with Cu-Kα radiation (λ = 1.54 Å) at 45 kV and 200 mA. XRR fitting is accomplished by GlobalFit program. XRD (D8 Advance, Bruker Co.) was used with in-plane mode and 6 kW to define the crystal structure. XPS (theta probe base system, Thermo Fishier Scientific Co.) was used to characterize the electronic state of the Al_2O_3 films. It was calibrated by the carbon 1s peak (284.6 eV) in consideration of Al 2P peak (74.3 eV). In addition, the morphology of the films were characterized by AFM (XE100, PSIA Co.).

4.10 References

[1] K. Nomura, H. Ohta, K. Ueda, T. Kamiya, M. Hirano, H. Hosono, Science, 2003, 300, 1269.

[2] Y.-H. Kim, J.-S. Heo, T.-H. Kim, S. Park, M.-H. Yoon, J. Kim, M. S. Oh, G.-R. Yi, Y.-Y. Noh, S. K. Park, Nature, 2012, 489, 128.

[3] M.-G. Kim, M. G. Kanatzidis, A. Facchetti, T. J. Marks , Nat. Mater. 2011, 10, 382.

[4] E. Fortunato, P. Barquinha, R. Martins, Adv. Mater. 2012, 24, 2945.

[5] J. Jang, R. Kitsomboonloha, S. L. Swisher, E. S. Park, H. Kang, V. Subramanian, Adv. Mater. 2013, 25, 1042.

[6] S. Y. Park, B. J. Kim, K. Kim, M. S. Kang, K.-H. Lim, T. I. Lee, J. M. Myong, H. K. Baik, J. H. Cho, Y. S. Kim, Adv. Mater. 2012, 24, 834.

[7] K.-H. Lim, K. Kim, S. Kim, S. Y. Park, H. Kim, Y. S. Kim, Adv. Mater. 2013, 25, 2994.

[8] Y. S. Rim, H. Chen, X. Kou, H.-S Duan, H. Zhou, M. Cai, H. J. Kim, Y. Yang, Adv. Mater. 2014, 26, 4273.

[9] T. Kamiya, K. Nomura, H. Hosono. Sci. Technol. Adv. Mater. 2010, 11, 044305.

[10] H.-W. Zan, W.-T. Chen, C.-C. Yeh, H.-W. Hsueh, C.-C. Tsai, H.-F. Meng, Appl. Phys. Lett. 2011, 98, 153506.

[11] S. T. Meyers, J. T. Anderson, C. M. Hung, J. Thompson, J. F. Wager, D. A. Keszler, J. Am. Chem. Soc. 2008, 130, 17603.

[12] S. Y. Han, G. S. Herman, C. H. Chang, J. Am. Chem. Soc. 2011,

133, 5166.

[13] K. K. Banger, Y. Yamashita, K. Mori , R. L. Peterson, T. Leedham, J. Rickard, H. Sirringhaus, Nat. Mater. 2011, 10, 45.

[14] G. Adamopoulos, S. Thomas, P. H. Wobkenberg, D. D. C. Bradley, M. A. McLachlan, T. D. Anthopoulos. Adv. Mater. 2011, 23, 1042.

[15] C. Avis, H. R. Hwang, J. Jang, Appl. Mat. Interfaces. 2014, 6, 10941.

[16] G. Huang, L. Duan, G. Dong, D. Zhang, Y. Qiu, Appl. Mat. Interfaces. 2014, 6, 20786.

[17] X. Yu, J. Smith, N. Zhou, L. Zeng, P. Guo, Y. Xia, A. Alvarez, S. Aghion, H. Lin, J. Yu, R. P. H. Chang, M. J. Bedzyk, R. Ferragut, T. J. Marks, A. Facchetti, PNAS, 2015, 112, 3217.

[18] X. Yu, T. J. Marks, A. Facchetti, Nat. Mater. 2016, 15, 383.

[19] B. N. Pal, B. M. Dhar, K. C. See, H. E. Katz, Nature Mater. 2009, 8, 898.

[20] J. B. Kim, F.-H. C., K. B. Appl. Phys. Lett. 2008, 93, 242111.

[21] E. Lee, J. Ko, K.-H. Lim, K. Kim, S. Y. Park, J. M. Myoung, Y. S. Kim, Adv. Func. Mater. 2014, 24, 4689.

[22] A. Zeumault, V. Subramanian, Adv. Func. Mater. 2016, 26, 955.

[23] R. Branquinho, D. Salgueiro, L. Santos, P. Barquinha, L. Pereira, R. Martins, E. Fortunato, Appl. Mat. Interfaces. 2014, 6, 19592.

[24] H. Xu, D. Luo, M. Li, M. Xu, J. Zou, H. Tao, L. Lan, L. Wang, J. Peng, Y. Cao, J. Mater. Chem. 2014, 2, 1255.

[25] G. Lefe'vre, M. Duc, P. Lepeut, R. Caplain, M. Fe´doroff,

Langmuir, 2002, 18, 7530.

[26] F. Torricelli, J. R. Meijboom, E. Smits, A. K. Tripathi, M. Ferroni, S. Federici, G. H. Gelinck, L. Colalongo, Z. M. Kovacs-Vajna, D. de Leeuw, E. Cantatore, IEEE Trans. Electron Devices. 2011, 58, 2610.

[27] Z. B. Ayadi, L. E. Mir, Nanotechnology. 2007, 18, 445702.

[28] Y.-G. Lee, W.-S. Choi, Electron. Mater. Lett. 2013, 9, 719.

[29] L. Lan, J. Peng, IEEE Trans. Electron Devices. 2011, 58, 1452.

[30] W. Xu, H. Wang, L. Ye, J. Xu, J. Mater. Chem. 2014, 2, 5389.

[31] L. Shao, K. Nomura, T. Kamiya, H. Hosono, Electrochem. Solid-State Lett. 2011, 14, H197.

Chapter 5. Conclusions

In summary, this dissertation proposes alkali metal doping and dielectric engineering for enhancement of field-effect mobility in solution-processed oxide semiconductor TFTs. Also, through the various analyses, the mechanism regarding the enhancement of field-effect mobility was investigated by various analyses.

First, alkali metals as a dopant enhanced the field-effect mobility by 2 to 3 times in solution-processed amorphous ZTO semiconductor TFTs. Furthermore, a new monitoring technique on the electrical performance was proposed, such as field effect mobility in ZTO TFTs, in terms of the variation of optical bandgap of ZTO semiconductor films using spectroscopic UV-visible ray analysis. Although the fluctuation of oxygen vacancy content in the XPS analysis and carrier concentration in the Hall measurement correlated with the enhanced field-effect mobility in ZTO TFTs, there were cumbersome and destructive methods for on-spot monitoring the performance of ZTO TFTs. Otherwise, the change in the optical bandgap observed by spectroscopic UV-visible ray analysis successfully represented the change of field effect mobility in ZTO TFTs, as related to the doping concentration of alkali metals. This result shows good potential as a new technique for monitoring the electrical performance of oxide semiconductor TFTs as fast and non-destructive analysis.

Second, dielectric engineering for solution-processed oxide semiconductor TFTs with ultrahigh effective field-effect mobility was

introduced. Through the dielectric engineering, I successfully demonstrated ZTO TFTs with ultrahigh effective field-effect mobility over 400 cm^2 V^{-1} s^{-1} with a 10^6 on/off current ratio. In addition, through introducing the dielectric engineering to ZTO TFTs with conventional dielectric layer (a low capacitance SiNx), the unique effects of the dielectric engineering was successfully investigated. Through the TFT models and various analyses, I found out that the abnormal enhancement of effective field-effect mobility is originated from two phenomena; the phase separation of ZTO on HCA layer, and the change of trap density and orbital overlap in Zn-based oxide semiconductor region by the Al diffusion. Based on these observations, I proposed a novel electron transport mechanism for abnormal enhancement of the effective field-effect mobility of ZTO TFTs. These findings demonstrate that the physical properties of oxide semiconductor are strongly related to properties of solution-processed dielectric. The dielectric engineering in this study shows good potential as a breakthrough for fabricating oxide semiconductor TFTs with high effective field-effect mobility beyond the conventional oxide semiconductor TFT.

In these respects, I believe that the alkali metal doping and dielectric engineering can yield the important clues for the application of the oxide semiconductor TFTs in advanced display industry.

요 약 (국문초록)

알칼리 금속 도핑과 절연체 엔지니어링을 통한 고성능 용액 공정 산화물 반도체 박막 트랜지스터 개발에 관한 연구

최근에, 정보화 시대의 도래에 따라, 시각적인 정보를 더 사실적이고 정확하게 전달하기 위하여, 더 크고 고해상도를 가진 고성능 디스플레이가 개발되고 되어왔다. 미래에는 더 효율적이고 인체 친화적으로 정보를 전달하기 위하여 더 높은 성능 뿐 만 아니라, 투명하고 유연한 특성을 가진 디스플레이가 요구 되고 있다. 이러한 미래의 디스플레이를 개발하기 위해서는, 디스플레이에서 스위칭 소자로서 핵심 역할을 하는 박막 트랜지스터가 고성능의 특성과 함께 투명하고 유연한 성질을 가져야 한다.

실리콘 기반의 박막 트랜지스터는 기존의 LCD (Liquid Display) 및 OLED (Organic Light Emitting Display) 디스플레이에 주로 사용되어 왔다. 실리콘 기반의 박막 트랜지스터의 일종인 LTPS (Low Temperature Poly Silicon) 박막 트랜지스터는 100 cm^2 V^{-1} s^{-1} 이상의 고이동도 특성을 가진다. 그러나 생산 시설 비용이 높고, 대면적 공정이 취약하다는 단점이 있다. 게다가, 불투명하고 유연하지 못한 특성의 한계점을 가지고 있다. 산화물 박막 트랜지스터는 투명하고 유연한 특성을 가지고 있기 때문에, 미래의 디스플레이용 박막 트랜지스터로 많은 연구가 되어왔다. 특히, 용액 공정을 통한 산화물 반도체 박막 트랜지스터는 적은 비용, 대면적 생산 및 연속 공정으로 제조가 가능하게 하므로 많은 관심을 받아왔다. 따라서, 고성능의 용액 공정 산화물 반도체를 개발하기

위하여 다양한 방법들이 제시되어 왔다. 그러나, 아직까지 낮은 이동도의 성능 특성을 가지기 때문에 실제적인 적용에 큰 문제점이 되고 있다.

본 연구에서는 고이동도 특성의 고성능을 가진 용액 공정 산화물 반도체 박막 트랜지스터 개발을 위하여 알칼리 메탈 도핑과 절연체 엔지니어링 방법을 제안하였다. 용액 공정 $ZnSn_xO_y$ (ZTO) 반도체에 알칼리 금속을 도핑하는 과정을 통하여, 이동도를 올리는 방법을 제시하였다. 알칼리 금속이 도핑 된 ZTO 박막 트랜지스터는 같은 조건에서 약 2~3배의 높아진 이동도 특성을 보여주었다. 한편, 절연체 엔지니어링을 하기 위해, 용액 공정으로 제조되는 Al_2O_3 절연체의 공정 조건을 조절 하였다. 절연체 엔지니어링이 된 용액 공정 절연체를 용액 공정 ZTO TFT에 적용하여, 매우 높은 이동도 특성을 갖는 ZTO TFT를 구현해내었다. 이러한 방법들에 의한 이동도 증가 현상을 규명하기 위하여, X-ray diffraction (XRD), high-resolution transmission electron microscopy (HRTEM), atomic force microscopy (AFM), photoemission spectroscopy (XPS) 뿐만 아니라 TFT 모델링 등의 분석 기술들이 응용 되었다. 이러한 분석을 토대로, 이동도 증가 현상을 설명할 수 있는 메커니즘이 규명되었다.

결론으로, 본 연구에서는 알칼리 메탈 도핑과 절연체 엔지니어링을 사용하여 고이동도 특성을 갖는 고성능 용액 공정 산화물 반도체 박막 트랜지스터를 개발하였다. 또한, 체계적인 분석을 통하여 이동도의 증가 현상의 메커니즘을 규명하였다. 이러한 접근은 고성능 박막 트랜지스터가 필요한 미래의 디스플레이 기술에 높은 잠재성이 있을 것으로 예상된다.

주요어 : 산화물 반도체, 용액 공정, 고이동도, 박막 트랜지스터, 알칼리 금속 도핑, 절연체 엔지니어링

학 번 : 2011-22761